

Brandenburgische Technische Universität Cottbus - Senftenberg

Fakultät Maschinenbau, Elektro- und Energiesysteme

Lehrstuhl Thermodynamik und Thermische Verfahrenstechnik

Prof. Dr.-Ing. Fabian Mauß



Brandenburgische
Technische Universität
Cottbus - Senftenberg

Kinetic mechanism of surrogates for biodiesel

Von der Fakultät für Maschinenbau, Elektro- und Energiesysteme
der Brandenburgischen Technischen Universität Cottbus–Senftenberg
zur Erlangung des akademischen Grades eines Doktors der
Ingenieurwissenschaften

genehmigte Dissertation

Vorgelegt von
M. Sc
Xiaoxiao Wang

geboren am 29.11.1985 in Zhejiang, China

Vorsitzender: Prof. Dr.-Ing. habil. Sabine Weiß

Gutachter: Prof. Fabian Mauß

Gutachter: PD Dr. Thomas Zeuch

Tag der mündlichen Prüfung: 11.12.2017

Abstract

In recent years, biodiesel is an alternative fuel to petroleum diesel that is renewable and creates less harmful emissions than conventional diesel. Biodiesel blends – usually B20 or below, have been the most commonly used biodiesel blends. In current study, the kinetic mechanism of *n*-decane/ α -methyl-naphthalene (AMN)/methyl-decanoate (MD) blend is developed and validated as the surrogate for biodiesel/diesel blends.

The IDEA reference fuel (70% *n*-decane/30% AMN by liquid volume) was formulated in the past as a two-component diesel surrogate fuel. A comprehensive and compact oxidation model for the IDEA reference fuel is developed. One important fuel-fuel interaction pathway via reaction pathway of $A_2CH_2 + HO_2$ is observed and detailed discussed. The IDEA blends are validated by comprehensive target experiments for *n*-decane, AMN, and the AMN/*n*-decane blends. Ignition delay times, flame speeds, and species composition in jet stirred reactor and counter flow flames are successfully simulated for a broad range of temperatures (500-2000 K) and pressures (1-50 bar). The simulations of the IDEA blend with current model show acceptable agreement when compared with different experiments of ignition delay times for diesel fuels as well as flame speed experiments.

With a chain of ten carbon atoms and a methyl-ester group attached, MD is considered as a one-component surrogate fuel for biodiesel. A comprehensive and compact kinetic model for MD is developed. The mechanism is critically tested by comparison of model predictions with experimental data over a wide temperature (500 to 1500 K) and pressure (1 to 20 bar) range and for different fuel/oxidizer ratios. The good maintenance of chemical information during the reduction has been confirmed by simulation results, as well as the sensitivity and flow analyses performed using the detailed and the skeletal model. The MD model is compared with available experimental ignition delay times of biodiesel fuels. The good agreement between the simulations and the experiments proves that this model is a reliable kinetic model for simulations, either used by itself or in combination with IDEA blend.

To improve the mechanism analysis, this thesis introduces a new three-stage reactive flow analysis. The final skeletal *n*-decane/AMN/MD blend with skeletal base mechanism includes 295 species and 3500 reactions by using the CGR approach. Based on the above validations and comparisons, current blend is considered as one surrogate for biodiesel/diesel blends that is suitable for improving kinetic understanding and for application in engine simulations.

Contents

Abstract	I
Contents	II
1 Introduction	1
1.1 Background.....	1
1.2 Biofuels overview.....	2
1.3 Objectives	2
1.4 Thesis organization.....	3
2 Theoretical fundamentals	4
2.1 Chemical kinetics	4
2.1.1 Rate law	4
2.1.2 Rate coefficient	6
2.2 Reaction mechanism.....	8
2.2.1 Elementary reaction.....	8
2.2.2 Chain reaction	8
2.3 Mechanism analysis.....	10
2.3.1 Sensitivity analysis	10
2.3.2 Reaction flow analysis	12
2.4 Physical modeling	12
2.5 Reactor modeling.....	12
2.5.1 Shock tube	12
2.5.2 Jet stirred reactor	16
2.5.3 Laminar, one-dimensional, premixed flame	17
2.5.4 Free propagating flame.....	19
3 Fundamentals of kinetic mechanisms	22
3.1 Base mechanism	22
3.2 Extension strategy	24
3.3 Thermodynamic and transport properties.....	25
3.4 Chemistry-guided reduction (CGR)	26
4 Kinetic mechanism for the blends of AMN/<i>n</i>-decane	28
4.1 Mechanism development for <i>n</i> -decane.....	28
4.2 Mechanism development for AMN.....	33
4.3 Compilation of AMN/ <i>n</i> -decane	37

4.4	Fuel-fuel interaction	39
4.4.1	Blends of AMN and <i>n</i> -decane	41
4.4.2	Influence of pathway for $A_2CH_2 + HO_2$	44
4.5	Mechanism validations for pure <i>n</i> -decane and pure AMN	47
4.5.1	Ignition delay times	47
4.5.2	Laminar flame speeds.....	51
4.5.3	Jet stirred reactor	52
4.5.4	Premixed flame speciation	55
4.6	Mechanism validations for IDEA fuel blends	56
4.6.1	Ignition delay times	56
4.6.2	Jet stirred reactor	57
4.7	Surrogate fuel for diesel	58
4.7.1	Ignition delay times	59
4.7.2	Laminar flame speeds.....	62
5	Kinetic mechanism of MD	65
5.1	Mechanism development for MD.....	65
5.1.1	Detailed mechanism	66
5.1.2	Chemistry-guided reduction (CGR).....	71
5.2	Mechanism validations for MD	77
5.2.1	Ignition delay times	77
5.2.2	Laminar flame speeds.....	83
5.2.3	Jet stirred reactor	84
5.2.4	Diffusion flame speciation	87
5.2.5	Base mechanism	89
5.2.6	Three-stage flow analysis.....	90
5.3	Surrogate component for biodiesel.....	94
6	Conclusions.....	100
6.1	Conclusions	100
6.2	Suggestions for future research	102
	Bibliography	103
	Nomenclature.....	115
	Acknowledge.....	117

1 Introduction

1.1 Background

Commercial diesel is a complex blend of several hundreds of individual species. For detailed engine simulations, a proper diesel surrogate fuel is of importance. In the past, a surrogate fuel consisting of 70% *n*-decane/30% α -methyl-naphthalene (AMN) (by liquid volume) was formulated as part of the Intergrated Development on Engine Action (IDEA) program [1]. This IDEA reference fuel has the following properties: a normal density of 798 kg/m³ at 20 °C, a cetane number of 55, and a hydrogen-to-carbon ratio of 1.7, similar to those of European diesel fuel [2, 3].

In recent years, biofuels (such as biodiesels and alcohols) have gained much more attention as potential alternatives to fossil fuels due to their good exhaust quality, sustainability, and biodegradability [4]. In Germany, a duty of up to 7% of biodiesel to conventional diesel has been added according to the fuel standard EN 590 conventional diesel since 2009 [5]. Biodiesel blends – usually B5 or B20 – are available at an increasing number of service stations in all states [5]. Biodiesel blends of 20% (B20) and below can be used without any modification in diesel engines [6]. B20 is the most commonly used biodiesel blend in the United States because it provides a good balance between material compatibility, cold weather operability, performance, emission benefits, and costs [7]. Biodiesel can also be used in its pure form (B100), but may require certain engine modifications to avoid maintenance and performance problems [7].

Many studies have investigated the manufacturing process, performance, emission, and effects of biofuel blends with conventional fuels. The fundamental combustion properties and chemical kinetics of biofuels, especially the biodiesel blends are of importance but are still at an early stage. Therefore, the motivation of this thesis is to develop the kinetic mechanism of surrogates for biodiesel/diesel blends. The kinetic mechanism of *n*-decane/AMN blend as a surrogate model for conventional diesel fuels and the kinetic mechanism of methyl-decanoate (MD) as one-component surrogate model for biodiesels are respectively developed. Finally, the *n*-decane/AMN/MD blend can be applied as the surrogate model for biodiesel/diesel blends.

1.2 Biofuels overview

Biofuels are defined as liquid or gaseous fuels for the transport sector that are predominantly produced from biomass [8]. Biodiesel is one of the major biofuel products produced via a biochemical conversion process. The composition of biodiesel is typically a combination of long chain fatty acid methyl-esters derived from vegetable oils or animal fats through the transesterification process shown in Figure 1.1 [9]. The main feedstock for biodiesel production includes rapeseed, soybean, oilseeds, palm oil, and animal fats [2].

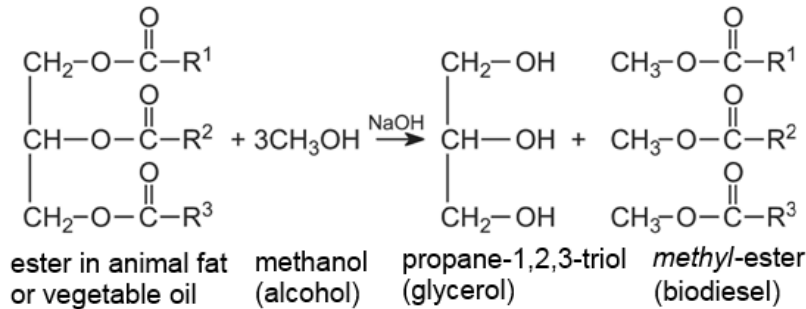


Figure 1.1: Reaction for transesterification process

In biodiesel, it is the presence of esters and fatty acids that influences ignitability and soot formation potential [10, 11]. There is a risk that the proportion of esters in the exhaust gas may increase, which may lead to negative health effects [10, 11]. The oxidation pathways that are responsible for these combustion characteristics can be studied using detailed kinetic mechanisms.

1.3 Objectives

The objective of this thesis work is to develop the kinetic mechanism of surrogates for biodiesel/diesel blends. These kinetic mechanisms can be further applied in three-dimensional engine simulations. The objectives are summarized as follows:

- 1) Improvement of the kinetic oxidation of *n*-decane
- 2) Improvement of the kinetic oxidation of AMN
- 3) Compilation of the *n*-decane and AMN blend and investigation of the fuel-fuel interaction between AMN and *n*-decane
- 4) Validation of the AMN/*n*-decane blend with the help of experimental studies of *n*-decane, AMN, and the IDEA blend
- 5) Comparison of the AMN/*n*-decane blend with diesel experiments
- 6) Improvement of the kinetic oxidation of MD

-
- 7) Application of chemistry-guided reduction to the MD mechanism
 - 8) Validation of the MD mechanism with the help of relevant experimental studies
 - 9) Comparison of the MD mechanism with biodiesel experiments
 - 10) Compilation of the *n*-decane/AMN/MD blend

1.4 Thesis organization

This thesis contains six chapters. The motivation and objectives were already introduced in this chapter.

The theoretical fundamentals, which include chemical kinetics, reaction mechanisms, analysis tools, physical and reactor modeling, will be explained in chapter 2. The concepts of rate law, combined with those of rate coefficient, elementary reaction, and chain reaction, as well as mechanism analyses will be covered concisely, followed by a short introduction of different reactors and mathematical descriptions.

With this knowledge of the theory, the approach used to develop an oxidation model will be depicted in chapter 3. The concepts of base mechanism, thermodynamic and transport data, and reduction approach will also be covered in this chapter.

The kinetic mechanism development of *n*-decane/ AMN will be discussed in chapter 4. The results of literature reviews for *n*-decane and AMN will be reported and reaction kinetics for both models will be discussed. Flow analysis and reaction analysis will be performed to show the fuel-fuel interaction between *n*-decane and AMN. Subsequently, the comparison between the mechanism and relevant experiments will be discussed.

The kinetic mechanism of MD will be investigated in chapter 5. The reaction kinetics for MD will be discussed in detail. Chemistry-guided reduction will be applied to the MD mechanism. The detailed and skeletal mechanism will be validated using available experiments. Flow analysis and sensitivity analysis will be performed using both the detailed and the skeletal model. The thesis introduces a new three-stage flow analysis in order to visualize flow pathways at different stages. The chapter ends with the comparison of the simulations and experiments for biodiesel fuels.

A conclusion and suggestions for future research will be provided in chapter 6.

2 Theoretical fundamentals

The theoretical fundamentals in the fields that are relevant to kinetic mechanisms will be presented in this chapter as shown in Figure 2.1. The mathematical equations in chapter 2.1, 2.3 and 2.5 are mainly referred from Warnatz [12]. The mathematical equations regarding to shock tube and jet stirred reactor (JSR) are cited from Miller and Kee [13].

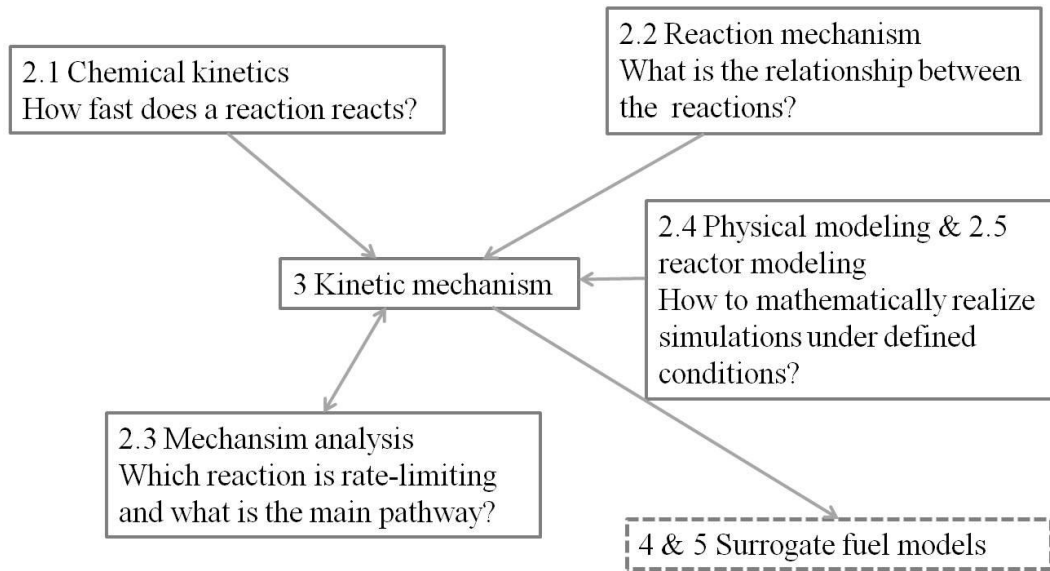


Figure 2.1: Schematic structure of theoretical fundamentals

2.1 Chemical kinetics

Chemical kinetics is the branch of chemistry that investigates how fast the amounts of products and reactants change during a reaction [14]. The term “kinetics” originally stems from the Greek word *kinesis*, meaning movement.

2.1.1 Rate law

An arbitrary elementary reaction with n species takes place as follows:



where R_i and P_i are symbols of the reactant and the product; ν_i' and ν_i'' are the stoichiometric coefficients of reactant R_i and product P_i , respectively; and N and M are the respective numbers of the chemical species. For each reaction, the stoichiometric number indicates the quan-

titative relationship among the substances as they participate in the reaction. Production shows up with a positive value, while consumption has a negative one.

The rate law, which is defined as an experimentally determined equation, can be used to study how fast a reaction takes place. More formally, the rate law is used to express the rate of a reaction in terms of molar concentration of species. Under the assumption of the law of mass action for one elementary reaction, the rate law of the forward reaction in equation 2.1 in terms of species c_i can be expressed as:

$$\left(\frac{dc_i}{dt}\right)_f = v_{i,f} k_f \prod_{i=1}^N c_{R_i}^{v'_i} \quad (2.2)$$

where $v_{i,f} = v''_i - v'_i$. c_{R_i} is the concentration of reactant species R_i ; k_f is the forward rate coefficient. For this elementary reaction, the reaction order of the i -th reactant species is equal to stoichiometric coefficient v'_i of the reactants. In the case of non-elementary reaction, the reaction order is usually calculated by experiments.

When applying the same rule for the reverse reaction in equation 2.1, the rate constant becomes:

$$\left(\frac{dc_i}{dt}\right)_r = v_{i,r} k_r \prod_{i=1}^M c_{P_i}^{v''_i} \quad (2.3)$$

where $v_{i,r} = v'_i - v''_i$; the reaction order of the i -th product species is equal to stoichiometric coefficient v''_i of the products and k_r is the reverse rate coefficient. When both the forward and the reverse reaction have the same reaction rates on the microscopic level, equilibrium is reached with no net reaction change on the macroscopic level:

$$\left(\frac{dc_i}{dt}\right)_f + \left(\frac{dc_i}{dt}\right)_r = 0 \quad (2.4)$$

Therefore,

$$v_{i,f} k_f \prod_{i=1}^N c_{R_i}^{v'_i} = -v_{i,r} k_r \prod_{i=1}^M c_{P_i}^{v''_i} \quad (2.5)$$

The equilibrium constants $K_{eq,c}$ (defined by molar concentrations) and $K_{eq,p}$ (by partial pressures), which represent the ratio of the rate constant, are respectively obtained:

$$K_{eq,c} = \frac{\prod_{i=1}^M c_{P_i}^{v''_i}}{\prod_{i=1}^N c_{R_i}^{v'_i}} \quad ; \quad K_{eq,p} = \frac{\prod_{i=1}^M p_{P_i}^{v''_i}}{\prod_{i=1}^N p_{R_i}^{v'_i}} \quad (2.6)$$

Meanwhile, the relationship between $K_{eq,c}$ and $K_{eq,p}$ is as following:

$$K_{eq,c} = K_{eq,p} / RT^{(\sum_{i=1}^M \nu_i'' - \sum_{i=1}^N \nu_i')} \quad (2.7)$$

Since $\Delta G(T) = \Delta G^0(T) + RT \ln(K_{eq,p})$ and the $\Delta G(T) = 0$ in equilibrium at corresponding temperature, therefore

$$K_{eq,p} = \exp\left(\frac{-\Delta G^0(T)}{RT}\right) \quad (2.8)$$

here $\Delta G^0(T)$, the standard molar Gibb's free energy, is the free energy of one mole of the gas at 1 bar of pressure and can be calculated by

$$\Delta G^0(T) = \Delta_R H(T) - T \Delta_R S(T) \quad (2.9)$$

where $\Delta_R H(T)$ is the molar enthalpy (in J/mol) of the reaction and $\Delta_R S(T)$ is the molar entropy (in J/(mol*K)) of the reaction.

In practice, it is useful to calculate the equilibrium constant and the easily measurable rate constant and then calculate the unknown rate constant using the equation 2.6.

2.1.2 Rate coefficient

The rate coefficient, which is crucial in the rate law, can be expressed as:

$$k = f[\text{temperature, concentration, ... , other quantities}]$$

where the concentration of the individual species and the temperature are the two main impact factors. Other quantities may also influence the reaction. For example, total pressure may play a role in gas phase reactions.

Temperature dependence of rate coefficients

In the gas phase, chemical reactions rely on temperature to a large extent as the collision behavior becomes more active at higher temperature (i.e., at a higher average kinetic energy level). Arrhenius (1889) summarized the empirical relationship between rate coefficient and temperature as the Arrhenius Law:

$$k = A * \exp\left[-\frac{E_a}{RT}\right] \text{ or } k = A * T^n * \exp\left[-\frac{E_a}{RT}\right] \quad (2.10)$$

where the pre-exponential factor A , or more specifically $A * T^n$, is a constant specific to each reaction with the same unit of k . T is the temperature and R , the universal gas constant. E_a is the activation energy. The reaction takes place only if the energy barrier, namely the activa-

tion energy, is exceeded as shown in Figure 2.2. Otherwise, no reaction takes place although two molecules collide with each other. In Figure 2.2, the reaction coordinate represents the changes in bond lengths and bond angles that occur as the chemical reaction proceeds from reactants to products.

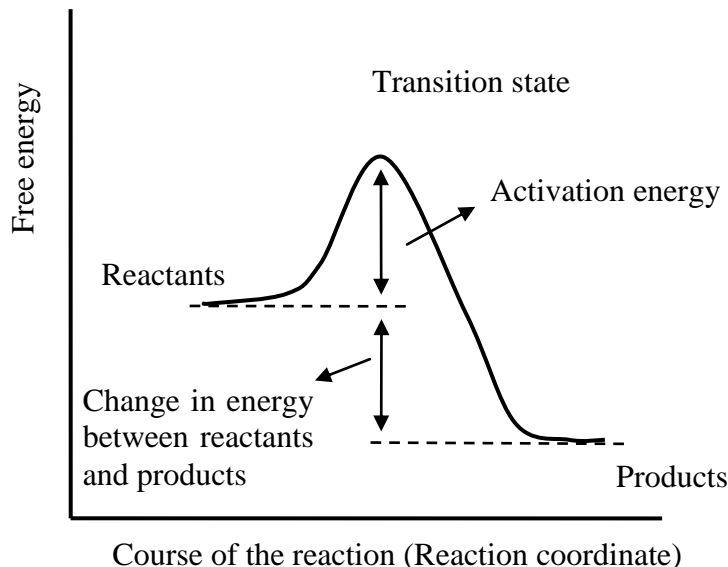


Figure 2.2: The energy profile of a chemical reaction

In practice, the Arrhenius plot is applied, where the natural logarithm of the rate coefficient is expressed versus the reciprocal temperature as in equation 2.10. The format of the Arrhenius plot avoids large calculation deviations resulting from possible measurement deviations.

$$\ln k = \ln A - \frac{E_a}{R} \left[\frac{1}{T} \right] \quad (2.11)$$

The Arrhenius law is the most common approach for describing reaction kinetics in which the rate coefficient of a specific elementary reaction is determined experimentally. In current study, the reaction rate is expressed following the Arrhenius law.

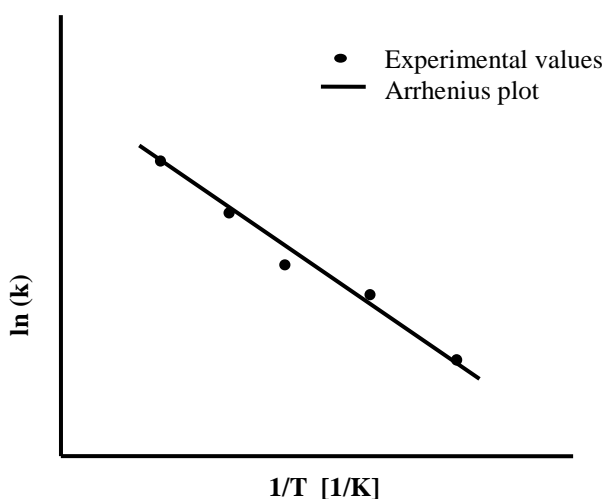
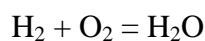


Figure 2.3: An example of an Arrhenius plot

2.2 Reaction mechanism

2.2.1 Elementary reaction

There are mainly two approaches for describing a chemical mechanism. One approach shows the overall relationship between the reactants and the final products. This is called a global reaction. For an H_2 - O_2 system, the global reaction can be expressed as follows:

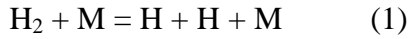


The global reaction shows a molar relation between reactants and products. However, the global reaction cannot provide any physical meaning. For an arbitrary reacting process, how reactants react with each other and what kind of intermediate species are produced contributes to the final products. Such detailed information is expressed by the elementary reactions that take place physically. An elementary reaction is defined as one that occurs on a molecular level exactly in the way described by the reaction equation [12].

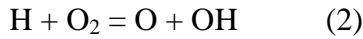
2.2.2 Chain reaction

One benchmark of combustion is the radical-chain reaction. The character of a radical-chain reaction is that the reactive intermediates produced in one step rapidly generate reactive intermediates in a subsequent step. Then the newly generated intermediates again produce other reactive intermediates, and so on [12]. Here the chain reactions in an H_2 - O_2 system are used as an example for investigating different types of chain reactions. Reaction processes for hydrocarbons are extensively discussed, for example, in “Hydrocarbons” by Pollard [15].

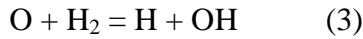
The fuel is H_2 and reacts with the respective oxidizer O_2 . Due to high activation energy, both molecules will not decompose spontaneously. However, due to the collision, a molecular species that can provide access energy may occur and bring the energy to the fuel molecules. This can be described as follows:



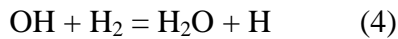
This is one typical chain initiation reaction and has a high activation energy E_a (in kJ/mole), which is provided by the third molecule M . M represents an unspecific molecule and is calculated from the sum of all species concentrations in the gas multiplied by their factors of effectiveness to carry the energy released or required. The H atom is a radical with one free bond, illustrated by a dot above the symbol. The H radical can react with the O_2 oxidant molecules and generate two new radicals.



The O radical has two free valence atoms, or two free bonds. The reaction produces more free bonds than it consumes and therefore it is called a chain-branching reaction. Similarly as an H radical, the O radical may react with the H_2 molecule in a chain propagation reaction as follows:

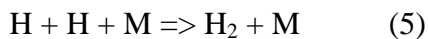


In the propagation reaction, the same number of free bonds is produced as has been consumed. The active OH radical can easily react with the fuel molecule and produce the product H_2O and an H radical:



When summing the reaction equations (2), the reactions (3), and two times of reactions (4) to form the overall reaction path, one free bond is consumed and three free bonds are produced. Hence, this reaction path is called a net chain-branching reaction.

Due to the chain-branching reaction, more and more H radicals are produced and the frequency of molecule collisions also increases under certain conditions. When two H radicals react with each other, they form an H_2 molecule and release part of their energy. If a third molecule can take away this energy, the following reaction may occur:



This reaction is called a chain-termination or chain-breaking reaction, a competitor of chain-branching reactions. If the chain-branching reaction exceeds the chain-breaking reac-

tion in a reaction system, an explosion will take place. In the opposite case, the reaction process is terminated. It can be observed that this reaction is the reverse of reaction equation (1).

Chain-branching reactions produce energy-rich radicals and they are endothermic reactions, i.e., they need energy from the system. When free radicals accumulate to such an extent that a chain-termination reaction may occur, this exothermic reaction will release energy to the system, causing an increase in temperature. The increased temperature may in turn yield a new chain-branching reaction since a sufficiently high-temperature can easily overcome the activation energy barrier. The concentration of radicals decreases because of the termination reaction and the temperature increases until the thermodynamic equilibrium of the system is finally reached.

2.3 Mechanism analysis

It is clear that some reactions have a greater impact on the overall reaction process while others have minor influence. Therefore, it is of interest to rank the importance of each reaction for reducing or improving the mechanism model.

2.3.1 Sensitivity analysis

Assuming a reaction mechanism consisting of R reactions and S species, the rate law can be expressed as follows [12]:

$$\frac{dc_i}{dt} = F_i(c_1, \dots, c_S; k_1, \dots, k_R), \quad c_i(t = t_0) = c_i^0, \quad i = 1, 2, \dots, S. \quad (2.12)$$

where c_i is the concentration of species i ; t , the time and c_i^0 , the initial concentration. k_1, \dots, k_R are the parameters of the system. Because it is of great importance to determine how each rate coefficient affects the overall reaction rate or a certain production, only rate coefficients other than the initial concentration and other properties are chosen as the parameters to be investigated.

Therefore, sensitivity is defined as the dependence of solution c_i on the parameters k_R ; absolute sensitivity and relative sensitivity [12] are defined, respectively, as:

$$E_{i,R}^{ab.} = \frac{\partial c_i}{\partial k_R} \quad (2.13)$$

$$E_{i,R}^{rel.} = \frac{k_r}{c_i} \frac{\partial c_i}{\partial k_R} \quad (2.14)$$

For instance, the relative sensitivity coefficient in the reaction $A \xrightarrow{k_1} I \xrightarrow{k_2} B$ is plotted in Figure 2.4.

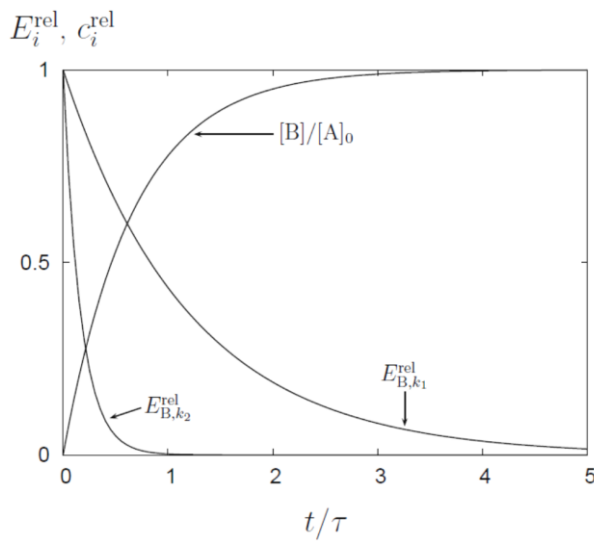


Figure 2.4: An example of relative sensitivity coefficients [12]

It is obvious that reaction $A \xrightarrow{k_1} I$ has a much larger impact relevant to time when compared with reaction $I \xrightarrow{k_2} B$. As a result, the rate limiting reaction is reaction $A \xrightarrow{k_1} I$. Hence, the chemical kinetics of reaction $A \xrightarrow{k_1} I$ is worthy of more investigation.

When the most sensitive reactions are collected, an overall sensitive analysis is obtained. Figure 2.5 illustrates the overall sensitivity analysis for ignition delay times in a shock tube with stoichiometric *n*-decane/air mixtures at 1100 K. The sensitive analysis clearly indicates how each reaction influences the overall reactivity.

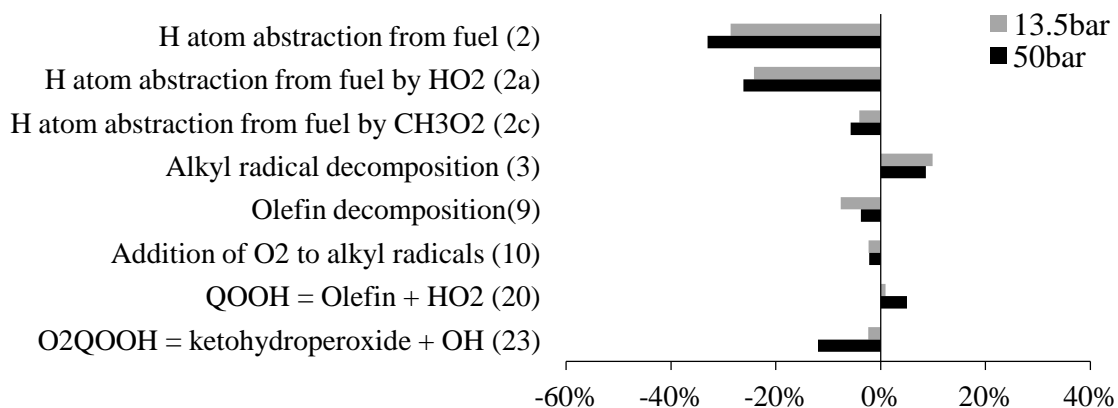


Figure 2.5: An example of a sensitivity analysis

2.3.2 Reaction flow analysis

Reaction flow analysis is performed in order to describe the importance of certain paths in the mechanism under specified conditions. It is performed by calculating the transfer rate of certain atomic species such as C, O, and H. The reaction flow of atomic species a between species j and species k in the i th elementary reaction can be described simply by [16],

$$f_{jk}^a = \sum_{i=1}^I r_i (n_j^a v_{j,i}'' - n_k^a v_{k,i}') \quad (2.15)$$

where the sum is calculated over the set of I reactions. n_j^a and n_k^a are the numbers of atom a in molecules j and k , and $v_{j,i}''$ and $v_{k,i}'$ are the stoichiometric coefficients for molecules j and k in the i th reaction.

2.4 Physical modeling

Once the elementary reactions and their corresponding rate coefficients have been determined, we combine these reactions through a set of differential equations describing the concentration evolution of various species during the combustion process, thus representing the species conservation equation. The species conservation equation is often defined in terms of the molar fraction, X_i , or the mass fraction, Y_i , of the following form:

$$\frac{\partial \mathbf{Y}}{\partial t} + \mathbf{P}(\mathbf{Y}, \mathbf{v}, T) + \omega(\mathbf{Y}, T) = 0 \quad (2.16)$$

where $\mathbf{P}(\mathbf{Y}, \mathbf{v}, T)$ represents the spatial differential operator (advection, convection, and diffusion), which is dependent on the velocity field, \mathbf{v} , and the temperature, T . The $\omega(\mathbf{Y}, T)$ is the chemical source term (i.e., the chemical production and consumption of the species). \mathbf{Y} is the N -dimensional vector of the mass fraction for a mechanism containing N species.

2.5 Reactor modeling

2.5.1 Shock tube

In purely thermal ignition processes, the reaction begins and the temperature increases at once; however, in explosions of hydrogen or hydrocarbon-air mixtures, an explosion takes place only after a certain induction time (i.e., the ignition delay time) despite the rise in temperature [12]. The ignition delay is very characteristic in radical-chain explosions where radi-

cals are accumulating during ignition delay (in Figure 2.6) until the radical pool grows large enough to consume a significant fraction of the fuel and then rapid ignition occurs [12].

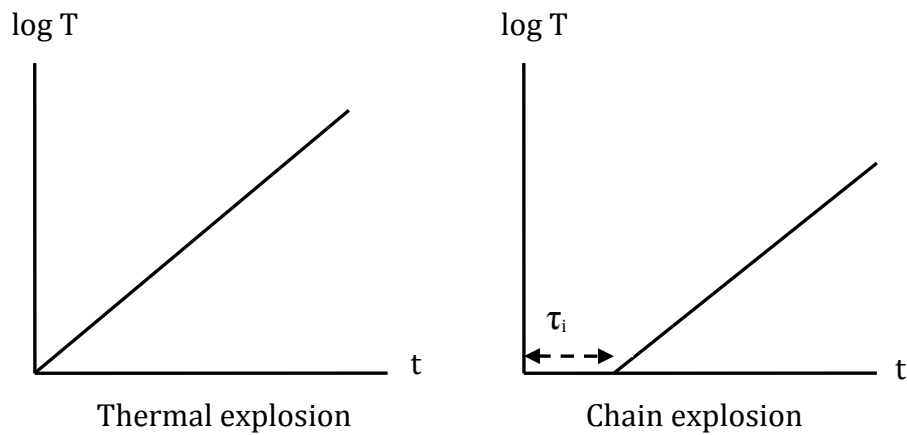


Figure 2.6: Time behaviors of thermal and chain explosion in an adiabatic system [12]

Ignition delay is dependent on initial pressure, temperature, and mixture composition; therefore, the compositions of species can be reflected by measuring the dependence of ignition delay on temperature. As a result, the calculation of the ignition delay time is a powerful tool for modeling and understanding the combustion mechanism of a given fuel. There exist different specified definitions of induction time, depending on the application of various criteria such as fuel consumption, carbon monoxide formation, formation of hydroxyl radicals, pressure increase in a constant-volume vessel, temperature increase in an adiabatic vessel, etc. A shock tube is commonly used to obtain the rate coefficient under one-dimensional conditions since it achieves a nearly one-dimensional flow with practically instantaneous heating of the reactants.

In the simplest skeleton [17] as shown in Figure 2.7, the space marked with (1) denotes the initial test gas, (2) the shocked gas, (3) the driver gas behind the contact surface, (4) the initial driver gas, (5) the test gas subjected to reflected shock. The shock tube consists of a uniform cross-section tube divided into a driver and a driven section, separated by a diaphragm. The driver section is filled with a low-molecular-weight gas (such as hydrogen or helium) with high pressure; in the driven section, the gas whose physical or chemical properties at high-temperature are under investigation is at low pressure. When the diaphragm is burst by the driver gas, a normal shock wave propagates down the driven section and heats the investigated gas.

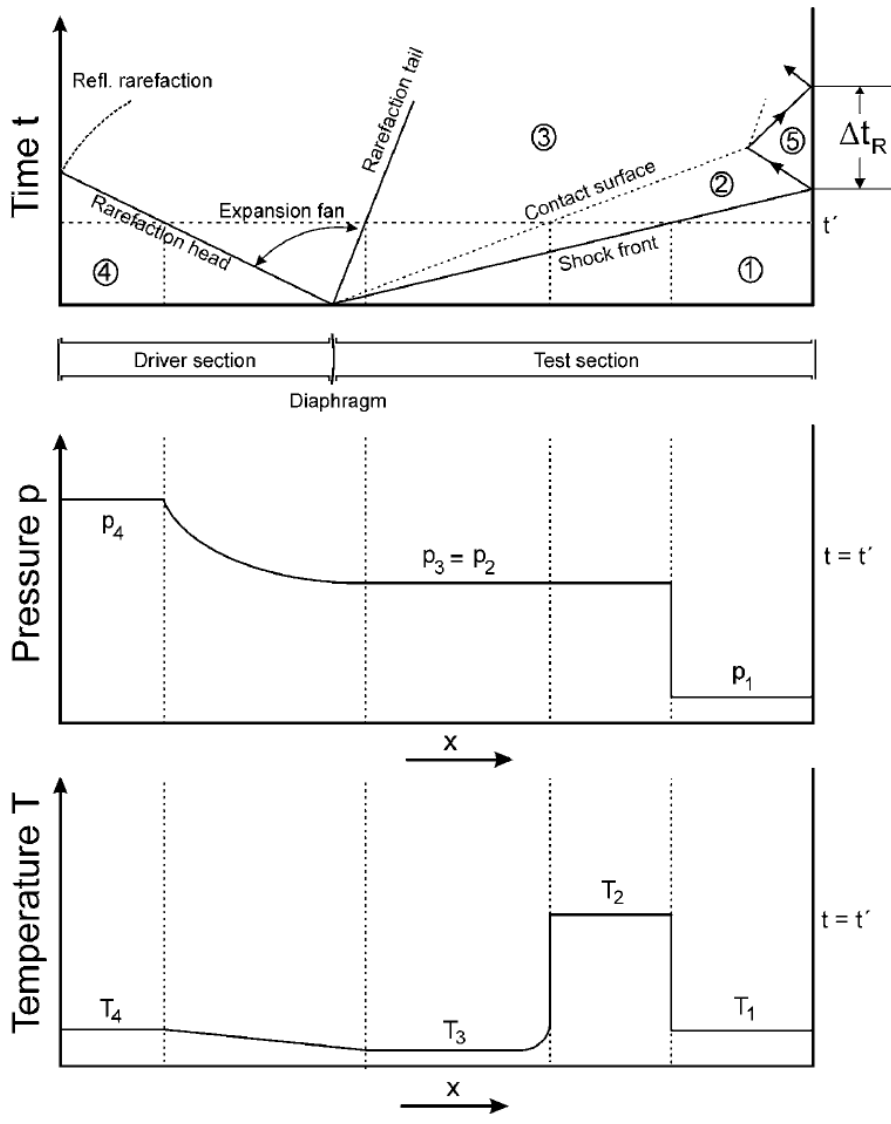


Figure 2.7: x-t diagram of a simple shock tube [17]

The incident shock is reflected at the end of the test section and rams into the shocked gas flowing behind it, which leads to a further increase in the temperature and pressure of the investigated gas. Correspondingly, the rarefaction wave, which travels in a direction opposite to that of the incident shock, is reflected from the end of the driver section and moves towards the testing gas. The rarefaction fan, bounded by the head and tail of the rarefaction zone, is characterized by falling temperature and pressure (p_3, T_3) below the initial conditions (p_4, T_4), as shown in Figure 2.7.

When the diluted fuel-oxygen mixture is effectively compressed and heated instantaneously in the shock tube, the reaction occurs after the ignition delay, which occurs in a simple initial condition for the modeling. The spatial uniformity of the stationary heated test gas mixture behind the reflected shock waves means that only the chemistry needs to be modeled, and fluid mechanical effects such as diffusion, mixing, and fluid movement are not significant

in most cases. The time scales and physical dimensions of shock tube experiments mean that the test gas volume can be considered adiabatically isolated from its surroundings.

Shock tube experiments can provide test conditions over a wide range of temperatures, pressure and gas mixtures, typically over temperatures of 600 K to 4000 K, pressures from sub-atmospheric to 1000 atm, and fuel concentrations from ppm to percentage levels with test times in the 1-10 ms range. Methods can be developed to extend these ranges if needed.

The reactor model is assumed to have a constant volume where pressure is allowed to rise. Since no mass flows in or out of the system and since mass cannot be created, the conservation equation of species is valid. The conservation equations of energy and the equation of state are applied during numeric calculation. The constant volume and homogeneous adiabatic conditions behind the reflected shock wave in the simulation software “LOGEsoft” are used to perform all the simulations for the shock tube and other kinds of reactors. Therefore, the corresponding differential equations describing the time evolution of a chemical reaction (N species participating in I elementary steps) under adiabatic, constant volume conditions are the following:

Conservation of species

$$\frac{\partial Y_n}{\partial t} = \frac{\dot{\omega}_n}{\rho} \quad (n = 1, \dots, N) \quad (2.17)$$

where Y_n is the mass fraction of the n th species, t is the time, and ρ is the (constant) mass density. $\dot{\omega}_n$ is the mass rate of production of the n th species by chemical reaction. As explained in chapter 2.1, one can generally write $\dot{\omega}_n$ as:

$$\dot{\omega}_n = W_n \sum_{i=1}^I (v''_{n,i} - v'_{n,i}) \left\{ k_{f,i} \prod_{l=1}^N [c_l]^{v'_{l,i}} - \frac{k_{f,i}}{K_{eq,i}} \prod_{l=1}^N [c_l]^{v''_{l,i}} \right\} \quad (2.18)$$

Where W_n is the molecular weight of the n th species, $k_{f,i}$ is the forward rate coefficient of the i th elementary chemical reaction, $K_{eq,i}$ is the equilibrium constant (in terms of concentrations) of the i th reaction, $[c_l]$ is the molar concentration of the l th species, and $v'_{l,i}$ and $v''_{l,i}$ are the reactant and product stoichiometric coefficients of the l th species in the i th reaction.

Conservation of energy

$$c_v \frac{\partial T}{\partial t} = - \frac{1}{\rho} \sum_{n=1}^N e_n \dot{\omega}_n \quad (2.19)$$

where T is the temperature, e_n is the internal energy per unit mass of the n th species (including a contribution from the heat of the formation) and c_v is the specific heat capacity at constant volume.

Equation of state

$$p = \frac{\rho RT}{\bar{W}} \quad (2.20)$$

where p is the pressure, R is the universal gas constant. $\bar{W} = \sum_{n=1}^N X_n W_n$ is the mean molecular weight of the mixture.

2.5.2 Jet stirred reactor

A JSR (or continuously stirred tank reactor) as an ideal reactor is considered to achieve perfect mixing. With a constant input and output stream, the reaction is under a steady state, i.e., the compositions of species do not change with time. Therefore, the stirred reactor is a suitable approach for investigating the evolution of chemical species in a large range of reaction extents including the induction period.

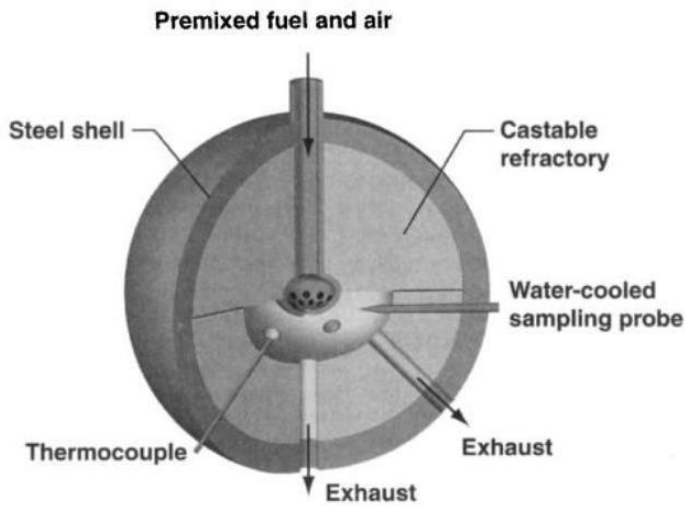


Figure 2.8: Schematic diagram of a jet-stirred reactor [18]

A schematic diagram of a JSR with hemispherical geometry [18] is shown in Figure 2.8. The reactor itself consists of a chamber that is insulated from the surroundings. The pre-mixed fuel/air mixtures are injected through numerous radial nozzles and enter the reactor zones as small sonic jets. Therefore, due to high-intensity turbulent mixing, temperature and concentrations can ideally be assumed to be homogeneously distributed. The rapid mixing

thus results in sampled compositions that are purely kinetically controlled. The (mean) residence time can be determined by varying the inlet mass flow rate.

The perfectly stirred reactor model in the simulation software “LOGEsoft” is applied to simulate a jet stirred reactor. A JSR can be regarded as a vessel in which there is extremely strong mixing, giving rise to steady state solutions of balance equations.

The corresponding differential equations describing the time evolution of a chemical reaction (N species participating in I elementary steps) in the JSR, written in transient form, are as follows:

Conservation of species

$$\frac{\partial Y_n}{\partial t} = \frac{Y_{n,0} - Y_n}{\tau} + \frac{\dot{\omega}_n}{\rho} \quad (n = 1, \dots, N) \quad (2.21)$$

Conservation of energy

$$c_p \frac{\partial T}{\partial t} = \frac{1}{\tau} \sum_{n=1}^N Y_{n,0} (h_{n,0} - h_n) - \frac{1}{\rho} \sum_{n=1}^N h_n \dot{\omega}_n \quad (2.22)$$

in both of the above equations, the subscript 0 indicates inlet conditions; non-subscript variables represent the reactor and exhaust conditions. The mean residence time of the fluid in the reactor, τ , is related to the (constant) mass flow rate through the reactor, \dot{m} , and the reactor volume, V , through the relation

$$\tau = \rho V / \dot{m} \quad (2.23)$$

Equation of state

$$p = \frac{\rho R T}{\bar{W}} \quad (2.24)$$

where p is the pressure, R is the universal gas constant. $\bar{W} = \sum_{n=1}^N X_n W_n$ is the mean molecular weight of the mixture.

2.5.3 Laminar, one-dimensional, premixed flame

A laminar premixed flame is a common laboratory-scale, macroscopic reactor. The flames are normally stabilized on top of porous metal cylinders through which the reactants are fed as shown in Figure 2.9. The flame is usually operated at low pressure or atmospheric pressure.

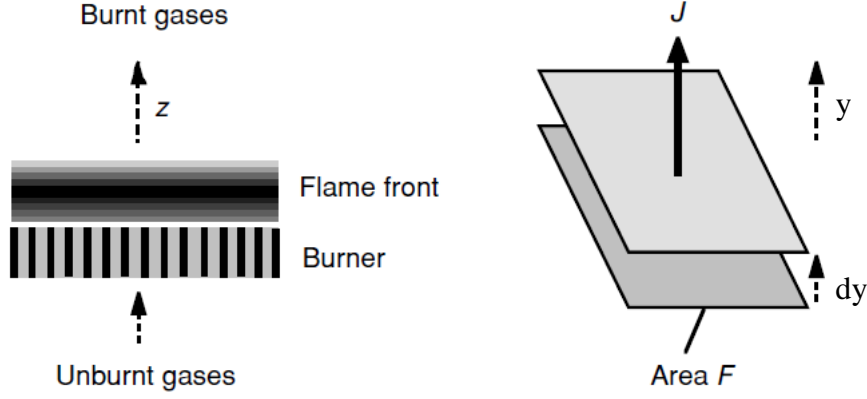


Figure 2.9: Schematic illustration of a laminar premixed flat flame [12]

The differential equations describing the species and energy by Mauß [19] can be written as follows:

Continuity equation

$$\rho v = (\rho v)_u = \text{const.} \quad (2.25)$$

Conservation of species

$$\rho v \frac{\partial Y_n}{\partial y} = - \frac{\partial}{\partial y} (\rho Y_n v_n) + \dot{\omega}_n \quad (n = 1, \dots, N) \quad (2.26)$$

where ρ is the mass density, v is the velocity, Y_n is the mass fraction of n th species, v_n is the diffusion velocity of the n th species, and $\dot{\omega}_n$ is the molar rate of production of n th species by chemical reaction.

Conservation of energy

$$\rho v c_p \frac{\partial T}{\partial y} = \frac{\partial}{\partial y} \left(\lambda \frac{\partial T}{\partial y} \right) - \frac{\partial T}{\partial y} \sum_n^N c_{p,n} \rho Y_n v_n - \sum_n^N h_n \dot{\omega}_n - q_r = 0 \quad (n = 1, \dots, N) \quad (2.27)$$

where λ denotes the heat conductivity of the mixture, c_p is the specific heat capacity of the mixture at constant pressure, $c_{p,n}$ is the specific heat capacity of n th species at constant pressure, h_n denotes the specific enthalpy of the n th species, q_r is the sink term due to radiation and discussed in next section.

Equation of state

$$p = \frac{\rho R T}{\bar{W}} \quad (2.28)$$

where p is the pressure, R is the universal gas constant. $\bar{W} = \sum_{n=1}^N X_n W_n$ is the mean molecular weight of the mixture.

2.5.4 Free propagating flame

In an opposed-jet burner, fuel and air are brought together by convection where they mix due to diffusion as shown in Figure 2.10.

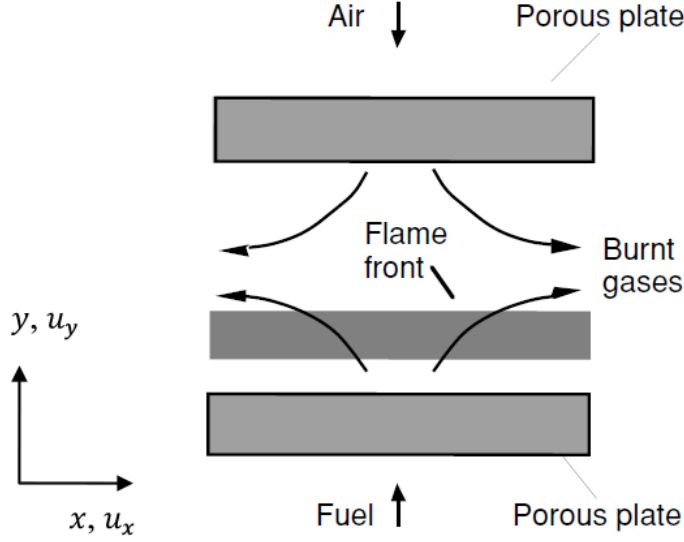


Figure 2.10: Schematic illustration of counter flow flames in an opposed-jet burner [12]

Since the flame is parallel to the unburnt layer, all the properties are dependent on the coordinate y alone. Therefore the simplified one-dimension equations by Mauß [19] are as following:

Conservation of momentum and total mass

$$\rho G + \frac{\partial(\rho v)}{\partial y} = 0 \quad (2.29)$$

$$\rho G^2 + \rho v \frac{\partial G}{\partial y} = -H + \frac{\partial}{\partial y} \left(\mu \frac{\partial G}{\partial y} \right) = 0 \quad (2.30)$$

where $G = u/x$, u is the tangential velocity, μ is the viscosity, and $H = \frac{1}{x} \frac{\partial P}{\partial x} = \text{const.}$

Conservation of species

$$\rho v \frac{\partial Y_n}{\partial y} = -\frac{\partial}{\partial y} (\rho Y_n v_n) + \dot{\omega}_n \quad (n = 1, \dots, N) \quad (2.31)$$

where ρ is the mass density, v is the velocity, Y_n is the mass fraction of n th species, v_n is the diffusion velocity of the n th species, and $\dot{\omega}_n$ is the molar rate of production of n th species by chemical reaction.

Conservation of energy

$$\rho v c_p \frac{\partial T}{\partial y} = \frac{\partial}{\partial y} \left(\lambda \frac{\partial T}{\partial y} \right) - \frac{\partial T}{\partial y} \sum_n^N c_{p,n} \rho Y_n v_n - \sum_n^N h_n \dot{\omega}_n - q_r = 0 \quad (n = 1, \dots, N) \quad (2.32)$$

where T denotes the temperature, c_p is the specific heat capacity of the mixture at constant pressure, $c_{p,n}$ is the specific heat capacity of n th species at constant pressure, λ is the heat conductivity of the mixture, and h_n is the specific enthalpy of n th species.

Diffusion velocity v_n and the sink term q_r

For the diffusion velocity v_n in the equations (2.26, 2.27, 2.31 and 2.32), its one-dimensional expression [19] is as following:

$$v_n = v_{D,n} + v_{T,n} + v_{C,n} \quad (2.33)$$

where $v_{D,n}$ is the mass flux due to the concentration gradients; $v_{T,n}$ is diffusion of mass caused by temperature gradients, and $v_{C,n}$ is the correction term.

For mixtures, empirical laws are applied for the diffusion of a compound n with the binary diffusion coefficients D_n :

$$v_{D,n} = - \frac{D_n}{X_n} \frac{\partial X_n}{\partial y} \quad (2.34)$$

$$D_n = - \frac{1 - Y_n}{\sum_{j=1, j \neq n}^N X_j / D_{n,j}} \quad (2.35)$$

For diffusion of mass by temperature gradient $v_{T,n}$,

$$v_{T,n} = - \frac{D_n t_n^T}{X_n} \frac{1}{T} \frac{\partial T}{\partial y} \quad (2.36)$$

where t_n^T is thermal diffusion coefficient.

Additionally the total diffusion flux $\sum_{n=1}^N Y_n v_n = 0$ is fulfilled by the correction term $v_{C,n}$.

The heat loss, q_r in the equations (2.27 and 2.32), are described by the Stefan–Boltzmann law:

$$q_r = 4\sigma_s T^4 (\alpha_{p,CO_2} p_{CO_2} + \alpha_{p,H_2O} p_{H_2O} + \alpha_{p,sv}) \quad (2.37)$$

where the $\sigma_s = 5.669 * 10^{-8}$ (in $\text{Wm}^{-2}\text{K}^{-4}$) is the Stefan-Boltzmann constant; p_{H_2O} and p_{CO_2} (in Pa) are the respective partial pressures for H_2O and CO_2 ; f_v is the soot volume fraction and further detailed information can be found in the Mauß [19]. The other three Planck absorption coefficients are referred as following [19]:

$$\alpha_{p,CO_2} = 46.241 \exp(-8.888 * 10^{-4}T) \quad (2.38)$$

$$\alpha_{p,H_2O} = 22.6 \exp(-1.546 * 10^{-3}T) \quad (2.39)$$

$$\alpha_{p,s} = -3.75 * 10^5 T + 1.735 * 10^3 T \quad (2.40)$$

3 Fundamentals of kinetic mechanisms

In the past, Warnatz proposed five steps that are necessary to develop a kinetic mechanism for the oxidation of hydrocarbons [20]:

1. Collection of all available experimental data on the elementary reactions involved in the $\text{H}_2\text{-O}_2\text{-CO-C}_1\text{-C}_2$ system
2. Extension of these data to higher hydrocarbons with the help of group additivity rules
3. Test of these rate data with the help of experimental results in typical, but simple (0D, 1D) combustion situations: ignition, flame propagation, flame structure, etc.
4. Modification of rate coefficients within the range of their error limits to reproduce the data on ignition, flame propagation, flame structure, etc.
5. The most dangerous last step: addition of missing reactions using estimates of the rate coefficients

However, with more and more advanced measurement technologies and updated experimental and simulation database, the majority of these five steps are becoming realizable and furthermore improved as following:

1. Collection of all available experimental data on the elementary reactions involved in the $\text{H}_2\text{-O}_2\text{-CO-C}_1\text{-C}_2\text{-C}_3\text{-C}_4$ system with important aromatic species (benzene and toluene). The oxidation model of toluene is proved to be important for modeling fuel rich oxidation process.
2. Extension of these data to higher hydrocarbons with the help of quantum chemistry
3. Test of these rate data with the help of experimental results in diverse combustion situations: ignition, flame propagation, flame structure, etc.
4. The reaction rates for most important reactions are determined by precise experimental measurements or theoretical studies.

3.1 Base mechanism

It is undoubted that any detailed hydrocarbon kinetic mechanism starts from the kinetic mechanism of O_2/H_2 and CO/CO_2 systems. Both systems include strong chain-branching or chain-breaking reactions, which dominate the rate of combustion, the ignition delay times, or the flame speeds with any type of hydrocarbon as fuel. One ubiquitous example is the chain-branching reaction between a hydrogen atom and an oxygen molecule [21]: $\text{H} + \text{O}_2 = \text{OH} +$

O. This reaction is primarily responsible for whether a gas mixture will burn or how fast it will burn.

Except for O₂/H₂ and CO/CO₂ systems, many small hydrocarbon species are also important for building detailed hydrocarbon kinetics. In the past, Warnatz and colleagues [12, 22, 23] developed a widely used mechanism for the oxidation of C₀-C₄ hydrocarbon fuels, which was validated for flame speeds, ignition delay times, and species concentration profiles. In 1987, Frenklach and Warnatz presented a kinetic model predicting PAH (polyaromatic hydrocarbon) concentration profiles in sooting acetylene flames [24]. Ten years later, Wang and Frenklach published a GRI-based detailed reaction mechanism describing fuel oxidation, benzene formation, and PAH mass growth [25] as the most extensive study on soot formation in C₂ flames. Later, the C₀-C₄ mechanism with oxidation of benzene by Hoyermann et al. [26] (which is called a “base mechanism”) was compiled from the above-mentioned mechanism of Warnatz et al. [12, 22, 23] and that of Wang and Frenklach. [24]. This compiled base mechanism includes O₂/H₂, CO/CO₂, CH₄, C₂H₆, C₃H₈, *n*-C₄H₁₀, C₂H₄, C₃H₆, C₂H₂, and benzene. Their paper demonstrates that this base mechanism has been improved as an optimal C₀-C₄ mechanism with a broader target validation range. This approach was confirmed by a study of Qin et al. [27] for C₃ fuel oxidation, in which simultaneous optimization of the kinetics of small and intermediate sized fuels was necessary to obtain optimal C₃ data.

Following this strategy and applying base mechanism by Hoyermann et al. [26] as the starting mechanism, the oxidation of toluene [28], butane isomers [29], and butene isomers [30] was compiled gradually. Once a new fuel component was added to the base mechanism, the compiled base mechanism was treated as a new model and validated for the target range of the old fuel pool being augmented by the targets for the new fuel. This can avoid compensation errors or build-up errors and assure the same sensitive kinetic parameters in the base mechanism. Therefore, with continuous compilation of necessary and important new species, the hierarchically constructed base mechanism is considered as a strong basis for developing any complex oxidation process. The base mechanism was validated against the measured low-pressure flame speciation data, laminar flame speeds at different pressures, as well as ignition delay time measurements and species composition results from jet stirred reactors. Detailed information about the literature sources of kinetic and thermodynamic properties for the reactions and species of the present model is provided in the published paper [30].

3.2 Extension strategy

Linear *n*-alkanes, as the simplest components, provide the fundamentals of fuel modeling in the case of more complicated components. *n*-alkanes or a blending of *n*-alkanes are by far the best studied class of compounds for which reliable, detailed chemical kinetic models for combustion exist. They are assumed to be a suitable surrogate component for practical fuels.

In the past, the first extension of the base mechanism was the inclusion of *n*-heptane oxidation by Ahmed [31] since *n*-heptane is an important benchmark fuel for the mechanisms of higher hydrocarbons appearing in model fuels, e.g. *n*-decane, *n*-dodecane, *n*-tetradecane, etc. Figure 3.1 shows the extension strategy for different fuels. Hereafter, the oxidation of 1-hexene [32] as an *n*-alkene was developed. Other fuels compiled by different authors include updated *n*-heptane [33], *n*-hexane [34], iso-octane [35], cyclohexane, methyl-cyclohexane [36], etc. Current study focuses on the oxidation of AMN/*n*-decane and MD and a discussion of mechanism kinetics will be presented in the next two chapters.

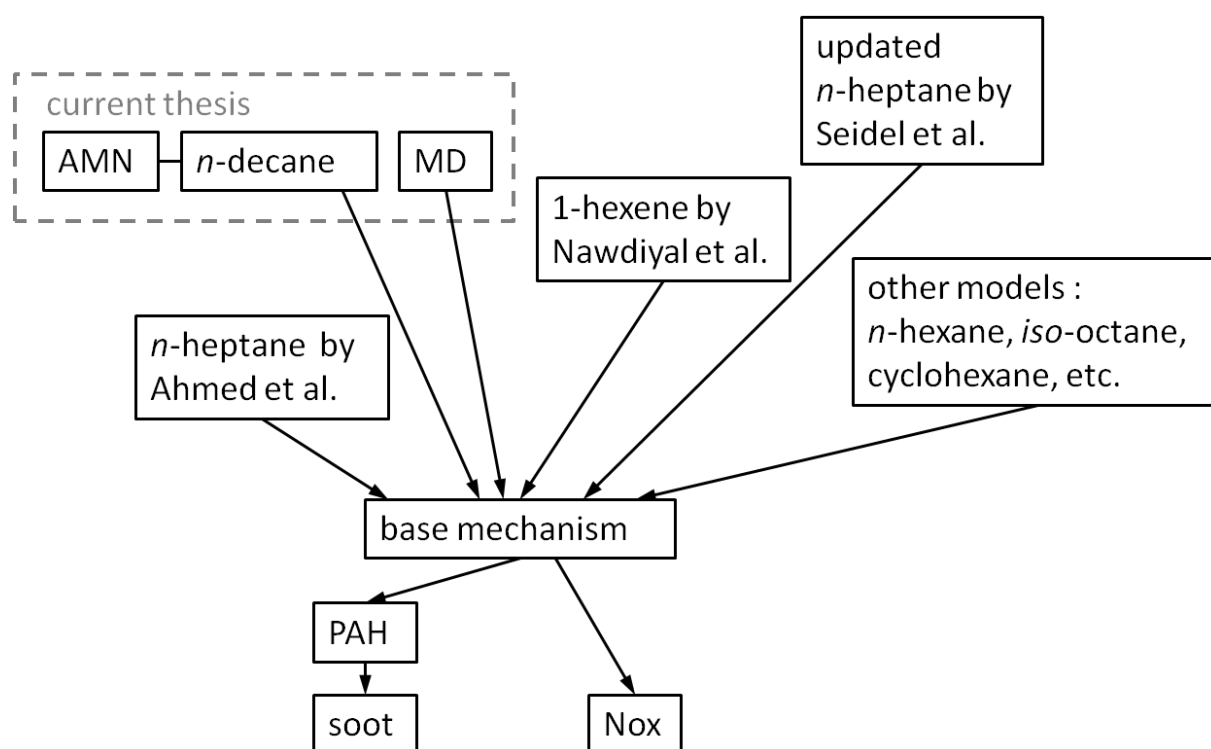


Figure 3.1: The extension strategy for different fuels

3.3 Thermodynamic and transport properties

Thermodynamic properties

For the description of the conservation equation for different reactors in chapter 2.5, several thermodynamic and transport properties (i.e., enthalpy, entropy, and heat capacity) are needed for the solution of the conservation equation. The concept of thermochemistry was originally proposed a hundred years ago and from then on, many pioneers devoted themselves to developing the study of thermodynamic properties [37]. Among them, Lewis and Randal put forward the polynomials proposal, which expresses thermal chemical properties including heat capacity (C_p), enthalpy (H), etc. as a function of temperature in a compact and clear way suitable for computer calculation. The well-known 7-coefficient NASA polynomials have the following format [37]:

$$\frac{C_p}{R} = a_1 + a_2 T + a_3 T^2 + a_4 T^3 + a_5 T^4 \quad (3.1)$$

$$\frac{H}{RT} = a_1 + \frac{a_2}{2} \cdot T + \frac{a_3}{3} T^2 + \frac{a_4}{4} T^3 + \frac{a_5}{5} T^4 + \frac{a_6}{T} \quad (3.2)$$

$$\frac{S}{R} = a_1 \ln T + a_2 T + \frac{a_3}{2} T^2 + \frac{a_4}{3} T^3 + \frac{a_5}{4} T^4 + a_7 \quad (3.3)$$

where a_1, a_2, \dots, a_7 are the numerical coefficients in NASA thermodynamic files.

There are two temperature regions of the NASA polynomials where the T_{int} point coincides with both polynomials [37]. The high-temperature region ranges from T_{int} to T_{max} (usually 1000 – 5000 K) while the low-temperature region T_{min} to T_{int} is around 300 – 1000 K. In total, there are 14 numerical coefficients.

One example of standard thermodynamic data from two 7-coefficient NASA polynomials is shown in Figure 3.2. The first row consists of the name of the species, the composition, the phase condition (solid, liquid, gas), and two temperature regions with three temperatures ($T_{min}, T_{int}, T_{max}$). Subsequent the first set of seven numerical coefficients belongs to the high-temperature polynomial. The rest set of seven numerical coefficients is corresponding to the low-temperature polynomial.

```

H          H 1 0 0 0 298.000 5000.000 1000.00 1
0.25000000D+01 0.00000000D+00 0.00000000D+00 0.00000000D+00 0.00000000D+00
0.25471620D+05-0.46011760D+00 0.25000000D+01 0.00000000D+00 0.00000000D+00
0.00000000D+00 0.00000000D+00 0.25471620D+05-0.46011760D+00
H2        H 2 0 0 0 298.000 5000.000 1000.00 1
0.29914230D+01 0.70006440D-03-0.56338280D-07-0.92315780D-11 0.15827519D-14
-0.83503400D+03-0.13551101D+01 0.32981240D+01 0.82494410D-03-0.81430150D-06
-0.94754340D-10 0.41348720D-12-0.10125209D+04-0.32940940D+01

```

Figure 3.2: Example of the standard format of 7-coefficient NASA polynomials

Transport properties

The transport properties (viscosity, thermal conductivity, and diffusion) describe the transport of physical properties due to movement in the gas phase. To account for intermolecular interaction, the Lennard-Jones-6-12 potential model is used, which is characterized by the molecular diameter σ and the depth of the intermolecular potential ε . σ and ε are used to determine the reduced collision integrals $\Omega^{(1,1)*}$ and the collision integrals $\Omega^{(2,2)*}$, which are factors accounting for the deviation from the model of rigid elastic spheres [12].

One example of transport data file used here is shown in Figure 3.3. The file lists seven columns and the column (from left to right) represents the following variable as:

- Chemical name
- Indicator for the structure of the species (0 = atom, 1 = linear molecule, 2 = non-linear molecule)
- Two parameters describing the shape of the Lennard-Jones potential well: well depth divided by Boltzmann's constant [K] and collision diameter σ [nm]
- The bond dipole moment [D]
- The polarizability [nm]
- The rotational collision number (Z_{ROT}) at 298 K

H	0	145.0	2.05	0.0	0.0	0.0
O	0	80.0	2.75	0.0	0.0	0.0
OH	1	80.0	2.75	0.0	0.0	0.0
HO2	2	107.0	3.46	0.0	0.0	1.0
H2O2	2	107.0	3.46	0.0	0.0	3.8
CH	1	80.0	2.75	0.0	0.0	0.0
HCO	2	498.0	3.59	0.0	0.0	0.0
CH2-1	1	144.0	3.8	0.0	0.0	0.0
CH2-3	1	144.0	3.8	0.0	0.0	0.0

Figure 3.3: Example of standard format of molecular data

3.4 Chemistry-guided reduction (CGR)

The direct usage of detailed surrogate fuel mechanisms in simulations with complex reactor models, e.g. for turbulent flow, is limited by the large number of species and elementary steps involved. Studying critical combustion aspects like NO_x and soot formation makes the problem even more severe. The use of reduced models is therefore necessary.

The detailed and reduced oxidation of target fuels, together with NO_x, soot formation mechanisms, or other fuels can be compiled using the existing base mechanism. This methodology is illustrated in Figure 3.4.

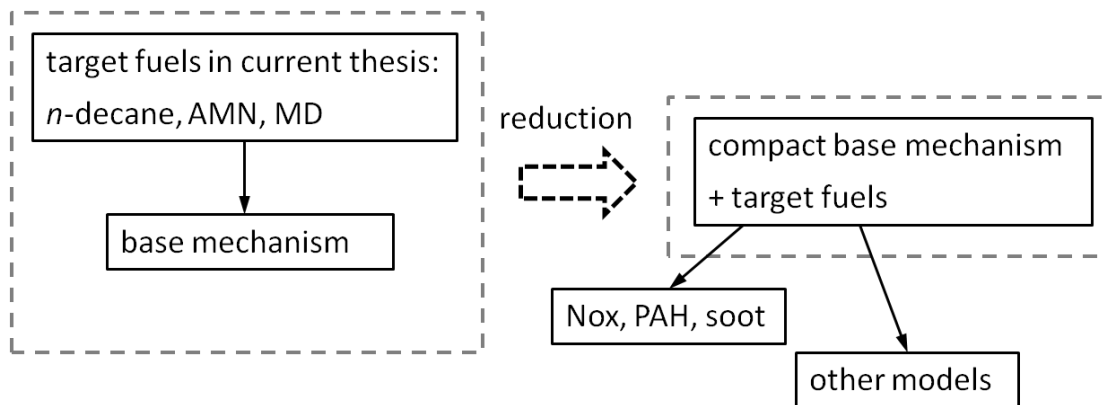


Figure 3.4: Schematic illustration of mechanism development

There are many reduction approaches, either employing chemistry or using a purely mathematical procedure [38-42], in which the chemistry-guided reduction approach (CGR) [43], which keeps the chemistry information, is proposed and applied in our group. In brief, CGR is the combination of chemical lumping and necessity analysis. It facilitates the reduction of the mechanism and is aimed at the development of a comprehensive skeletal mechanism. In the past, the CGR reduction approach has been applied for model reduction of *n*-heptane mechanism [43] and *n*-heptane/toluene mechanism [28]. MD as the first ester species is applied using CGR for the reduction, which is one of the tasks in this thesis work. In chapter 5, the reduction process of MD is depicted in detailed steps.

4 Kinetic mechanism for the blends of AMN/*n*-decane

In the past, a surrogate fuel consisting of 70% *n*-decane/30% α -methylnaphthalene (by liquid volume) was formulated as part of the Intergrated Development on Engine Action (IDEA) program [1]. Following this concept, the blends of AMN/*n*-decane are comprehensively discussed in this chapter.

4.1 Mechanism development for *n*-decane

As one component of commercial fuels, *n*-decane is a typical *n*-alkane with a ten-carbon chain. Since it has a strong NTC, it is commonly considered as a surrogate fuel or one component in surrogate fuel blends for diesel fuels [44], jet fuels [45], or biodiesel fuels [46].

A number of experimental investigations have been performed regarding *n*-decane oxidation, with global combustion characteristics such as ignition delay times [47-53] and flame speeds [54-58] being examined. Speciation during *n*-decane combustion has been studied in JSR [45, 59-61], plug flow reactors [62, 63], and premixed flames [64, 65]. The mechanism model of *n*-decane has been investigated for different purposes. Several *n*-decane models [62, 65, 66] have been developed for high-temperature oxidation alone. However, low-temperature oxidation is crucial for applications in auto-ignition-based engine concepts. Comprehensive models for both high- and low-temperature regions have been reported [67-71]. Table 4.1 reviews the experimental measurements and mechanism modeling for *n*-decane. Some relevant experimental data and modeling behaviors will be discussed in the later section.

Table 4.1 Review of experiments and modeling for *n*-decane

Authors	Devices	Conditions			Modeling
		T [K]	p [atm]	Mixtures	
Pfahl et al. [47]	ST (heated)	700-1300	13-50	$\phi = 0.5-2.0$ in air	--
Dean et al. [48]	ST (heated)	1000-1700	8.5	$\phi = 1.0$ in air	--
Zhukov et al. [49]	ST (heated)	800-1300	10-80	$\phi = 0.5, 1.0$ in air	--
Shen et al. [50]	ST (heated)	786-1396	9-58	$\phi = 0.25-1.0$ in air	--
Olchanski et al. [51]	ST (heated)	1239-1616	2-10	0.49-1.5% <i>n</i> -decane, 4.2-23.3% O ₂ in Ar	69 species; 433 reactions
Horning et al. [52]	ST	1400-1550	1	0.2% <i>n</i> -decane, 3.1% O ₂ in Ar	--
Haylett et al. [53]	ST (aerosol)	1100-1200	5	<i>n</i> -decane/O ₂ in Ar	--

(Table continues on next page)

Table 4.1 (continued)

Authors	Devices	Conditions			Modeling
		T [K]	p [atm]	Mixtures	
Wagner and Dugger [54]	FS	300	1	$\phi = 1.05$ in air	--
Zhao et al. [55]	FS	500	1	$\phi = 0.6-1.4$ in air	86 species; 641 reactions
Kumar and Sung [56]	FS	360, 400, 470	1	$\phi = 0.7-1.4$ in "O ₂ /N ₂ =1:3.76"	--
Wang et al. [57]	FS	403	1	$\phi = 0.7-1.5$ in air	--
Ji et al. [58]	FS	403	1	$\phi = 0.7-1.5$ in air	--
Bales-Gueret et al. [59]	JSR	925-1033	1	$\phi = 0.2-1.5$ in air	--
Dagaut et al. [45]	JSR	550-1150	10	$\phi = 1.0$ in air	--
Dagaut et al. [60]	JSR	700-1200	10-40	$\phi = 0.5, 1.0, 1.5$ in air	209 species; 1673 reactions
Biet et al. [61]	JSR	700-1200	1	$\phi = 1.0$ in He	--
Zeppieri et al. [62]	PFR	1019, 1033	1	$\phi \approx 1.0$	69 species; 494 reactions
Jahangirian et al. [63]	PFR	520-830	8, 12.5	$\phi = 1.0$ in N ₂	--
Delfau et al. [64]	Premixed flame	--	0.06	$\phi = 1.9$ in Ar	78 species; 638 reactions
Doute et al. [65]	Premixed flame	473	1	3.2% <i>n</i> -decane, 28.6% O ₂ in N ₂	62 species; 467 reactions
Kumar et al. [72]	RCM	635-706	7-30	<i>n</i> -decane/O ₂ in N ₂	--
Modeling including high-temperature mechanism alone					
Glaude et al. [66]	Turbulent PFR of <i>n</i> -octane [73]; JSR [59]				1216 species; 7920 reactions
Models including both high- and low-temperature pathways					
Ranzi et al. [67]	Lumped C ₁₀ -C ₁₄ <i>n</i> -alkane mechanism				250 species; 5000 reactions
Battin-Leclerc [68]	JSR [45, 59]; flame structure [64]				1216 species; 7920 reactions
Bikas and Peters [69]	Ignition delay times [47]; JSR [45]; Flame [65]				67 species; 600 reactions
Moréac et al. [70]	Ignition delay times [47]				506 species; 3684 reactions
Westbrook et al. [71]	C8 - C16 <i>n</i> -alkane mechanism				2116 species; 8130 reactions

Among the available *n*-decane models, there is no *n*-decane model with comprehensive validation applied for different reactors and a compact size suitable for complicated engine simulations. Such a compact and comprehensive *n*-decane model is being developed in current study.

The oxidation model for *n*-decane follows the rules for 25 reaction classes suggested by Curran et al. [74]. The reaction rates are mainly based on the previous *n*-heptane study by

Ahmed et al. [31]. With the help of recent experimental investigations and mechanism modeling, several updated reaction rates have been obtained as explained in the following.

First, the H atom abstraction reaction rate by hydroxyl radicals (OH) is applied from recent kinetic data of Sivaramakrishnan and Michael [75]. Using their data improves model predictions in the low temperature range compared to those reported in earlier studies [76, 77]. The H atom abstraction reactions by highly oxygenated methane derivatives (O₂CHO), as suggested by Curran and colleagues [74], are not considered. Instead, the rate coefficients for secondary oxygen addition (class 22) are multiplied with four to compensate for the reactivity in the low-temperature region (550-650 K). The reaction rates of abstraction reactions by radical carriers (other than OH) remain the same as given by Ahmed et al. [31].

Second, the revised kinetic data for β -scission reactions (reaction class 3) follow the study of El Bakali et al. [78], who suggested rates from theoretical predictions [79, 80].

Third, the high-temperature oxidation pathway of olefins is applied with detailed rules suggested by Nawdiyal et al. [32] because olefins are one of the most intermediate products. The low-temperature oxidation pathway of olefins is not included here because the low-temperature pathway is applied only to the seed molecule as explained in this chapter later. The H atom abstraction from olefins (reaction class 6) follows the rules of H abstraction from the fuel molecule (reaction class 2). As the allylic C-H bond and C-C bond have the lowest bond energies, only the rate coefficients on the allylic position given by Mehl et al. [81] are applied as the fastest reaction pathway. Subsequently, the detailed decomposition rules of olefin at the allylic position (reaction class 9) and the decomposition of alkenyl radicals (reaction class 8) are used as in Mehl et al. [81].

The primary mechanism for the oxidation of *n*-decane is shown in Table 4.2. With CGR applied, the resulting skeleton model consists of 65 species and 480 reactions. The thermodynamic and transport data of the species were taken from the literature [71].

Table 4.2: Primary mechanism for *n*-decane oxidation

Reaction	$A [\frac{cm^3}{mol \cdot s}]$	n	$E_a [\frac{cal}{mol}]$	Ref.
<i>Class 1 : Unimolecular alkane decomposition</i>				
$C_n H_{2n+2} = H + C_n H_{2n+1}$	2.5E27	-3.8	9.708E4	[31]
$C_{n+m} H_{2(n+m)+2} = C_n H_{2n+1} + C_m H_{2m+1}$	5.0E16	0.0	8.011E4	[78]

(Table continues on next page)

Table 4.2 (continued)

Reaction	$A [\frac{cm^3}{mol \cdot s}]$	n	$E_a [\frac{cal}{mol}]$	Ref.
<i>Class 2 : H atom abstraction from fuel & class 6 : H atom abstraction from alkenes</i>	Per <i>H</i>			
$C_nH_{2n+2} + H = C_nH_{2n+1} + H_2$				
Primary	5.63E07	2.00	7.706E3	[31]
Secondary	2.45E07	2.00	5.002E3	[31]
$C_nH_{2n+2} + OH = C_nH_{2n+1} + H_2O$				
Primary	4.55E06	1.81	8.683E2	[75]
Secondary S01 ^a	3.53E09	0.94	5.047E2	[75]
Secondary S11 ^a	2.86E06	1.81	-1.015E3	[75]
Secondary S11' ^a	2.81E11	0.32	8.465E2	[75]
$C_nH_{2n+2} + O = C_nH_{2n+1} + OH$				
Primary	3.66E05	2.40	5.507E3	[31]
Secondary	1.18E05	2.50	2.201E3	[31]
$C_nH_{2n+2} + CH_3 = C_nH_{2n+1} + CH_4$				
Primary	2.17E11	0.00	1.166E4	[31]
Secondary	2.00E11	0.00	9.506E3	[31]
$C_nH_{2n+2} + HO_2 = C_nH_{2n+1} + H_2O_2$				
Primary	2.68E12	0.00	1.941E4	[31]
Secondary	2.44E12	0.00	1.701E4	[31]
$C_nH_{2n+2} + CH_3O = C_nH_{2n+1} + CH_3OH$				
Primary	5.27E10	0.00	7.005E3	[31]
Secondary	5.48E11	0.00	5.002E3	[31]
$C_nH_{2n+2} + O_2 = C_nH_{2n+1} + HO_2$				
Primary	4.17E12	0.00	4.903E4	[31]
Secondary	1.00E13	0.00	4.763E4	[31]
$C_nH_{2n+2} + C_2H_3 = C_nH_{2n+1} + C_2H_4$				
Primary	1.67E11	0.00	1.801E4	[31]
Secondary	2.00E11	0.00	1.681E4	[31]
$C_nH_{2n+2} + C_2H_5 = C_nH_{2n+1} + C_2H_6$				
Primary	1.67E10	0.00	1.341E4	[31]
Secondary	2.50E10	0.00	1.041E4	[31]
$C_nH_{2n+2} + CH_3O_2 = C_nH_{2n+1} + CH_3O_2H$				
Primary	2.02E12	0.00	2.044E4	[31]
Secondary	2.02E12	0.00	1.771E4	[31]
$C_nH_{2n+2} + C_nH_{2n+1}O_2 = C_nH_{2n+1} + C_nH_{2n+1}O_2H$				
Primary	2.02E12	0.00	2.044E4	[31]
Secondary	2.02E12	0.00	1.771E4	[31]
<i>Reaction class 3: $C_nH_{2n} + H = C_nH_{2n+1}$</i>				
<i>H addition on terminal C</i>	1.00E13	0.0	1.200E3	[31]
<i>H addition on internal C</i>	1.00E13	0.0	2.900E3	[31]
$C_{n+m}H_{2(m+n)+1} = C_nH_{2n+1} + C_mH_{2m}$	2.50E13	0.0	2.880E4	[79]
<i>Reaction class 5: $C_nH_{2n} = C_nH_{2n}$</i>				
Primary to secondary 3 ring	5.48E08	1.62	3.876E4	[31]
Reverse	1.74E07	2.01	4.128E4	[31]
Primary to secondary 4 ring	1.39E09	0.98	3.376E4	[31]
Reverse	4.41E07	1.38	3.628E4	[31]
Primary to secondary 5 ring	2.54E09	0.35	1.976E4	[31] ^b
Reverse	1.61E08	0.74	2.228E4	[31] ^b
Primary to secondary 6 ring	4.28E11	-1.05	1.176E4	[31]
Reverse	1.36E10	-0.66	1.428E4	[31]
Secondary to secondary 3 ring (2-3)	9.59E08	1.39	3.970E4	[31]
Reverse	9.59E08	1.39	3.970E4	[31]

(Table continues on next page)

Table 4.2 (continued)

Reaction	$A [\frac{cm^3}{mol \cdot s}]$	n	$E_a [\frac{cal}{mol}]$	Ref.
Secondary to secondary 3 ring (3-4)	6.04E08	1.39	3.970E4	[31]
Reverse	1.20E09	1.39	3.970E4	[31]
Secondary to secondary 4 ring	1.76E09	0.76	3.470E4	[31]
Reverse	3.50E09	0.76	3.470E4	[31]
Secondary to secondary 5 ring	3.22E09	0.13	2.070E4	[31]
Reverse	3.22E09	0.13	2.070E4	[31]
Secondary to secondary 6 ring	5.00E11	-1.25	1.276E4	[71]
Reverse	1.60E10	-0.86	1.528E4	[71]
Reaction class 7				
$C_nH_{2n} + O \Rightarrow products$	2.00E10	0.00	-1.05E3	[31]
$C_nH_{2n} + OH \Rightarrow products$	2.00E10	0.00	-4.00E3	[31]
Reaction class 8				
secondary radicals (to form primary radical)	1.00E14	0.00	3.100E4	[81]
primary radicals (to form primary radical)	1.00E14	0.00	3.000E4	[81]
allyl radicals (to form primary radical)	1.00E13	0.00	3.500E4	[81]
secondary radicals (to form allyl radical)	3.16E13	0.00	2.600E4	[81]
Reaction class 9				
$C_nH_{2n} = C_{n-1}H_{2n-1} + CH_3$	2.50E16	0.00	7.300E4	[81] ^c
$C_{n+m}H_{2(n+m)} = C_nH_{2n-1} + C_mH_{2m+1}$	2.50E16	0.00	7.100E4	[81] ^c
Reaction class 10				
$C_nH_{2n+1} + O_2 = C_nH_{2n+1}O_2$	2.00E12	0.00	0	[31]
Reaction class 11				
$C_nH_{2n+1} + C_mH_{2m+1}O_2 = C_nH_{2n+1}O + C_mH_{2m+1}O$	7.00E12	0.00	-1.000E3	[31]
Reaction class 12				
$C_nH_{2n+1}O_2 = C_nH_{2n}O_2H$	Per H			
5 ring primary	2.98E12	0.00	2.970E4	[31]
5 ring secondary	2.98E12	0.00	2.790E4	[31]
6 ring primary	2.47E11	0.00	2.390E4	[31]
6 ring secondary	2.48E11	0.00	2.215E4	[31]
7 ring primary	2.06E10	0.00	2.110E4	[31]
7 ring secondary	2.06E10	0.00	1.935E4	[31]
8 ring primary	1.72E09	0.00	2.390E04	[31]
8 ring secondary	1.72E09	0.00	2.215E04	[31]
Reaction class 13,14				
$C_nH_{2n+1}O_2 + HO_2 = C_nH_{2n+1}O_2H + O_2$	1.75E10	0.00	-3.275E3	[31]
$C_nH_{2n+1}O_2 + H_2O_2 = C_nH_{2n+1}O_2H + HO_2$				
forward reaction	2.40E12	0.00	1.000E4	[31] ^b
reverse reaction	2.40E12	0.00	1.000E4	[31] ^b
Reaction class 15, 16				
$C_nH_{2n+1}O_2 + CH_3O_2 \Rightarrow C_nH_{2n+1}O + CH_3O + O_2$	1.40E16	-1.61	1.860E3	[31]
$C_nH_{2n+1}O_2 + C_mH_{2m+1}O_2 \Rightarrow C_nH_{2n+1}O + C_mH_{2m+1}O + O_2$	1.40E16	-1.61	1.860E3	[31]
Reaction class 17				
$C_nH_{2n+1}O_2H = C_nH_{2n+1}O + OH$	1.26E16	0.00	4.250E4	[31]
Reaction class 18				
product1 + product2 + product3 = $C_nH_{2n+1}O$	1.00E11	0.00	1.190E4	[31]
Reaction class 19				
cyclic ether 3 ring	3.00E11	0.00	2.200E4	[31]
cyclic ether 4 ring	2.50E10	0.00	1.525E4	[31]
cyclic ether 5 ring	2.08E09	0.00	6.500E3	[31] ^b
cyclic ether 6 ring	1.50E08	0.00	1.800E3	[31] ^b

(Table continues on next page)

Table 4.2 (continued)

Reaction	$A [\frac{cm^3}{mol \cdot s}]$	n	$E_a [\frac{cal}{mol}]$	Ref.
<i>Reaction class 20</i>				
$C_nH_{2n} + HO_2 = C_nH_{2n}OOH$ addition on terminal position	1.00E11	0.00	1.250E4	[31]
addition on internal position	1.00E11	0.00	7.600E3	[31]
<i>Reaction class 21</i>				
$C_nH_{2n}OOH \Rightarrow C_nH_{2m} + carbonyl + OH$	5.00E13	0.00	2.550E4	[31]
<i>Reaction class 22</i>				
$C_nH_{2n}OOH + O_2 = O_2C_nH_{2n}OOH$	8.00E12	0.00	0	[31] ^d
<i>Reaction class 23</i>				
$O_2C_nH_{2n}OOH = OC_nH_{2n}O_2 + OH$	Per H			
5 ring primary	1.49E12	0.00	2.670E4	[31]
5 ring secondary	1.49E12	0.00	2.490E4	[31]
6 ring primary	1.24E11	0.00	2.090E4	[31]
6 ring secondary	1.24E11	0.00	1.915E4	[31]
7 ring primary	1.03E10	0.00	1.810E4	[31]
7 ring secondary	1.03E10	0.00	1.635E4	[31]
8 ring primary	8.60E08	0.00	2.090E4	[31]
8 ring secondary	8.60E08	0.00	1.915E4	[31]
<i>Reaction class 24</i>				
$OC_nH_{2n}O_2 = product + OH$	1.00E16	0.00	4.30E4	[31]
<i>Reaction class 25</i>				
$C_nH_{2n}O + OH = products + H_2O$				
H - C - O primary	9.50E07	1.61	-3.500E1	[31]
H - C - O secondary	8.84E09	1.00	-1.490E2	[31]
$C_nH_{2n}O + HO_2 = products + H_2O_2$				
H - C - O primary	3.00E04	2.60	1.390E4	[31]
H - C - O secondary	1.08E04	2.55	1.053E4	[31] ^b

The rate constant, $k = A * T^n * \exp(-E_a/RT)$ are given in the units of s^{-1} , cm^3 , mol^{-1} , cal .

^a The rate constant here are taken from the source of rate constants [75].

^b The rate constant here is taken from the corrected table in the literature [31].

^c The pre-exponential factor here is multiplied with 2.5 for the value from Mehl et al. [81].

^d The pre-exponential factor here is multiplied with 2 for the value from [81].

4.2 Mechanism development for AMN

AMN is a simple polycyclic aromatic hydrocarbon (PAH) and is used as a cetane-number reference compound. PAHs are present in heating oil, diesel fuels, and aviation fuels. They are known to contribute significantly to the soot formation chemistry of these fuels. Furthermore, aromatic components are well-known knock inhibitors and are used as additives to supply high-octane unleaded gasoline [82]. Three reaction mechanisms of AMN oxidation [82-85] have been developed in the past. AMN combustion was studied in several experiments including the determination of ignition delay times [47, 86] and speciation in JSR [85, 87] and plug flow reactors [83, 84]. Table 4.3 reviews the experimental measurements and mechanism modeling of AMN.

Table 4.3: Review of experiments and modeling for AMN

Mechanism modeling of AMN				
Mechanism	Size	Validations and analyses included		
Shaddix et al. [83, 84]	unknown	AMN/air in PFR at 1 atm, 1200 K and $\phi = 0.7-1.3$ in their paper study and reaction pathway analysis		
Pitsch et al. [82]	89 species, 393 reactions	AMN/air in PFR at 1 atm, 1200 K and $\phi = 0.6$ [83]; Ignition delay of AMN/air mixtures by Pfahl et al. [47]		
Mati et al. [85]	146 species, 1041 reactions	AMN/O ₂ /N ₂ in JSR at 10 bar, 800-1150 K, $\phi = 0.5-1.5$ in their study; ignition delay of AMN/air [47]		
Experimental studies of AMN				
Authors	Devices	Conditions		
		T [K]	p [atm]	Mixtures
Shaddix et al. [83, 84]	PFR	1200	1	$\phi = 0.6-1.5$
Dagaut et al. [85]	JSR	800-1450	1-10	$\phi = 0.5, 1.0, 1.5$ in air
Pfahl et al. [47]	ST (heated)	700-1300	13-50 bar	$\phi = 0.5-2.0$ in air
Wang et al. [86]	ST (heated)	1032–1500	8-45 bar	$\phi = 0.5, 1.0, 1.5$ in air

Since a detailed kinetic model of AMN is of meaningful importance, a comprehensive AMN model is developed in current study. The reaction coefficients of the AMN model will be carefully investigated and discussed in the following.

There are few measured reaction rates for AMN and neither the analog of cresols nor that of dibenzyl has been measured in consistent or significant quantities. The reaction rates in current study mainly follow the kinetic model of AMN combustion [85] and toluene combustion [88, 89]. The mechanism for the oxidation of AMN is summarized in Table 4.4.

Table 4.4: Primary mechanism for AMN oxidation

No	Reactions of AMN	A	n	E _a	References	
Initiation reactions						
1	$A_2CH_3 + O_2 = A_2CH_2 + HO_2$	2.18E+07	2.50	46000	[90]	
2	$A_{2-x} + CH_3 (+ M) = A_2CH_3 (+ M)$	k_∞	2.33E+14	-0.283	-191	[91]
		k_0	1.08E+79	-20.22	14980	
		F_{cent}	0.5	15000	6.6E-6	
3	$A_2CH_2 + H = A_2CH_3$	1.00E+14	0.00	0	[85, 92]	
4	$A_2CH_3-p + H = A_2CH_3$	1.00E+14	0.00	0	[89]	
H atom abstraction reactions						
5	$A_2CH_3 + H = A_2CH_2 + H_2$	3.98E+02	3.40	3120	[85, 92]	
6	$A_2CH_3 + OH = A_2CH_2 + H_2O$	1.27E+13	0.00	2583	[85, 92]	
7	$A_2CH_3 + O = A_2CH_2 + OH$	5.00E+08	1.50	8000	[85, 92]	
8	$A_2CH_3 + CH_3 = A_2CH_2 + CH_4$	1.58E+12	0.00	11099	[85, 93]	
9	$A_2CH_3 + HO_2 = A_2CH_2 + H_2O_2$	4.00E+11	0.00	14077	[85, 94]	

(Table continues on next page)

Table 4.4 (continued)

No	Reactions of AMN	A	n	E _a	References
H atom abstraction reactions					
10	$A_2CH_3 + A_{2-x} = A_2CH_2 + A_2$	2.10E+12	0.00	4400	[88, 95]
11	$A_2CH_3 + A_2CH_3-p = A_2CH_2 + A_2CH_3$	7.90E+13	0.00	12000	[89]
12	$A_2CH_3 + H = A_2CH_3-p + H_2$	6.00E+08	1.00	16800	[89]
13	$A_2CH_3 + OH = A_2CH_3-p + H_2O$	1.60E+08	1.42	1450	[89]
14	$A_2CH_3 + O = A_2CH_3-p + OH$	2.00E+13	0.00	14700	[89]
15	$A_2CH_3 + CH_3 = A_2CH_3-p + CH_4$	2.00E+12	0.00	15000	[89]
16	$A_2CH_3 + HO_2 = A_2CH_3-p + H_2O_2$	4.00E+11	0.00	28900	[89]
Radical addition reactions					
17	$A_2CH_3 + H = A_2 + CH_3$	1.20E+13	0.00	5148	[88, 96]
18	$A_2CH_3 + O = OA_2CH_3 + H$	1.63E+13	0.00	3418	[88, 97]
Reactions of phenylbenzyl radicals (A_2CH_2)					
19	$A_2CH_2 + HO_2 \Rightarrow A_2CHO + OH + H$	7.60E+12	0.00	0	[98] ^a
20	$A_2CH_2 + HO_2 \Rightarrow A_{2-x} + CH_2O + OH$	2.40E+12	0.00	0	[98] ^a
21	$A_2CH_2 + O = A_2CHO + H$	1.65E+14	0.00	0	[88]
22	$A_2CH_2 + O = CH_2O + A_{2-x}$	8.00E+13	0.00	0	[88]
Reactions of methylnaphtyl radicals (A_2CH_3-p) and derived radicals					
23	$A_2CH_3-p + HO_2 = OA_2CH_3 + OH$	5.00E+12	0.00	0	[89]
24	$A_2CH_3-p + O = OA_2CH_3$	1.00E+14	0.00	0	[89]
25	$A_2CH_3-p + O_2 = OA_2CH_3 + O$	2.60E+13	0.00	6100	[89]
26	$A_2CH_3-p + H = A_2CH_2 + H$	1.00E+13	0.00	0	[89, 99]
27	$OA_2CH_3 \Rightarrow A_1C_2H_2-r1 + C_2H_2 + CO$	5.40E+11	0.00	43900	[89, 100]
28	$OA_2CH_3 \Rightarrow C_4H_2 + 3C_2H_2 + H + CO$	2.20E+11	0.00	43900	[89, 100]
Reactions of naphtyl (A_{2-x}) and derived radicals					
29	$A_{2-x} + HO_2 = OA_2 + OH$	5.00E+13	0.00	999	[85, 101]
30	$A_{2-x} + O = OA_2$	1.00E+14	0.00	0	[102]
31	$A_{2-x} + O_2 = OA_2 + O$	2.60E+13	0.00	6100	[89]
32	$OA_2 = A_1R_5- + CO$	7.40E+11	0.00	43900	[100]
33	$OA_2 + H = A_1R_5 + CO$	8.00E+12	0.00	0	[88]
Reactions of 1-naphthaldehyde (A_2CHO) and derived radicals					
34	$A_2CHO + O_2 = A_2CO + HO_2$	1.02E+13	0.00	38950	[88]
35	$A_2CHO + H = A_2CO + H_2$	5.00E+13	0.00	4928	[88]
36	$A_2CHO + OH = A_2CO + H_2O$	1.71E+09	0.00	-447	[88]
37	$A_2CHO + O = A_2CO + OH$	9.04E+12	0.00	3080	[88]
38	$A_2CHO + CH_3 = A_2CO + CH_4$	2.77E-03	2.81	5773	[88]
39	$A_2CHO + HO_2 = A_2CO + H_2O_2$	3.01E+12	0.00	13074	[88]
40	$A_2CHO + A_{2-x} = A_2CO + A_2$	7.01E+11	0.00	4400	[88]
41	$A_2CHO + A_2CH_2 = A_2CO + A_2CH_3$	2.77E+03	2.81	5773	[88]
42	$A_2CHO = A_2CO + H$	3.98E+15	0.00	83699	[85, 103]
43	$A_2CHO + H = A_2 + HCO$	1.20E+13	0.00	5148	[88]
44	$A_2CO = A_{2-x} + CO$	3.98E+14	0.00	29398	[88]
Reactions of indene (A_1R_5) and derived radicals					
45	$A_1R_5 + O_2 = A_1R_5- + HO_2$	2.00E+13	0.00	25000	[85, 88]
46	$A_1R_5 + H = A_1R_5- + H_2$	2.19E+08	1.77	3000	[88]
47	$A_1R_5 + OH = A_1R_5- + H_2O$	3.43E+09	1.18	-447	[85, 88]
48	$A_1R_5 + O = A_1R_5- + OH$	1.80E+13	0.00	3080	[85, 88]

(Table continues on next page)

Table 4.4 (continued)

No	Reactions of AMN	A	n	E _a	References
Reactions of indene (A ₁ R ₅) and derived radicals					
49	A ₁ R ₅ + HO ₂ = A ₁ R ₅ - + H ₂ O ₂	1.99E+12	0.00	11659	[82, 85]
50	A ₁ R ₅ + O ₂ = OA ₁ R ₅ + OH	1.00E+13	0.00	20712	[85]
51	A ₁ R ₅ - + H = A ₁ R ₅	1.00E+14	0.00	0.00	[85, 88]
52	A ₁ R ₅ - + O = n-A ₁ C ₂ H ₂ + CO	1.00E+14	0.00	0.00	[85, 88]
53	A ₁ R ₅ - + O = OA ₁ R ₅	1.00E+13	0.00	0.00	[85]
54	OA ₁ R ₅ = A ₁ C ₂ H ₂ -r1 + CO	7.40E+11	0.00	43900	[85, 88, 100]
Reactions of naphthalene (A ₂)					
55	A ₂ + O ₂ = A ₂ -x + HO ₂	6.30E+13	0.00	60000	[85, 104]
56	A ₂ + O = A ₂ -x + OH	2.00E+13	0.00	14704	[85]
57	A ₂ + O = OA ₂ + H	2.23E+13	0.00	4530	[82, 85]
58	C ₂ H ₂ + A ₁ C ₂ H-o = A ₁ C ₂ HAC	1.00E+13	0.00	0	[19]
59	A ₁ C ₂ HAC = A ₂ -x	1.00E+10	0.00	0	[19]
60	O ₂ + A ₁ C ₂ HAC => 2HCO + A ₁ C ₂ H-o	1.00E+13	0.00	0	[19]
61	H + A ₂ -x = A ₂	1.00E+13	0.00	0	[19]
62	H + A ₂ = H ₂ + A ₂ -x	1.00E+14	0.00	0	[19]
63	OH + A ₂ = H ₂ O + A ₂ -x	2.10E+13	0.00	19	[19]
64	C ₂ H + A ₂ = C ₂ H ₂ + A ₂ -x	2.00E+13	0.00	0	[19]

The rate constant, $k = A * T^n * \exp(-E_a/RT)$ are given in the units of $s^{-1}, cm^3, mol^{-1}, cal$.

^a The pre-exponential factor here is multiplied with 2 for the value from [98].

The initiation reactions include H atom abstraction by O₂ molecules (1). The rate coefficients of abstraction reactions by O₂ are applied using the values proposed by Oehlschlaeger et al. [90]. The rate determinations by Oehlschlaeger et al. [90] are in fair agreement with the previous measurements of Eng et al. [105] but with much less scatter and uncertainty. The three-parameter rate expression is the result of the combination of the current data with the measurements made by Ingham et al. [106] and is in good agreement with the review recommendations of Baulch et al. [107].

The unimolecular decomposition considers the removal of the CH₃ group and the removal of the H atom at the α -position is favored (2-3). The rate coefficients for unimolecular decomposition are applied with the reaction rates of Klippenstein et al. [91]. Besides, unimolecular decomposition also considers H atom abstraction from the ring side (4) and its rate coefficient is taken from the study of Bounaceur et al. [89].

The H atom abstraction reaction from the methyl group forms A₂CH₂ radicals, while the ring H abstraction at the para-site forms A₂CH₃-p radicals. The H abstraction reactions (5-11) are considered with H, OH, O, CH₃, HO₂, A₂-x, and A₂CH₃-p radicals.

The reactions of multi-ring species are, in principle, similar to those of comparable one-ring toluene species. The author uses the ring H atom abstraction reactions (12-16) and the rate coefficients provided by Bounaceur et al. [89]. All of these reactions (12-16) were not considered by Mati et al. [85].

The radical addition reactions are important for aromatic compounds. The addition reactions (17-18) include H and O radicals. The rate coefficients follow values from the literature [96, 97].

The A_2 -x, A_2CH_2 , and A_2CH_3 -p radicals are important intermediates after the first chemical step of AMN, and their consecutive reactions dominate the further degradation.

The decomposition reactions of A_2CH_2 mainly occur via two pathways: one pathway with $A_2CH_2 + HO_2$ and one pathway with $A_2CH_2 + O$, of which the pathway with $A_2CH_2 + HO_2$ is dominant. The reaction rates are applied using the values proposed by Hippler et al. [98]. Ranzi et al. [67] also followed these reaction rates for the oxidation of toluene. This pathway will be discussed in detail in the next section.

The decomposition reactions of the A_2CH_3 -p and A_2 -x radicals are expressed in three types of reactions:

- I) A_2CH_3 -p + $O_2 = OA_2CH_3 + O$ / A_2 -x + $O_2 = OA_2 + O$
- II) termination reactions by O and HO_2 radicals
- III) decomposition of OA_2CH_3 / decomposition of OA_2

Besides, the decomposition of OA_2CH_3 is proven to be an important pathway as shown in the flow analysis. The rate coefficients are used in the same way as the decomposition of phenoxy radicals to produce carbon monoxide and cyclopentadienyl radicals, as proposed by [100].

The further decomposition reactions of other products (A_2CHO , A_1R_5 and A_2) can be found in Table 4.4. The thermodynamic data of the species are mainly taken from Burcats' Thermodynamic Database [108]. Species not available in this database are calculated with Benson's group additivity method [109]. Because of the compact size, there is no need of a reduction procedure. The AMN oxidation consists of 20 species and 92 reactions.

4.3 Compilation of AMN/*n*-decane

There have been several studies on the AMN/*n*-decane blend. The oxidation of the IDEA blend was compared with that of a commercial diesel fuel in a JSR under identical ini-

tial conditions (560-1030 K, 6 and 10 atm, equivalence ratios of 0.25-1.5 and 10300 ppm of carbon) [110]. Current study demonstrated the general suitability of the IDEA blend as a diesel surrogate fuel. Their kinetic modeling of the experiments showed the importance and high sensitivity of the production and consumption of OH radicals.

Wang et al. [86] investigated the ignition delay times of 30% AMN/70% *n*-decane, 70% AMN/ 30% *n*-decane (in mole fractions), and pure AMN at 848-1394 K and 10-50 bar.

The auto-ignition of suspended liquid AMN/*n*-decane droplets was studied by Moriue et al. [111]. The authors reported raised induction times with increased aromatic content. The chain-breaking effect of AMN reduces the reactivity of *n*-decane in the gas phase.

Additionally, blends of AMN/*n*-decane have also been investigated for diesel and HCCI engine simulations [2]. A summary of published oxidation modeling approaches for the AMN/*n*-decane blend is shown in Table 4.5.

Table 4.5: Summary of published oxidation models for the AMN/*n*-decane blend

Mechanism	Size	Validations included
AMN/ <i>n</i> -decane blend (Wang et al. [86])	662 species, 3864 reactions	Ignition delay of AMN/ <i>n</i> -decane blend and AMN in their paper study; Ignition delay of <i>n</i> -decane by Pfahl et al. [47], Zhukov et al. [49], Shen et al.[50]; AMN/O ₂ /N ₂ in JSR at 10 bar, 800-1150 K, $\phi = 1$ [87] AMN/O ₂ /N ₂ in PFR at 1 atm, 1170 K, $\phi = 1$ [84]
AMN/ <i>n</i> -decane blend (Ramirez et al. [110])	1124 species, 4762 reactions	IDEA blend in JSR at 6 and 10 atm, 560-1030 K and $\phi = 0.25-1.5$ in their paper study
AMN/ <i>n</i> -decane blend (Bounaceur et al. [112])	530 species, 2834 reactions	AMN/ <i>n</i> -decane droplet in pressurized chamber at 3 bar by Moriue et al. [111] Ignition delay of AMN by Pfahl et al. [47] AMN/O ₂ /N ₂ in JSR at 10 bar, 800-1150 K, $\phi = 1$ [87] AMN/O ₂ /N ₂ in PFR at 1 atm, 1170 K, $\phi = 1$ [84]
AMN/ <i>n</i> -decane blend in current study	273 species, 3100 reactions	Ignition delay of AMN/ <i>n</i> -decane blend and AMN [86] IDEA blend in JSR at 10 atm, 560-1030 K [110] Ignition delay of <i>n</i> -decane by Pfahl et al. [47], Zhukov et al. [49], Shen et al. [50] AMN/air in JSR at 10 bar, $\phi = 1$ [85] <i>n</i> -Decane/air in JSR at 10 bar, $\phi = 1$ [45]

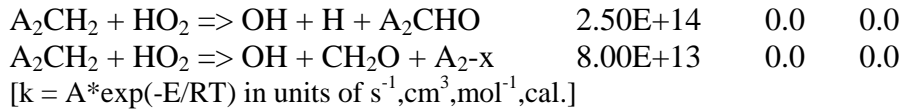
To date, the IDEA kinetic models published so far are either broadly validated but very large, which limits their application in engine simulations, or they are compact, but suitable only for engine simulations. In current study, compact and comprehensive oxidation models of *n*-decane and AMN, respectively, are developed and compiled. The feature of current AMN/*n*-decane blend is the complete validations with available experiments for the AMN/*n*-decane blend and pure AMN and *n*-decane as well. Besides, the IDEA blend model

in current study is compiled using a broadly validated base mechanism. Another aim of this dissertation is to discuss a decisive reaction pathway for the AMN model. It is observed in this work that the reaction pathway of $A_2CH_2 + HO_2$ is one important source of OH formation in the initial stage. In the case of the blends of AMN/*n*-decane, these OH radicals promote the decomposition of both AMN and *n*-decane fuel. Therefore, a discussion of a proper rate coefficient for the $A_2CH_2 + HO_2$ pathway makes sense, as shown in the next section.

4.4 Fuel-fuel interaction

Although direct fuel-fuel interaction reactions, such as AMN reacting with *n*-decyl radicals as described by Wang et al. [86], are not included in the current AMN/*n*-decane blend, the reaction pathways of $A_2CH_2 + HO_2$ provide fuel-fuel interaction via the HO_2 and OH radicals.

The majority of published AMN modeling mechanisms [82, 85, 86] include two paths for the reaction of $A_2CH_2 + HO_2$ with the rate coefficients from the publication of Emdee et al. [88] presented for toluene oxidation:



Emdee and his colleagues [88] stated that their rate coefficients were estimated and their sum was similar to that of $3.3E+14 \text{ cm}^3/\text{mol}$ for the reaction $A_1CH_2 + O_2$ reported by Bartels et al. [113]. However, there are no measurements or theories that support this high rate coefficient. When applying this high rate coefficient, the ignition delay times of AMN are accelerated. To compensate for the over-reactivity of the $A_2CH_2 + HO_2$ reaction, these AMN models [82, 85, 86] add the chain-breaking reaction: $OA_2 + H = OHA_2$ followed by chain breaking decomposition reactions: $OHA_2 + OH = OA_2 + H_2O$, $OHA_2 + H = OA_2 + H_2$, $OHA_2 + O = OA_2 + OH$, and $OHA_2 + H = A_2 + OH$.

The AMN model by Shaddix et al. [84] uses a rate coefficient of $2.0E+13 \text{ cm}^3/\text{mol}$. They consider the value used by Emdee et al. [88] to be too high. The rate coefficient of $2.0E+13 \text{ cm}^3/\text{mol}$ was determined by Colket et al. [114] and recommended by Tsang and Hampson [115] for analogous reactions with methyl radicals.

Hippler and his colleagues [98] proposed a rate coefficient of $5.0E+12 \text{ cm}^3/\text{mol}$ for the total $A_1CH_2 + HO_2$ reaction, obtained from a model fit. The toluene model by Ranzi et al.

uses values close to the reaction rate proposed by Hippler et al. [98]. Bounaceur et al. [89] applied the values taken from Hippler for the combination reaction of $A_1CH_2 + HO_2$.

The toluene model by Oehlschlaeger et al. refers to a rate coefficient of $3.6E+12$ cm^3/mol determined by Brezinsky et al. [116]. Another AMN model [117] did not consider these reactions to achieve better model agreement with their JSR experiment. The above-mentioned reaction rates are summarized in Table 4.6.

Table 4.6: Summary of studies related to the reaction pathway with $A_2CH_2 + HO_2$

Mechanism	Reaction rate and comments			
Oxidation of toluene (Emdee et al. 1992 [88])	$A_1CH_2 + HO_2 = OH + H + A_1CHO$	2.50E+14	0	0
	$A_1CH_2 + HO_2 = OH + CH_2O + A_1-$	8.00E+13	0	0 ^a
Mechanism models following Emdee' rate coefficient include the AMN/ <i>n</i> -decane blend (Wang et al. 2010 [86]), AMN/ <i>n</i> -decane (Ramirez et al. 2010 [110]), AMN (Mati et al. 2007 [85]), and AMN (Pitsch 1996 [82]).				
Oxidation of AMN (Shaddix et al. 1992 [83])	$A_2CH_2 + HO_2 = OH + products$	2.00E+13	0	0 ^b
Oxidation of acetaldehyde (Colket et al. 1977 [114])	$CH_3 + HO_2 = OH + CH_3O$ measurement in a turbulent flow reactor	2.00E+13	0	0 ^c
Oxidation of benzyl radicals (Hippler et al. 1991 [98])	$A_1CH_2 + HO_2 = OH + products$	5.00E+12	0	0 ^d
Current study	$A_2CH_2 + HO_2 => OH + H + A_2CHO$	7.60E+12	0	0
	$A_2CH_2 + HO_2 => OH + CH_2O + A_2-x$	2.40E+12	0	0 ^e
Oxidation of toluene (Ranzi et al. 2005 [67])	$A_1CH_2 + HO_2 = OH + H + A_1CHO$	5.00E+12	0	2E4
	$A_1CH_2 + HO_2 = OH + CH_2O + A_1-$	5.00E+12	0	0 ^f
Other AMN and toluene mechanism models				
Oxidation of AMN (Bounaceur et al. 2007 [112])	Did not consider these reactions to get better agreement with JSR validation			
Benzyl radical with hydroperoxyl radical (Brezinsky et al. [116])	$A_1CH_2 + HO_2 = OH + H + A_1CHO$ Calculated by thermochemical kinetics, collision theory, and RRK theory	3.60E+12	0	0

The rate constants, $k = A * T^n * \exp(-E_a/RT)$ are given in units of s^{-1} , cm^3 , mol^{-1} , cal.

^aThe total rate constant is equal to the value used by Bartels et al. [113].

^bThe rate constant is assigned 2.00E+13 as determined by Colket et al. [114].

^cThe rate constant is calculated from the measurement in the turbulent flow reactor in their study.

^dThe rate constant is assumed from the measurement of the shock tube in their study.

^eThe rate constant corresponds to the ratio of the two reactions taken from Emdee et al. [88], applied with twice the total rate constant of Hippler et al. [98] and equal to the value used by Ranzi et al. [67].

^fTheir citations are unknown and the values are close to the reaction rate reported by Hippler et al. [98].

According to the above literature review, the rate coefficients for $A_2CH_2 + HO_2$ by Hippler et al. [98], Brezinsky et al. [116], and Colket et al. [114] are relatively close to each other, while the rate coefficient by Emdee et al. [88] is nearly two orders of magnitude faster than the other values. Since there are no direct experiments or theories supporting the high rate coefficient reported by Emdee et al. [88] and the corresponding chain-breaking reaction and relative reaction, the author applied the value taken from Hippler et al. [98] in current

study. The reactions are kept only as forward reactions because their backward reactions with three products hardly occur in reality. The author kept two sets of products taken from Emdee et al. [88], applied with the sum of pre-exponential factors ($1.0\text{E}+13 \text{ cm}^3/\text{mol}$), twice as the pre-exponential factors by Hippler et al. [98]. The sum of the pre-exponential factors is equal to the sum of the pre-exponential factors for the reaction $\text{A}_1\text{CH}_2 + \text{HO}_2$ by Ranzi et al. [67] and is in the middle region of the values reported by Colket et al. [114] and Brezinsky et al. [116]. Following section shows the simulations performed in a constant volume and discusses the interaction between AMN and *n*-decane.

4.4.1 Blends of AMN and *n*-decane

Ignition delay times of pure AMN, 99% AMN/1% *n*-decane (99/1 blend) and 90% AMN/10% *n*-decane (90/10 blend) at 40 bar are plotted in the Figure 4.1. Either with 1% or 10% *n*-decane addition, the AMN/*n*-decane blend is more reactive than pure AMN. Meanwhile, the ignition delay times of 90/10 blend are faster than those of 99/1 blend, especially in NTC and low-temperature regions. To illustrate how does the addition of *n*-decane accelerate the reactivity of AMN in the NTC region, the simulations and reaction analyses of 90/10 blend and pure AMN are respectively calculated in a constant volume reactor at 40 bar and 900 K as shown in the Figures 4.2 - 4.5.

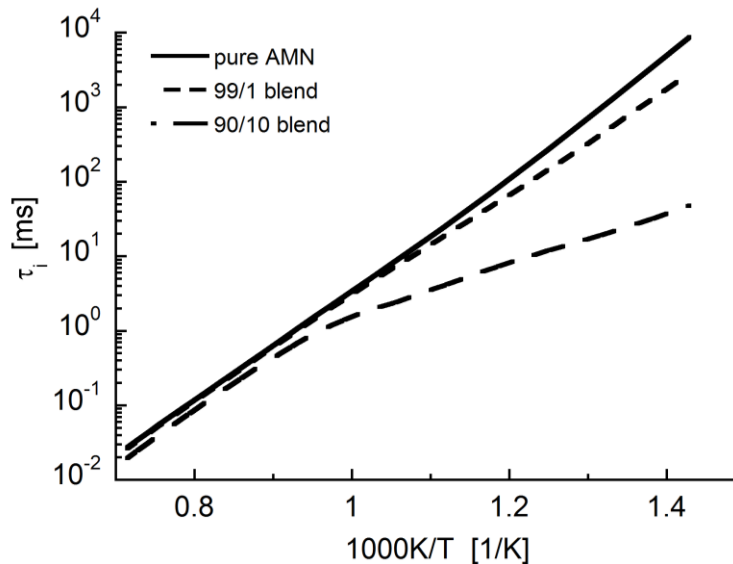


Figure 4.1: Ignition delay times of AMN, 99/1 and 90/10 blend in air at $p = 40 \text{ bar}$ and $\phi = 1$

pure AMN vs 90/10 blend

With addition of 10% *n*-decane, the concentration profiles of AMN, O₂ and *n*-decane are shown in the Figure 4.2 (left). It can be clearly noticed that *n*-decane has 2-stage decomposition. According to the theory, the 1st stage of *n*-decane decomposition results in the formation of relative stable species including H₂O₂, olefins (such as decene), aldehydes (such as *n*-C₃H₇CHO), etc. Some examples of stable species are shown in the Figure 4.2 (right). Till these stable species start to decompose, the auto-ignition begins.

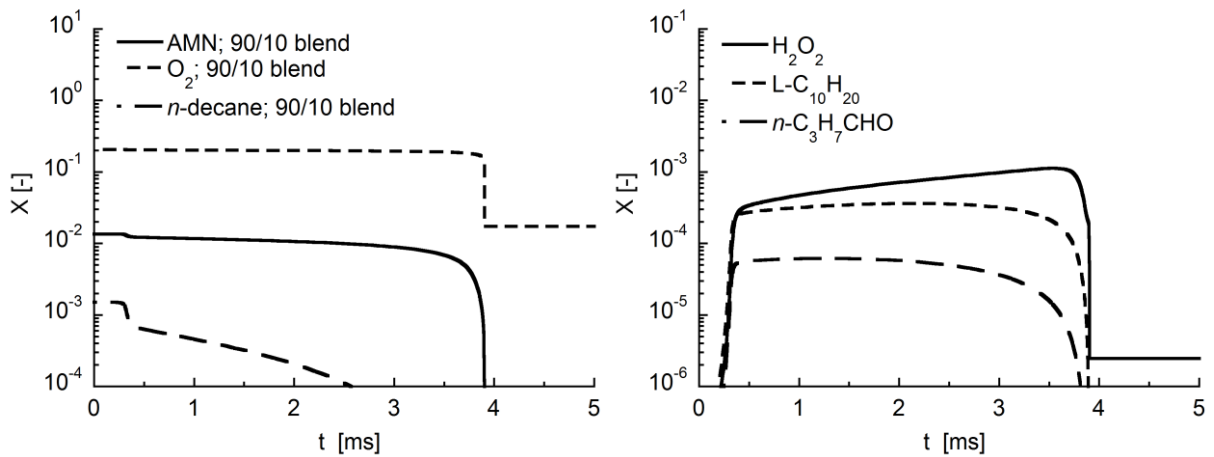


Figure 4.2: Speciation of 90/10 blend in air at $p = 40$ bar, $\phi = 1$ and $T = 900$ K

Since the AMN and *n*-decane share all reactive radicals, due to the formation of reactive radicals from *n*-decane, the decomposition of AMN shows 2-stage decomposition tendency. In this way, both fuels consumed with much faster reaction rates as shown in the Figure 4.3 (left). Figure 4.3 (right) is set with 5 ms for x Axis for better showing reaction rates of 90/10 blend. Same setting is performed from Figure 4.3 to Figure 4.5.

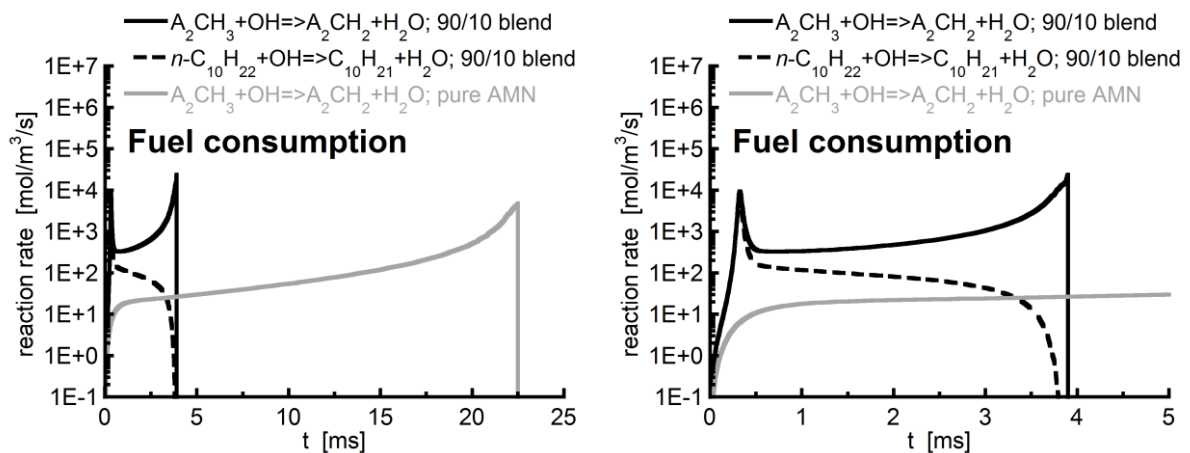


Figure 4.3: Net reaction rate of fuel decomposition for 90/10 blend and pure AMN in air at $p = 40$ bar, $\phi = 1$ and $T = 900$ K

Figure 4.4 shows the net reaction rate of major HO₂ formation. With addition of 10% *n*-decane, the decomposition reaction of 5-ring hydroperoxical radicals becomes a new HO₂ formation source. Another main HO₂ formation source: H + O₂ + M₁ => HO₂ + M₁ are accelerated with addition of 10% *n*-decane.

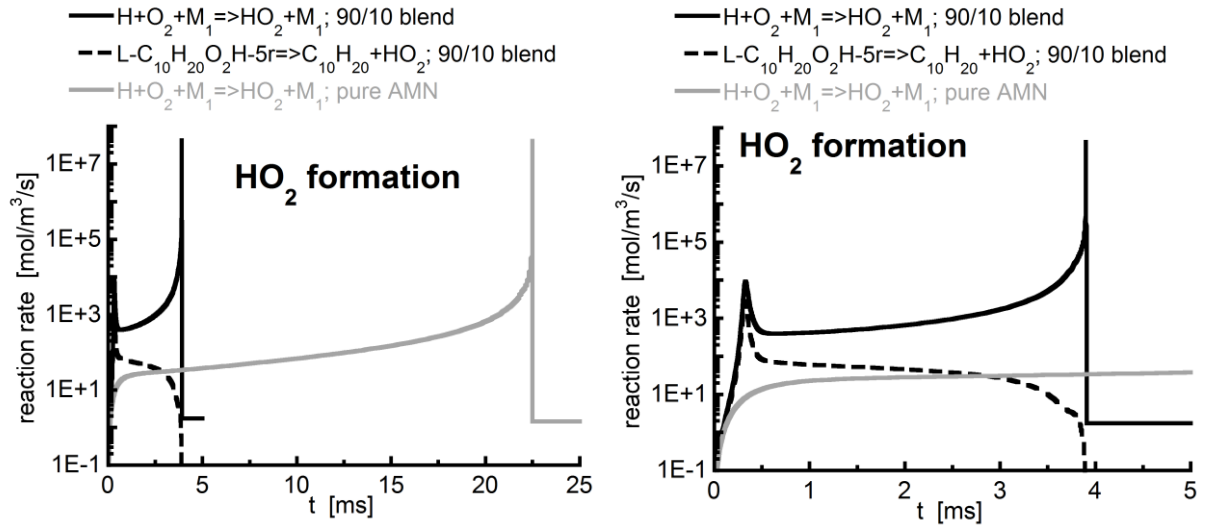


Figure 4.4: Net reaction rate of major HO₂ formation for 90/10 blend and pure AMN in air at $p = 40$ bar, $\phi = 1$ and $T = 900$ K

The faster HO₂ formation leads to the chain propagating pathway of A₂CH₂ + HO₂ as shown in the Figure 4.5. The chain propagating pathway of A₂CH₂ + HO₂ forms reactive OH and H radicals. These radicals result in the faster fuel decomposition and in turn the faster fuel decomposition provide more A₂CH₂ radicals for the reaction pathways of A₂CH₂ + HO₂ and initiate other subsequently reactions.

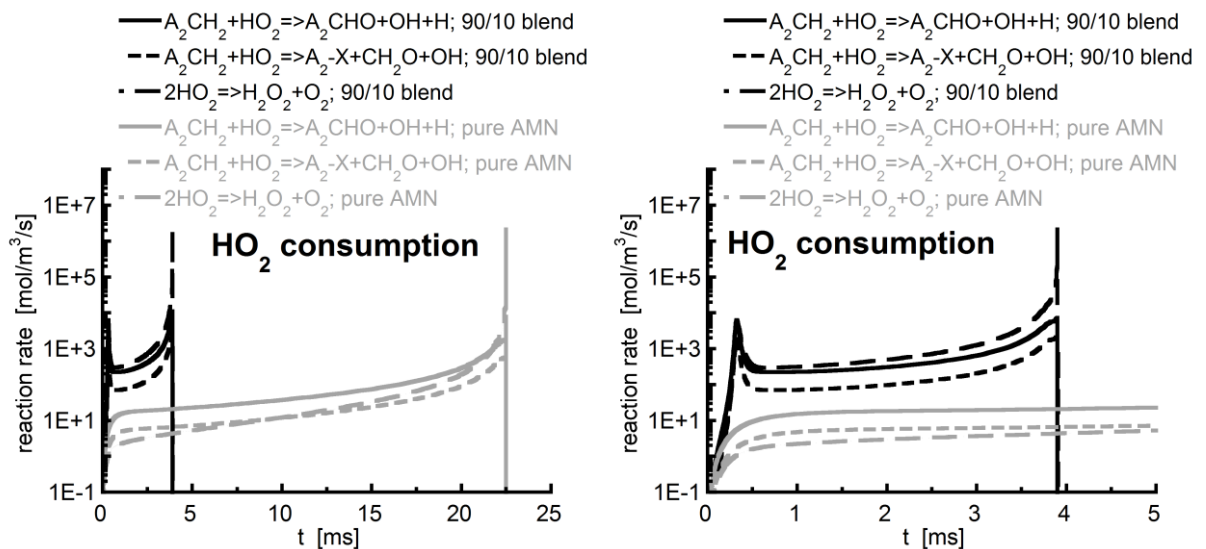


Figure 4.5: Net reaction rate of major HO₂ consumption for 90/10 blend and pure AMN in air at $p = 40$ bar, $\phi = 1$ and $T = 900$ K

pure *n*-decane vs 10/90 blend

The ignition delay times of *n*-decane and 10% AMN/90% *n*-decane (10/90 blend) in air at 40 bar and $\phi = 1$ are plotted in the Figure 4.6. From the Figure 4.1, the ignition delay times of AMN show high sensitivity with small amount of addition of *n*-decane. However, the ignition delay times of *n*-decane show much low sensitivity with small amount of addition of AMN. Therefore, the high amount of AMN needs to be added to change the cetane number.

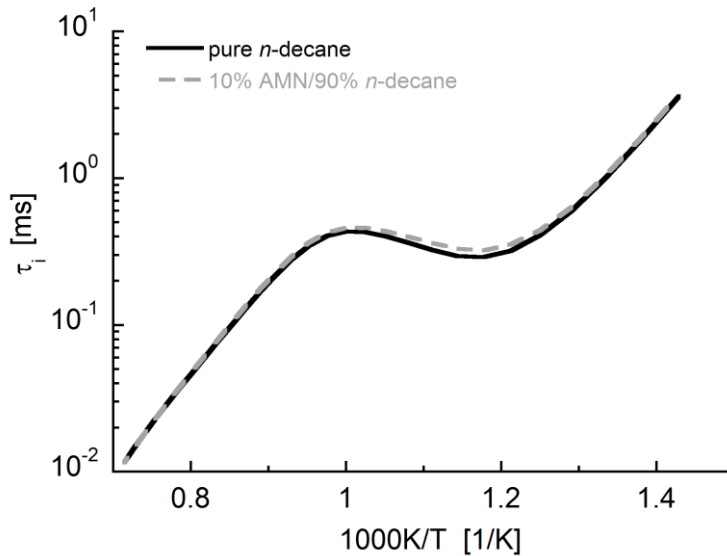


Figure 4.6: Ignition delay times of *n*-decane, 10/90 blend in air at $p = 40$ bar, $\phi = 1$

4.4.2 Influence of pathway for $A_2CH_2 + HO_2$

Two versions of mechanism model with respective rate coefficients were prepared to show the influence of pathway for $A_2CH_2 + HO_2$. As shown in Table 4.7, the first column shows names for different mechanism models and second column show the respective used rate coefficients. Except the rate coefficients listed in Table 4.7, all other reactions within these two mechanisms were exactly same.

Table 4.7: Used rate coefficients for $A_2CH_2 + HO_2$ reactions

names	Used rate coefficients				
Original	$A_2CH_2 + HO_2 \Rightarrow OH + H + A_2CHO$	7.60E+12	0	0	! Hippler*2
	$A_2CH_2 + HO_2 \Rightarrow OH + CH_2O + A_2-x$	2.40E+12	0	0	! Hippler*2
Faster	$A_2CH_2 + HO_2 \Rightarrow OH + H + A_2CHO$	2.50E+14	0	0	! Emdee(\approx Hippler*80)
$A_2CH_2 + HO_2$	$A_2CH_2 + HO_2 \Rightarrow OH + CH_2O + A_2-x$	8.00E+13	0	0	! Emdee(\approx Hippler*80)

The experimental ignition delay times of pure AMN, 70/30, 30/70 (in mole) are compared with corresponding simulations at $\phi = 1.0$, $p = 40$ bar in Figure 4.7. For comparison, the

simulations of pure *n*-decane at 40 bar are also depicted in the Figure 4.7. However there is no available experimental for pure *n*-decane at 40 bar. In the following discussion, reactions: $A_2CH_2 + HO_2 \Rightarrow OH + H + A_2CHO$ and $A_2CH_2 + HO_2 \Rightarrow OH + CH_2O + A_{2-x}$ are referred as “chain propagation pathway of $A_2CH_2 + HO_2$ ”.

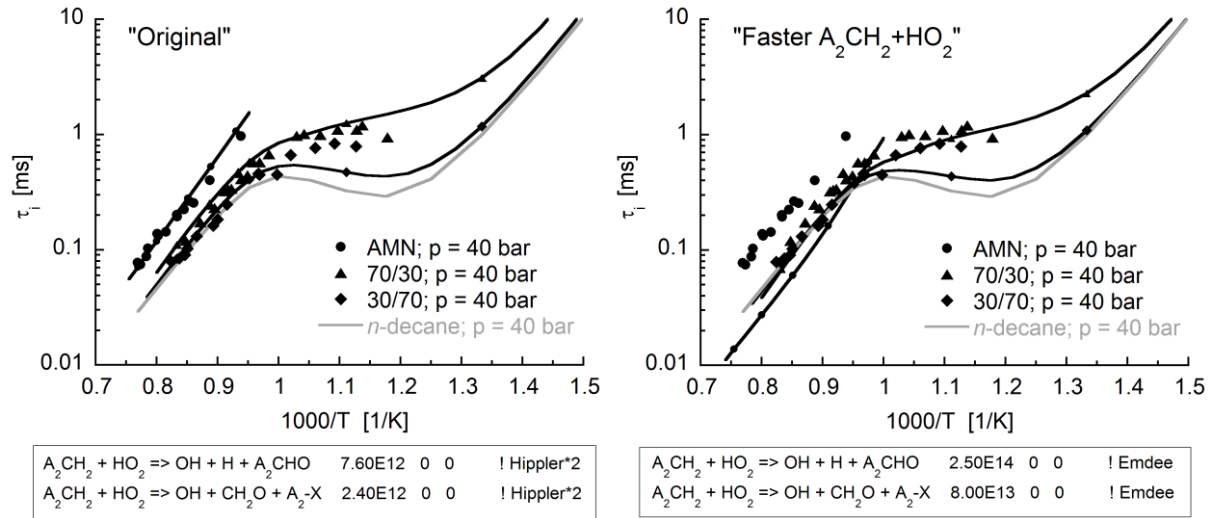


Figure 4.7: Experimental [86] (symbols) and simulated (lines) ignition delays for AMN, 70% AMN/30% *n*-decane, 30% AMN/70% *n*-decane, *n*-decane at $\phi = 1.0$ and $p = 40$ bar.

With much faster reaction coefficients from Emdee et al. [88] for chain propagation pathway of $A_2CH_2 + HO_2$, the ignition delay times of pure AMN is greatly decreased; meanwhile the ignition delay times of 70/30 and 30/70 blend (namely IDEA blend) are correspondingly decreased. In the temperature region from 1100 K, the ignition delay times of pure AMN, 70/30 and IDEA blend show abnormal results when comparing with experimental data: $\tau_{AMN} < \tau_{70/30} < \tau_{IDEA\ blend} < \tau_{n-decane}$. The reactivity of chain propagation pathway of $A_2CH_2 + HO_2$ clearly dominates the reactivity of pure AMN.

For more detailed analysis of chain propagation pathway of $A_2CH_2 + HO_2$, simulations were performed with IDEA blend in air at $\phi = 1.0$, $p = 40$ bar and $T = 675$ K ($1000/T = 1.48$) in a constant volume reactor. Figure 4.8 shows the oxygen flows and net reaction analyses in the initiation stage by applying final time as 7.2 ms to show the initiation stage. The oxygen flow is selected because oxygen flow includes all the target reactions in a compact structure.

From the Figure 4.8 (right), the faster chain propagation pathway of $A_2CH_2 + HO_2$ produces small amounts of OH radicals and H radicals more rapidly. These formed radicals promote the initial fuel decomposition of *n*-decane ($n-C_{10}H_{22}$) and AMN (A_2CH_3), which can be seen from the values of oxygen flows. The faster fuel decomposition results in faster formation of reactive radicals such as OH, H, O, etc. These radicals in turn speed up the fuel

decomposition. The reaction: $s\text{-C}_{10}\text{H}_{20}\text{O}_4\text{H-6r} \Rightarrow s\text{-HO}_2\text{C}_{10}\text{H}_{19}\text{O-6r} + \text{OH}$ is the fastest among the decomposition pathway of peroxy hydroperoxical radicals. This reaction is selected to represent the OH formation source from *n*-decane and other similar reactions are not shown here due to space limitation. From the net reaction analysis of “OH formation”, the decomposition of peroxy hydroperoxical radicals (such as $s\text{-C}_{10}\text{H}_{20}\text{O}_4\text{H-6r} \Rightarrow s\text{-HO}_2\text{C}_{10}\text{H}_{19}\text{O-6r} + \text{OH}$) is the major OH formation source before auto-ignition. Therefore, the influence of chain propagation pathway of $\text{A}_2\text{CH}_2 + \text{HO}_2$ by using IDEA blend as fuel is much less than using pure AMN as fuel. When using pure AMN as fuel, chain propagation pathway of $\text{A}_2\text{CH}_2 + \text{HO}_2$ is the major OH formation source alone before auto-ignition. Hence, the faster chain propagation pathway of $\text{A}_2\text{CH}_2 + \text{HO}_2$ greatly influences the reactivity of AMN as shown in the Figure 4.7.

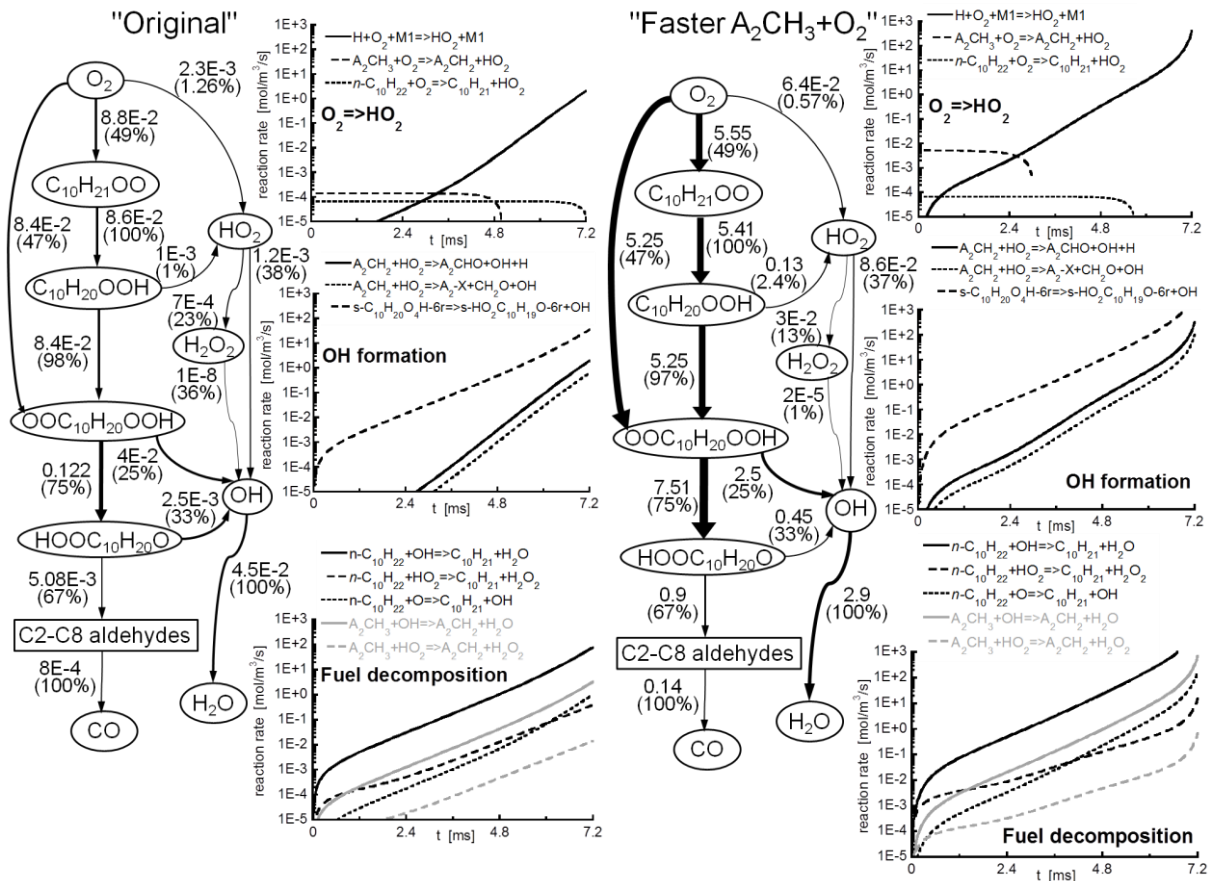
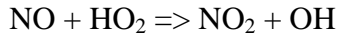


Figure 4.8: Oxygen flow with IDEA blend in air at $\phi = 1.0$, $p = 40$ bar, $T = 675$ K ($1000/T = 1.48$) and $\tau_{\text{final}} = 7.2$ ms in a constant volume reactor by using different reaction coefficients for chain propagation pathway of $\text{A}_2\text{CH}_2 + \text{HO}_2$

By using the extreme faster rate coefficients from Emdee et al. [88], the before discussed reactions of $\text{A}_2\text{CH}_2 + \text{HO}_2$ has a high sensitivity on the reactivity of AMN and *n*-decane blends. The chain propagation pathway of $\text{A}_2\text{CH}_2 + \text{HO}_2$ eliminates the chain breaking

effect of HO₂ formation. This effect can be compared with the influence of NO on the NTC regime of paraffinic hydrocarbons [118-120], which may cause increased engine knock in SI-engines [121, 122].



NO available in the engine from internal or external EGR influences the next engine cycle.

Although the rate coefficients from Hippler et al. [98]. are applied in current study, the interaction between AMN and *n*-decane is still not fully understood. Further investigations are of necessary for understanding the oxidation model of AMN and blends of AMN/*n*-decane.

4.5 Mechanism validations for pure *n*-decane and pure AMN

4.5.1 Ignition delay times

- *n*-decane

Ignition delay time is one of the most important characteristic parameters for the combustion process. There are plenty of measurements that can be taken if *n*-decane is used as fuel. According to the different fuel-air equivalence ratios, the comparison of experimental data and simulated values is plotted in Figure 4.9 to Figure 4.12.

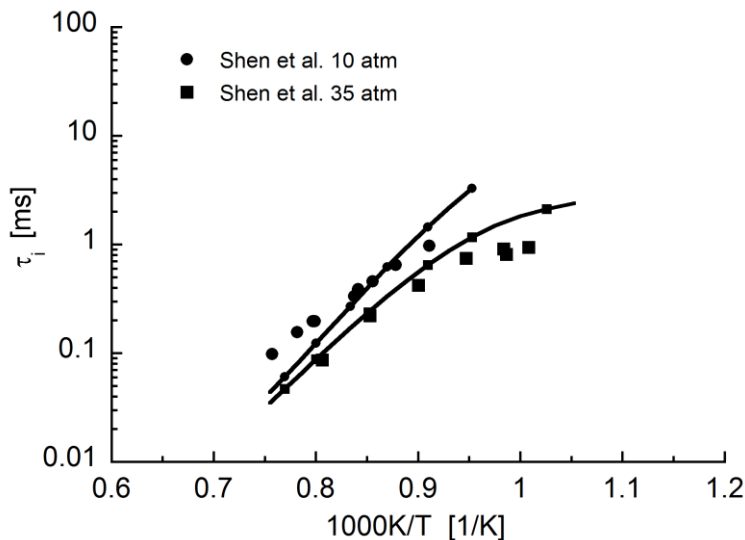


Figure 4.9: Simulated and experimental ignition delay times [50] for *n*-decane/air mixtures with $\phi = 0.25$

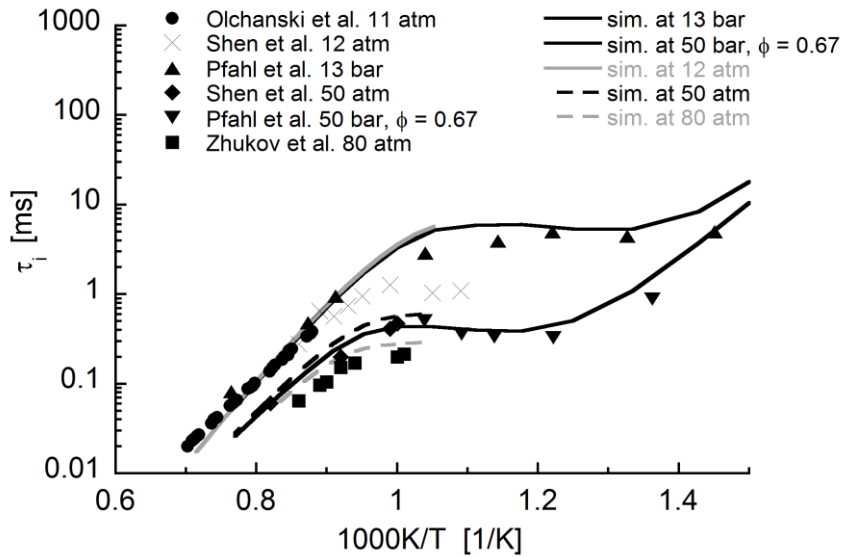


Figure 4.10: Simulated and experimental ignition delay times [47, 49-51] for *n*-decane/air mixtures with $\phi = 0.5/0.67$

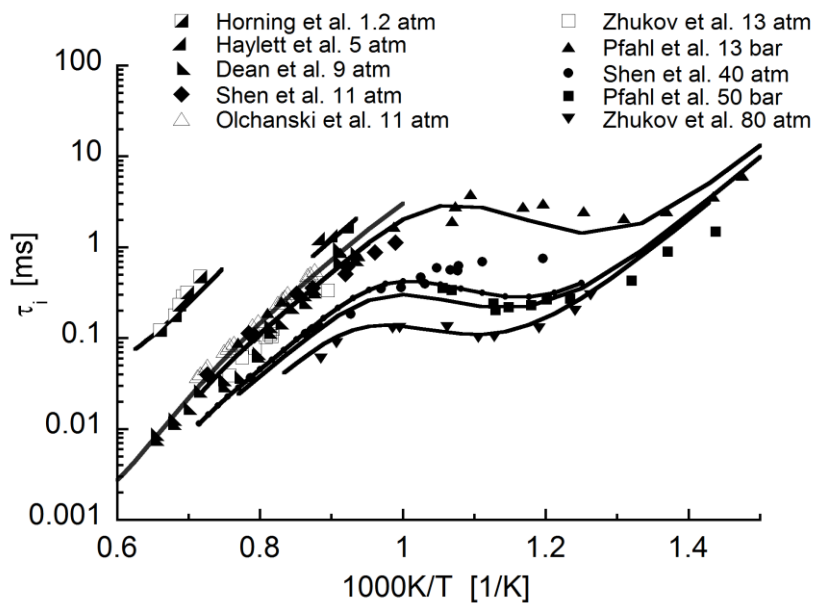


Figure 4.11: Simulated and experimental ignition delay times [47-53] for *n*-decane/air mixtures with $\phi = 1$

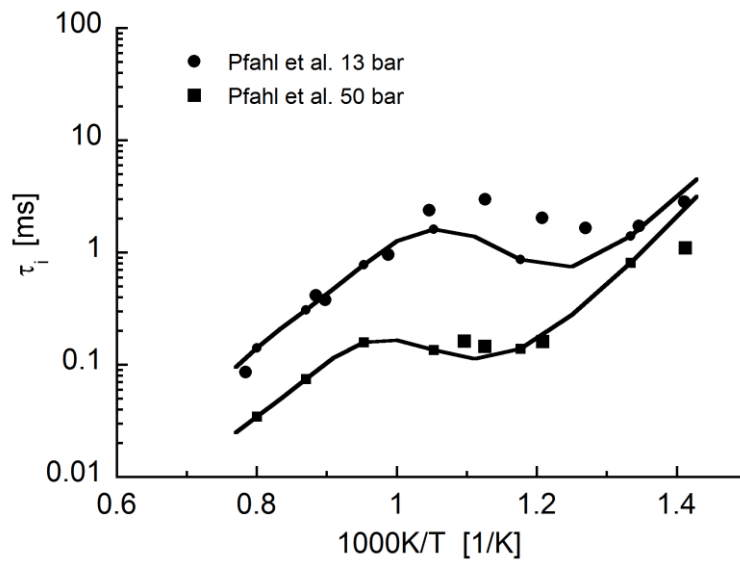


Figure 4.12: Simulated and experimental ignition delay times [47] for *n*-decane/air mixtures with $\phi = 2$

In general, the simulated ignition delay times agree with the experimental values in stoichiometric and fuel-rich conditions. In fuel-lean conditions, the simulated values are a little greater than the measured values in the high-temperature region at 10 atm.

- AMN

The ignition delay times of pure AMN were experimentally investigated by Pfahl et al. [47] and later by Wang et al. [86] as shown in Figures 4.13 - 4.15. It can be observed that with $\phi = 0.5, 1,$ and $1.5,$ the simulated ignition delay times at 10 bar generally match the experimental values, and that in the high-temperature region, there appears to be a little over-prediction. At 40 bar, the deviations between the simulated and the experimental values are obvious and the deviations increase with the increase in the fuel/air ratio.

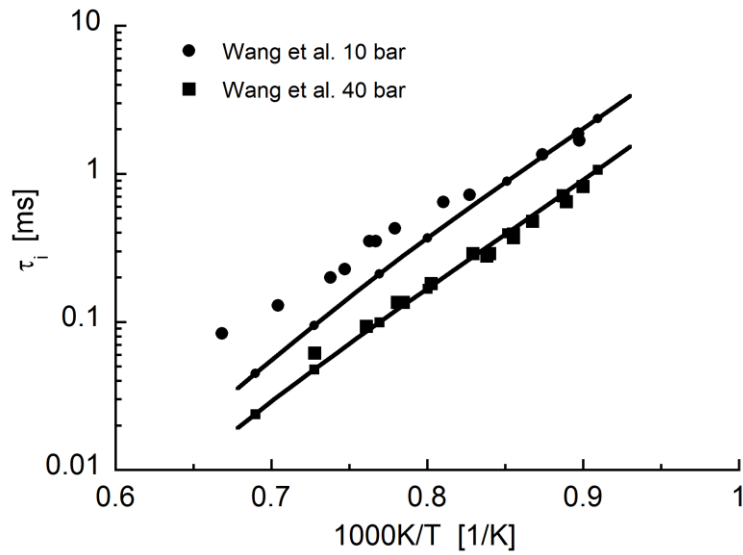


Figure 4.13: Simulated and experimental ignition delay times [86] for AMN/air mixtures with $\phi = 0.5$

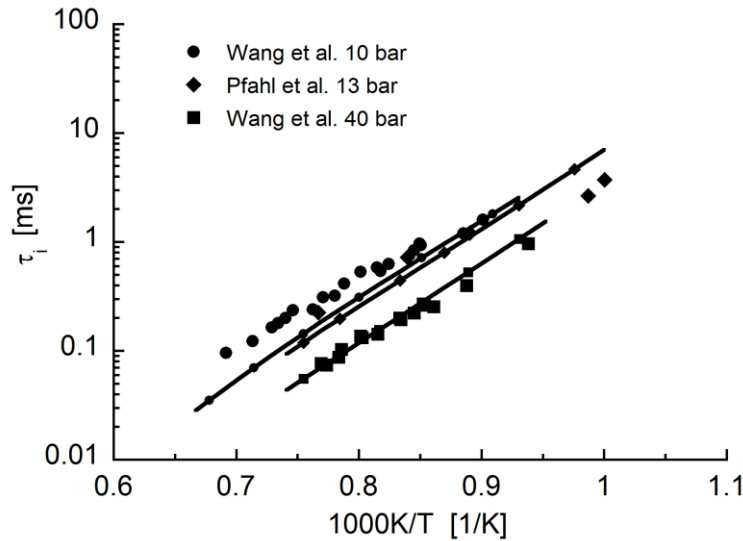


Figure 4.14: Simulated and experimental ignition delay times [47, 86] for AMN/air mixtures with $\phi = 1.0$

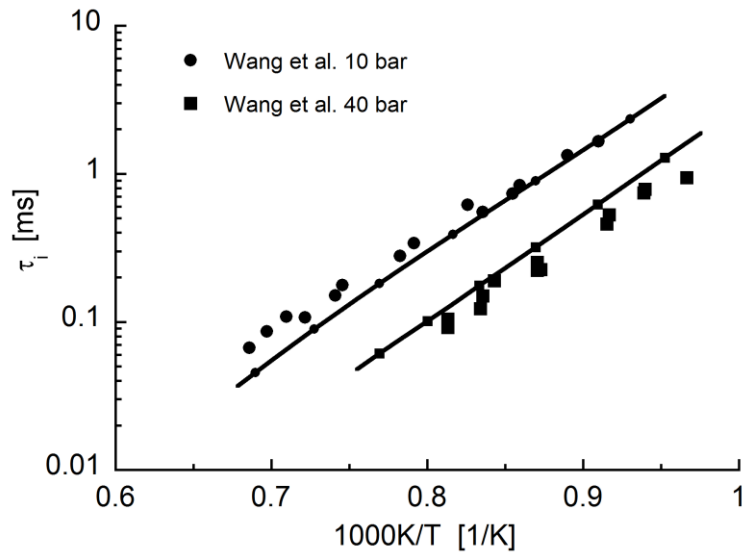


Figure 4.15: Simulated and experimental ignition delay times [86] for AMN/air mixtures with $\phi = 1.5$

4.5.2 Laminar flame speeds

- *n*-decane

Laminar flame speed is another common characteristic parameter for combustion. Figure 4.16 shows atmospheric laminar flame velocities for *n*-decane/air mixtures at temperatures from 300 K to 500 K [54-56].

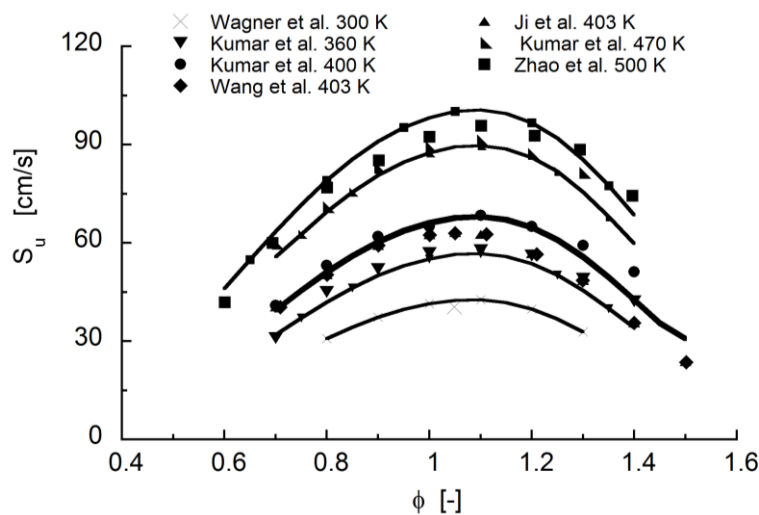


Figure 4.16: Simulated and experimental laminar flame speeds for *n*-C₁₀H₂₂/air mixtures at $p = 1$ atm, $T = 300$ K [54]; 360, 400, 470 K [56]; 403 K [57]; 403 K [58]; 500 K [55]

The simulated laminar flame velocities agree with the experimental data in a broad range of equivalence ratios. Due to different approaches, the flame speeds at 403 K reported by Ji et al. [58] and Wang et al. [57] have fine coincidence while their values are much slower

than the flame speed at 400 K reported by Kumar et al. [56]. Possible reasons may be the different calculation approaches or the degree of precision.

To date, there is no measurement for the laminar flame speed of AMN.

4.5.3 Jet stirred reactor

- *n*-decane

With the help of a JSR experiment, detailed chemistry information such as major and minor species concentration can be investigated. The detailed speciations are validated against JSR experiments for a stoichiometric *n*-decane/air mixture [45] at 10 bar in the Figure 4.17.

Figure 4.19 shows good agreement between the simulations and the experimental data for major species such as *n*-decane, O₂, CO, and CO₂. In the intermediate temperature region, CO₂ is generally under-predicted by the model when compared to the experiments. In the same region, CO is over-predicted. For important intermediate species, C₂H₆ and C₂H₄ are clearly under-predicted while the secondary decenes from the fuel and 1-hexene are obviously over-predicted. Other intermediate species have acceptable agreement.

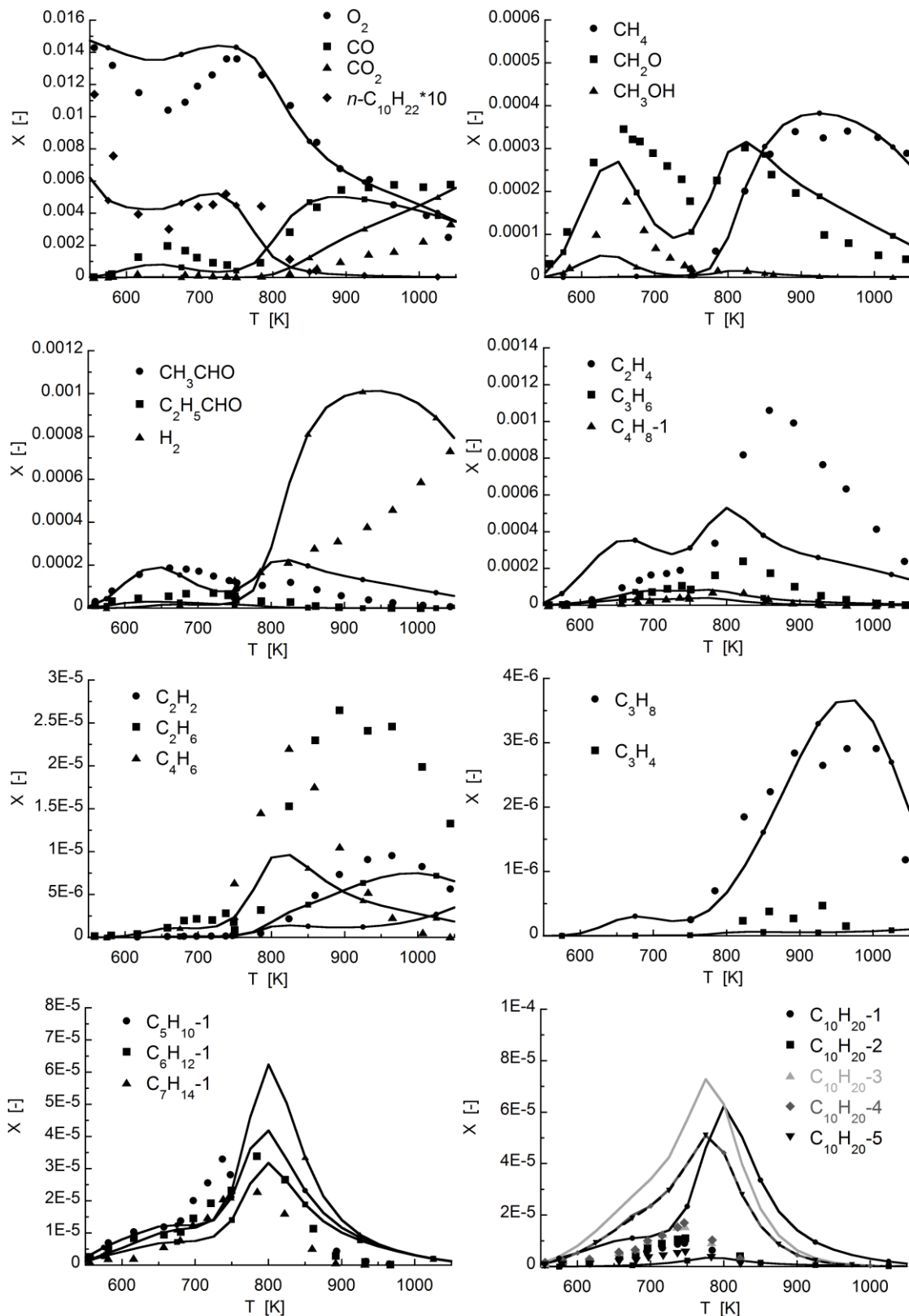


Figure 4.17: Simulated and experimental species profiles [45] in JSR for $n\text{-C}_{10}\text{H}_{22}$ /air mixtures at $p = 10$ atm, $\phi = 1$, and $\tau = 1$ s

Apart from the validation of JSR at 10 atm, Figure 4.18 and Figure 4.19 illustrate the validation of JSR under higher pressure conditions. At 40 atm, the species profiles of O_2 and CO are over-predicted compared to the experimental values, while the species profile of CO_2

is under-predicted compared to the experimental values. This observation is also found in the validation of JSR at $p = 10$ atm and that at $p = 20$ atm. The species profiles of CH_4 , C_2H_4 , and CH_2O are acceptable at 40 atm, while at 20 atm, the species profiles of CH_4 and C_2H_4 are much under-predicted.

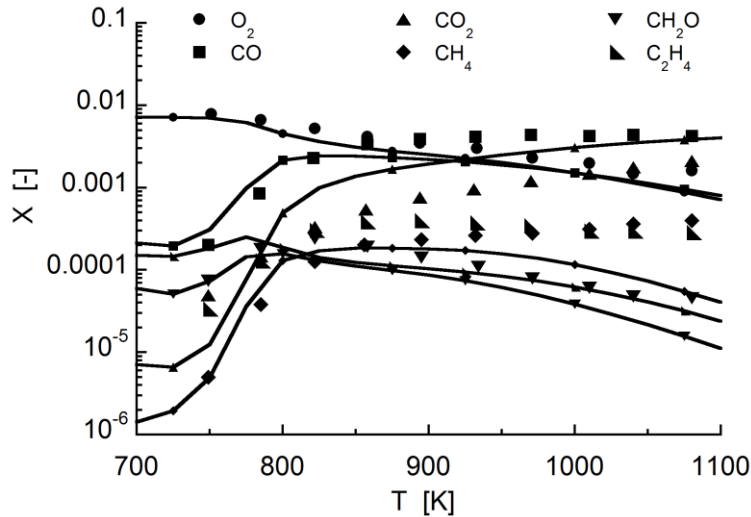


Figure 4.18: Simulated and experimental species profiles [60] in JSR for $n\text{-C}_{10}\text{H}_{22}/\text{air}$ mixtures at $p = 20$ atm, $\phi = 1$, and $\tau = 1$ s

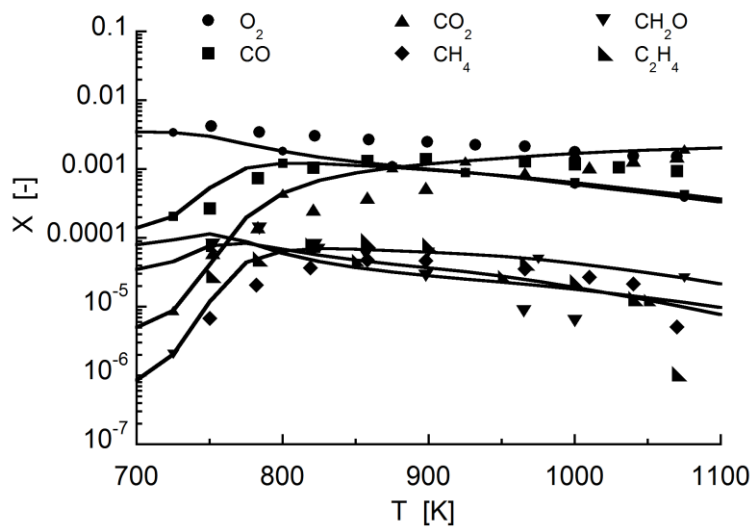


Figure 4.19: Simulated and experimental species profiles [60] in JSR for $n\text{-C}_{10}\text{H}_{22}/\text{air}$ mixtures at $p = 40$ atm, $\phi = 1$, and $\tau = 1$ s

- AMN

The AMN model is validated against the JSR experiments at high-temperatures between 800-1200 K, $\phi = 1$, $p = 10$ bar, and $\tau = 0.5$ s [85]. As shown in Figure 4.20, there is good agreement between the simulations and the experimental data for pure AMN, O_2 , and CO_2 . The simulated species profile of CO is slightly under-predicted. The species profiles of

H_2 , A_2 , A_2CHO , indene, and CH_2O are acceptable. The species profile of C_2H_4 is nearly ten times less than predicted, which is something that needs to be improved in future work.

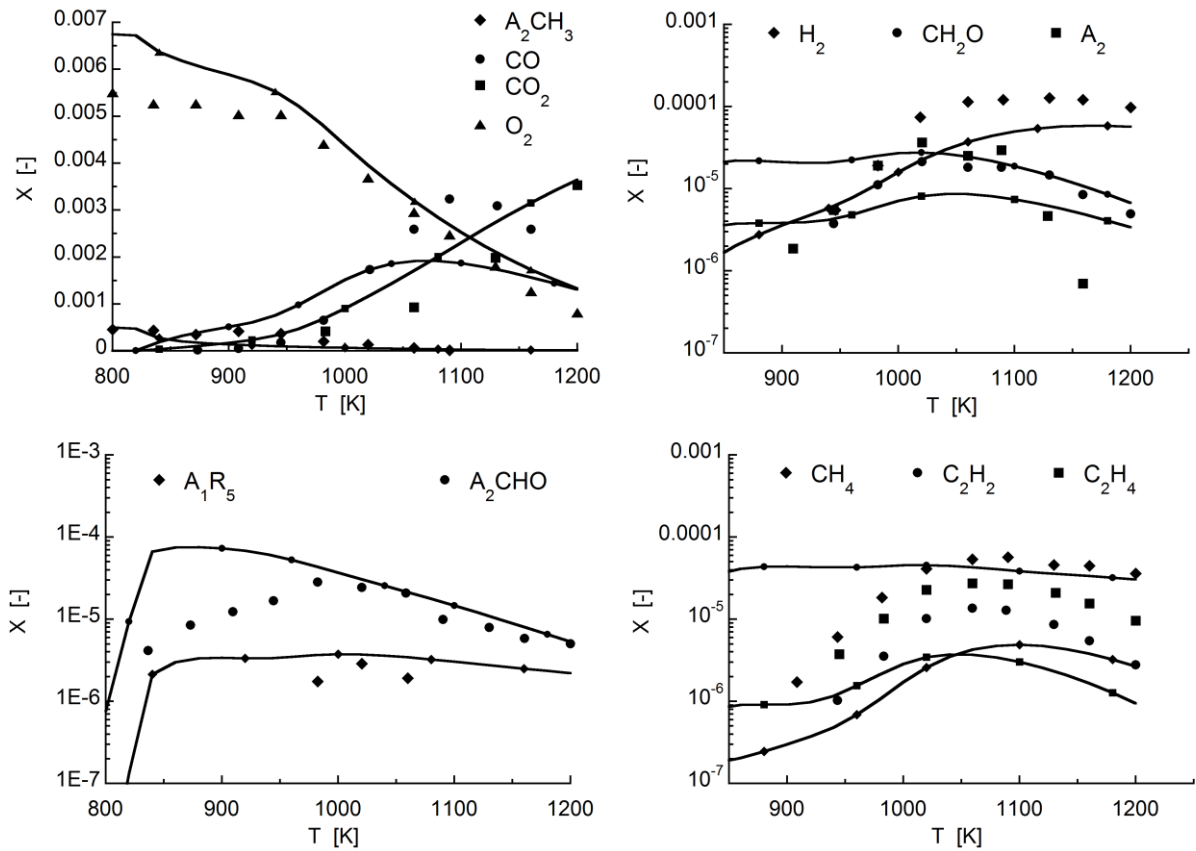


Figure 4.20: Simulated and experimental species profiles [85] in JSR for AMN/air mixtures at $p = 10$ atm, $\Phi = 1$, and $\tau = 0.5$ s

4.5.4 Premixed flame speciation

- *n*-decane

Doute et al. [65] performed premixed flame speciation with rich *n*-decane/ N_2/O_2 mixtures at 1 atm. The simulated major and intermediate species profiles have good agreement with the measured values depicted in Figure 4.21. In general, the deviations between the simulated and measured values are fairly negligible.

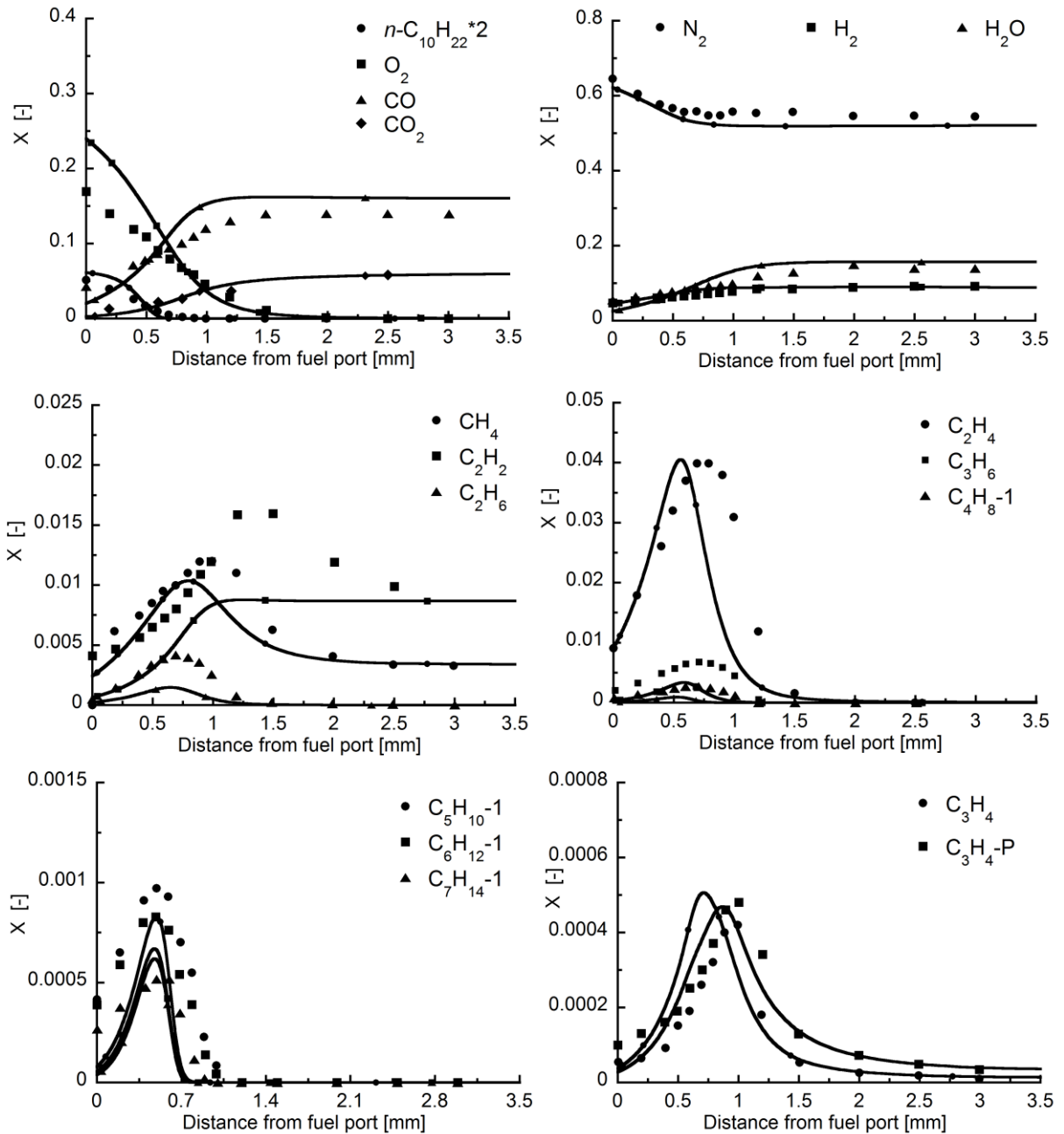


Figure 4.21: Simulated and experimental species profiles [65] in a rich *n*-decane/ N_2/O_2 flame

4.6 Mechanism validations for IDEA fuel blends

4.6.1 Ignition delay times

The ignition delay times of the AMN/*n*-decane blend were experimentally investigated by Wang et al. [86]. They compared the experiments for pure AMN, *n*-decane, and two blends 30/70 and 70/30 (in mole) at $\phi = 1.0$, $p = 10$ bar, and $p = 40$ bar, as shown in Figure 4.22 and Figure 4.23. The simulations agree well with the experiments performed at high-temperatures at 40 bar. At 10 bar, the model predicts faster ignition delay times for AMN, 70/30, and 30/70

blends in the high-temperature region. The difference between the validations at 10 bar and 40 bar may be the absence of some pressure-dependent reactions relevant to AMN models.

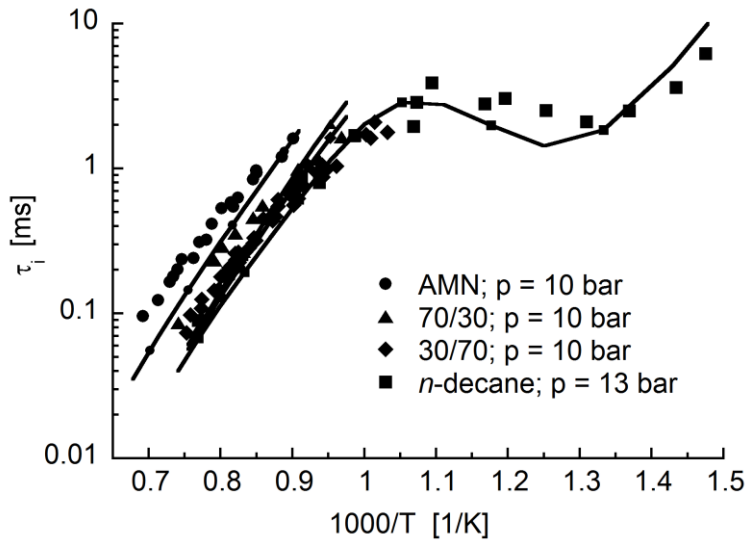


Figure 4.22: Simulated and experimental ignition delay times [86] for stoichiometric AMN, 70% AMN/30% *n*-decane, 30% AMN/70% *n*-decane, and pure *n*-decane in air at 10, 13 bar

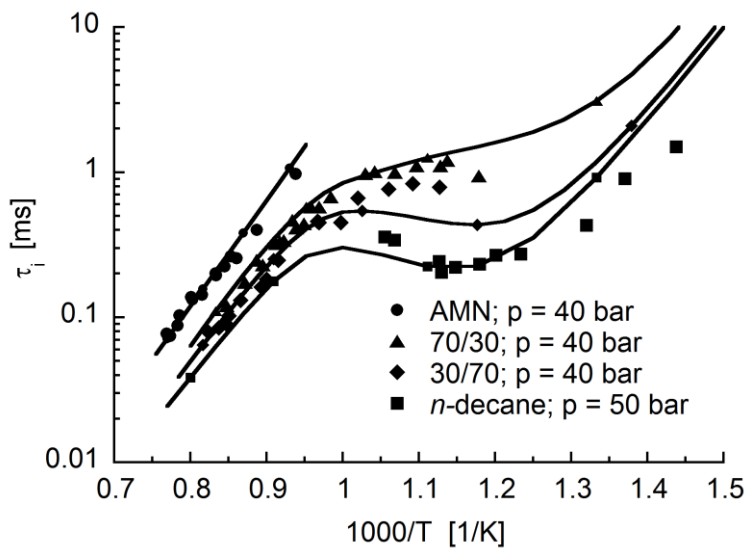


Figure 4.23: Simulated and experimental ignition delay times [86] for stoichiometric AMN, 70% AMN/30% *n*-decane, 30% AMN/70% *n*-decane, and pure *n*-decane in air at 40, 50 bar

4.6.2 Jet stirred reactor

Figure 4.24 shows a comparison of the simulations and the experimental values for the IDEA surrogate fuel blend at $T = 550\text{--}1100\text{ K}$, $p = 10\text{ bar}$, $\phi = 1$, and $\tau = 1\text{ s}$ [33]. The model predicts the speciation of the fuel and major products such as CO and CO₂ from low- to high-temperature regions well. The under-prediction of CO concentration is consistent with the over-prediction of CO₂ concentration, both of which are similar to the JSR results for *n*-

decane/air mixtures at the same pressure and in the same temperature region. The speciation of other species is fairly acceptable.

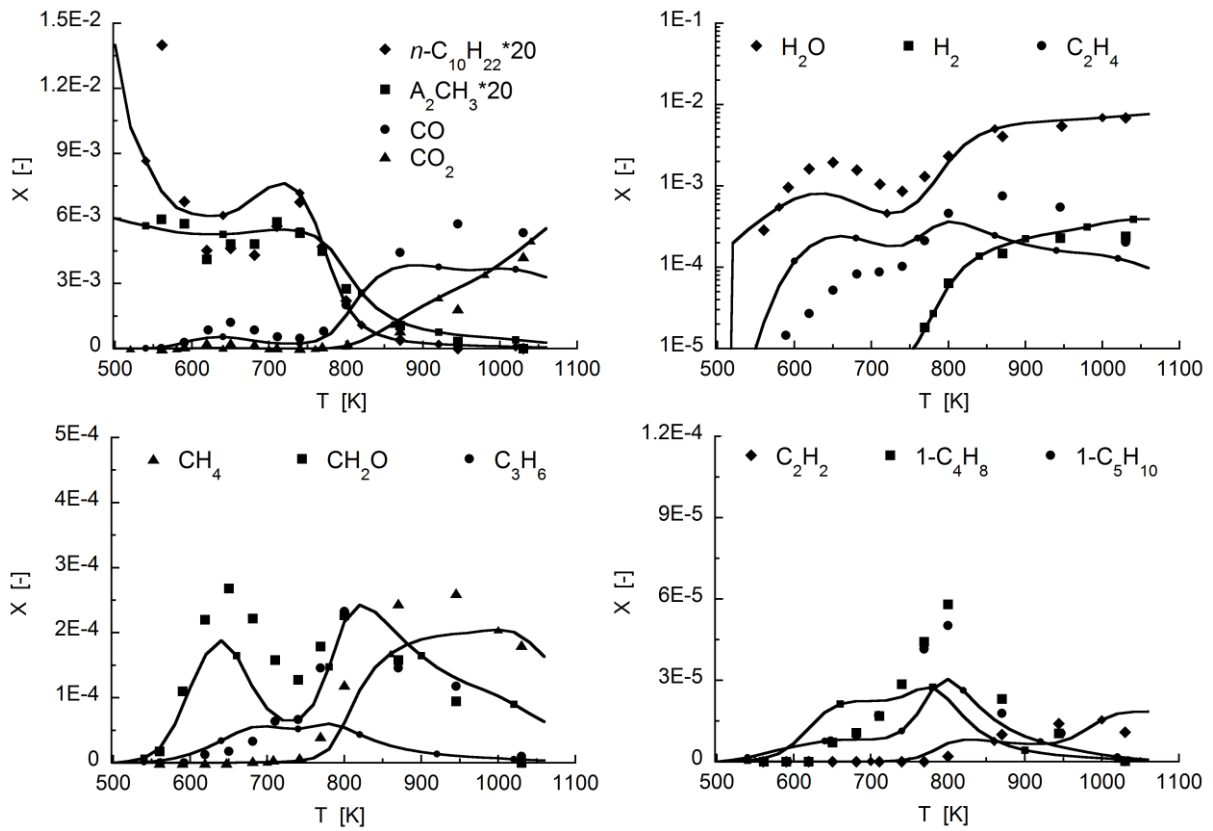


Figure 4.24: Simulated and experimental species profiles [110] in a JSR for the IDEA blend in air at $p = 10$ atm, $\phi = 1.0$, and $\tau = 1$ s

4.7 Surrogate fuel for diesel

Commercial diesel fuels are complex mixtures of hundreds of individual species. Their components consist of normal paraffins, *iso*-paraffins, *cyclo*-paraffins, aromatics, and multi-ring aromatics. Farrell and colleagues [44] and later Pitz and colleagues [123] reviewed different diesel surrogates as listed in Table 4.8.

Table 4.8 Component candidates for diesel surrogates [44]

Normal Paraffins	<i>iso</i> -Paraffins	<i>cyclo</i> -Paraffins	Single-Ring Aromatics	Multi-Ring Aromatics
<i>n</i> -heptane	<i>iso</i> -octane	methyl-cyclohexane	toluene	tetralin
<i>n</i> -decane	<i>iso</i> -cetane	ethyl/propyl/butyl cyclohexane	ethyl/propyl/butyl benzene	α -methylnaphthalene
<i>n</i> -dodecane		decalin	<i>n</i> -decylbenzene	
<i>n</i> -hexadecane				

Among these component candidates, the IDEA blend is the most well-known surrogate blend and investigated by many studies [2, 86, 110-112].

4.7.1 Ignition delay times

The ignition delay times of a US commercial No.2 diesel fuel (DF-2 diesel) were studied by Penzyakov et al. [124] in a heated shock tube with equivalence ratios from 0.5 to 2.0 at $p = 4.7\text{-}10.4$ atm and $T = 1065\text{-}1838$ K. The comparison of experimental data for diesel fuels and the computational results at $\phi = 0.5, 1.0,$ and 2.0 are shown in Figure 4.25. The simulated ignition delay times of the current IDEA blend are faster than those of the experimental values in the high-temperature region for three fuel/air equivalence ratios.

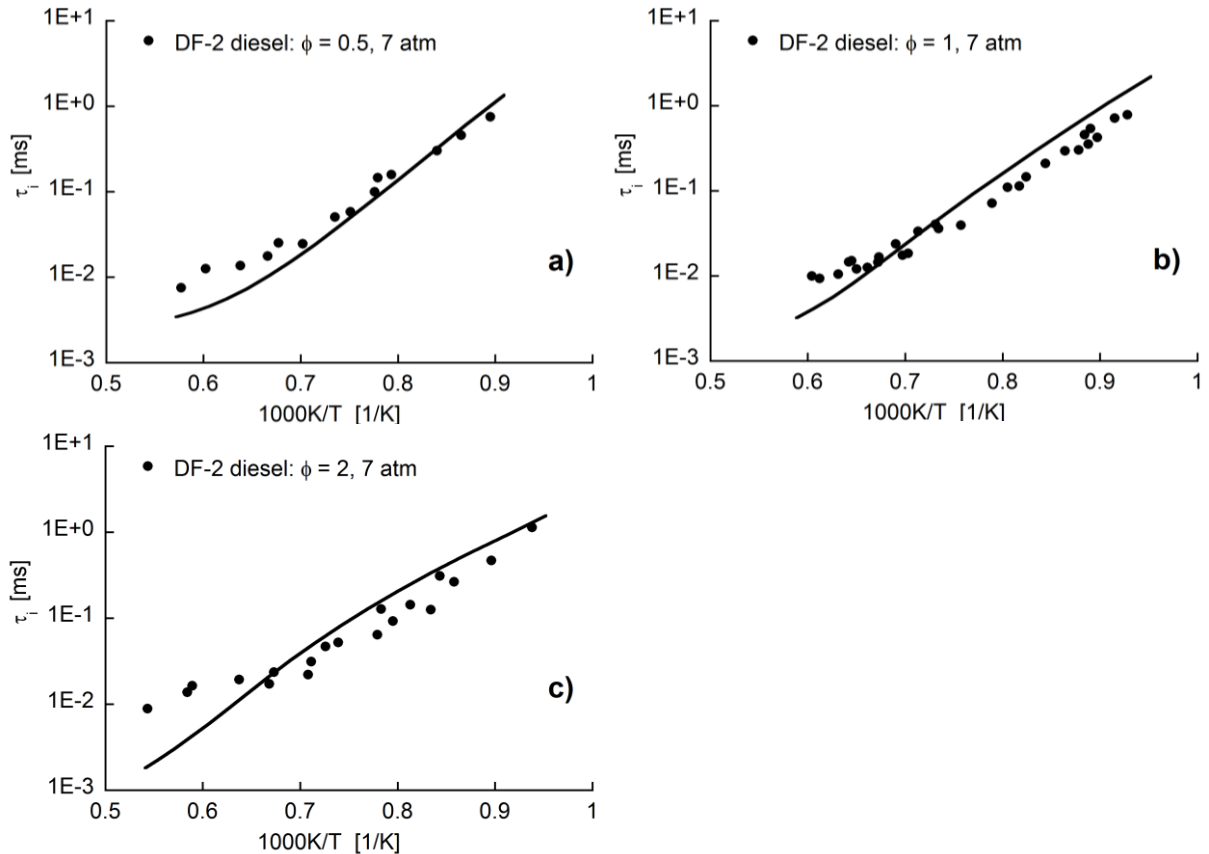


Figure 4.25: Simulated and experimental ignition delay times [124] of US DF-2 diesel/air mixtures at 7 atm

Haylett et al. [125] measured the ignition delay times of diesel fuels in an aerosol shock tube. Figure 4.26 shows the ignition delay times for mixtures consisting of commercial US DF-2 diesel/21% O_2 /Ar. In fuel-lean conditions ($\phi = 0.4$) at 7 atm, the simulations fit well with the experimental data. In fuel-rich conditions ($\phi = 1.3$) at 3 atm, the simulated ignition delay times are much slower than the experimental values. This behavior is consistent with

the slower ignition delay times of pure *n*-decane or pure AMN validation in the temperature region of 1100-1000 K as shown in the previous section.

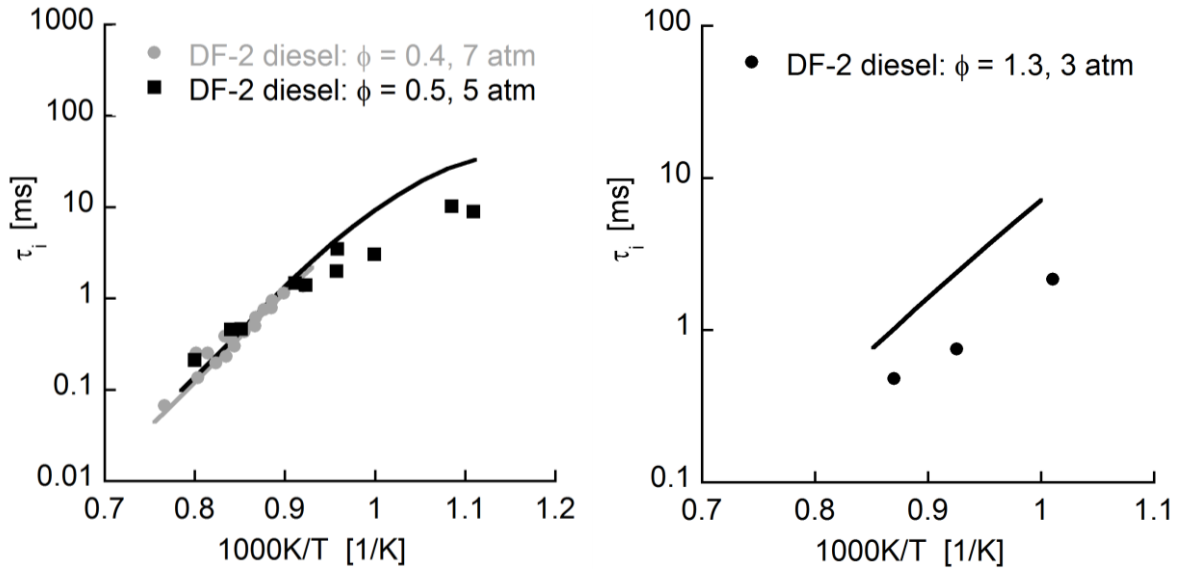


Figure 4.26: Simulated and experimental ignition delay times [125] for US DF-2 diesel /21% O₂/Ar

Three years later, Haylett and his colleagues [53] performed another ignition delay time experiment for DF-2 diesel fuels in an aerosol shock tube as depicted in Figure 4.27.

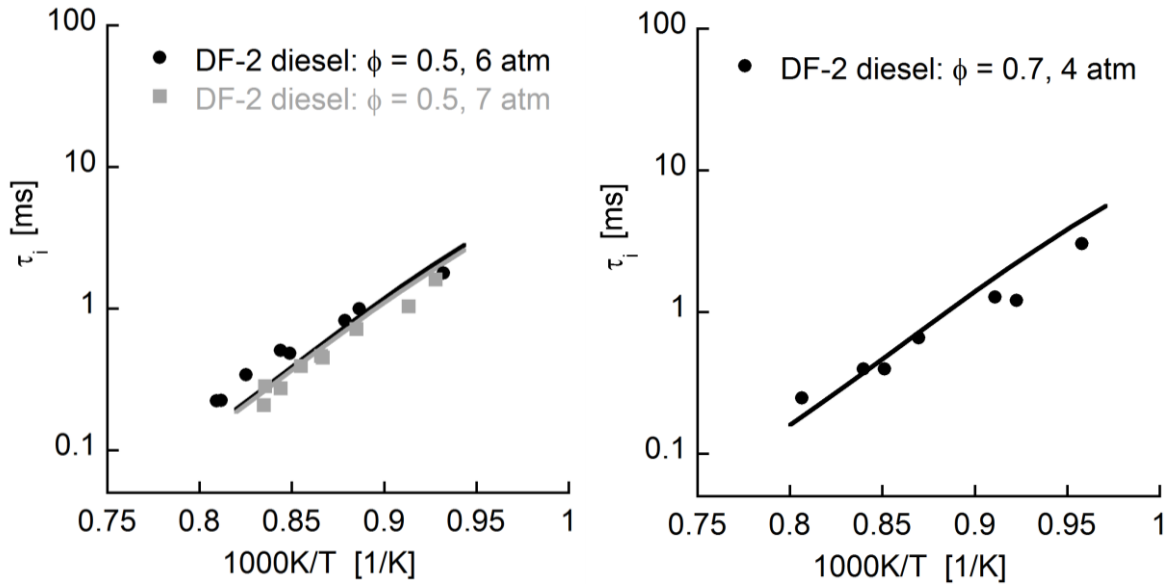


Figure 4.27: Simulated and experimental ignition delay times [53] for DF-2 diesel/21% O₂/Ar

For fuel-lean conditions ($\phi = 0.5$), the simulated ignition delay times at 6 and 7 atm almost coincide with each other, while the experimental data have obvious differences. The simulated values fit better with the experimental data at 7 atm than at 6 atm. For the condition with $\phi = 0.7$, the simulated ignition delay times agree with the experimental values in the measured temperature region.

Since two experiments from Haylett’s research group include similar experimental conditions with fuel air ratios close to 0.5 and pressures around 7 atm, the corresponding experimental data were normalized to 7.4 atm and $\phi = 0.5$ using p^{-1} and ϕ^{-1} scaling, which is depicted in Figure 4.28.

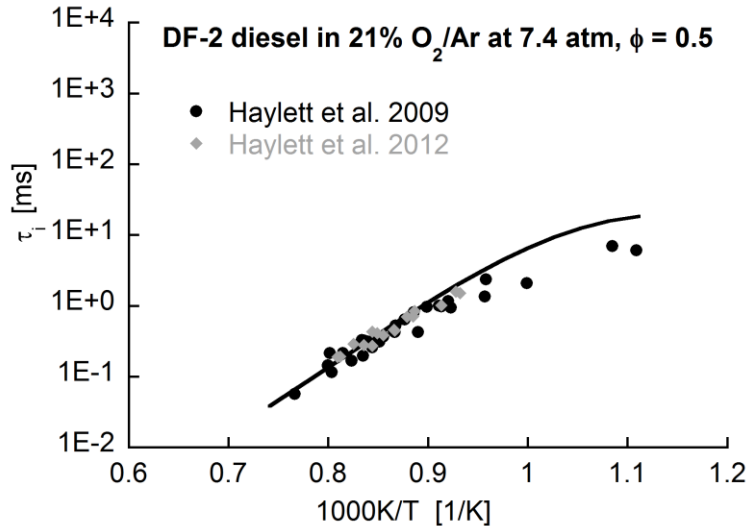


Figure 4.28: Comparison of experimental ignition delay times for DF-2 diesel/21% O₂/Ar

In addition to the experiments done by Haylett and his colleagues, the experiments performed by Spadaccini et al. [126] in the low-temperature and NTC region and those by Penzyakov et al. [124] in the high-temperature region are collected in Figure 4.29.

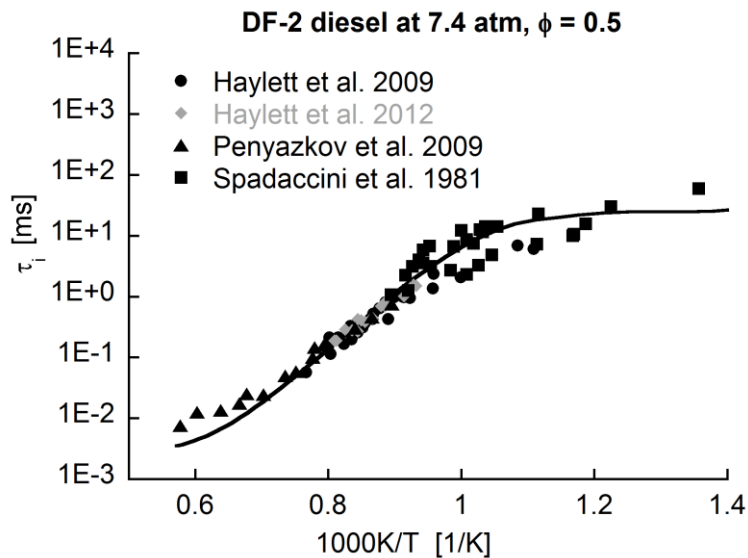


Figure 4.29: Comparison of experimental ignition delay times for DF-2 diesel

The experimental data from Spadaccini et al. [126] were normalized to 7.4 atm and $\phi = 0.5$ using p^{-1} and ϕ^{-1} scaling consistent with the experiment conditions of Penzyakov et al. [124]. In the NTC region, there are clear differences between the data from Spadaccini et al.

[124] and those from Haylett et al. [125], while the simulated values are in the middle of these two experiments. In general, the simulation of the IDEA blend fits with these four experiments in fuel-lean conditions at 7.4 atm.

The chemical and physical properties of the IDEA blend and DF-2 diesel are collected in Table 4.9.

Table 4.9 Chemical and physical properties of IDEA blend and DF-2 diesel

Property	IDEA blend [3]	DF-2 diesel [3, 127]
Cetane number	53	56
Density (20 °C) [kg/m ³]	817	840
Kinematic viscosity (40 °C) [mm ² /s = cSt]	-	2.6
Hydrogen/carbon ratio	1.79	1.80

In general, the properties of the IDEA blend are close to those of DF-2 diesel. However, the cetane number of IDEA blend is still a little different from that of DF-2 diesel. Since the cetane number of 74% *n*-decane/26% AMN blend is equal to that of DF-2 diesel, it is of interest to investigate the validations of 74% *n*-decane/26% AMN blend in the future work.

4.7.2 Laminar flame speeds

Figure 4.30 (left side) shows the experimental laminar flame speeds for ultra-low sulfur diesel and *n*-decane at 470 K under atmospheric pressure. They are compared with the simulations of *n*-decane, AMN, and the IDEA blend. The current model has good agreement with the experimental laminar flame speeds for *n*-decane at 470 K and those of diesel fuels at 470 K. Looking at the simulation results, it is clear that increased AMN composition decreases the flame speed. However, in fuel-rich conditions ($\phi=1.3-1.5$), the deviations between the experimental data and the simulation are obvious. From this point of view, some important reaction pathways in fuel-rich conditions are missing in this model.

Figure 4.30 (right side) shows the experimental laminar flame speeds for DF-2 diesel at 623 K. The deviation between the experimental values and the simulated values of the IDEA blend is huge. The simulated flame speeds of *n*-decane are much slower than the experimental values. For comparison, the flame speed validation of *n*-decane at 500 K is also plotted. The current model predicts the measured flame speed of *n*-decane at 500 K well. More measurements of *n*-decane or diesel fuels are needed to determine the source of the deviation.

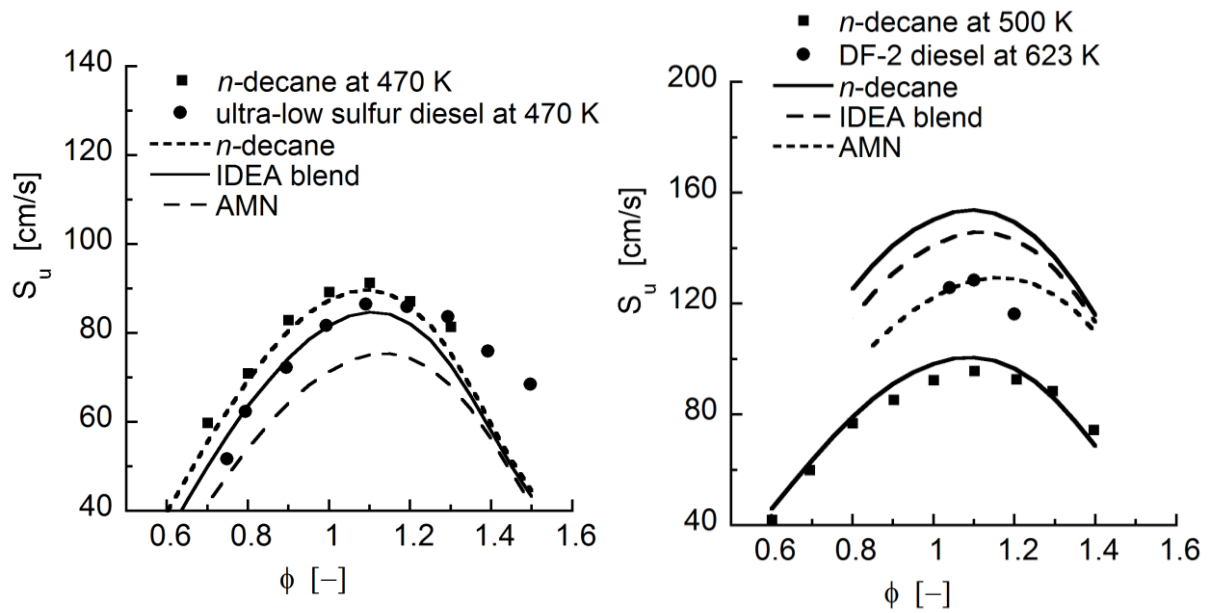


Figure 4.30: Simulated (lines) and experimental (symbols) flame speeds for diesels in air at 1 atm, 470 K [128], and 623 K [129]

Figure 4.31 shows a flame speed experiment for F-76 diesel at 443 K [130]. There, the fuel/air mass ratio is used instead of the equivalence ratio since the real C/H ratio for diesel fuels could not be determined. Consistent with the comparison at 470 K, the simulations for the lean side obviously have better agreement than the values on the rich side. To date, there is still a lack of enough measurements for determining the simulated behavior.

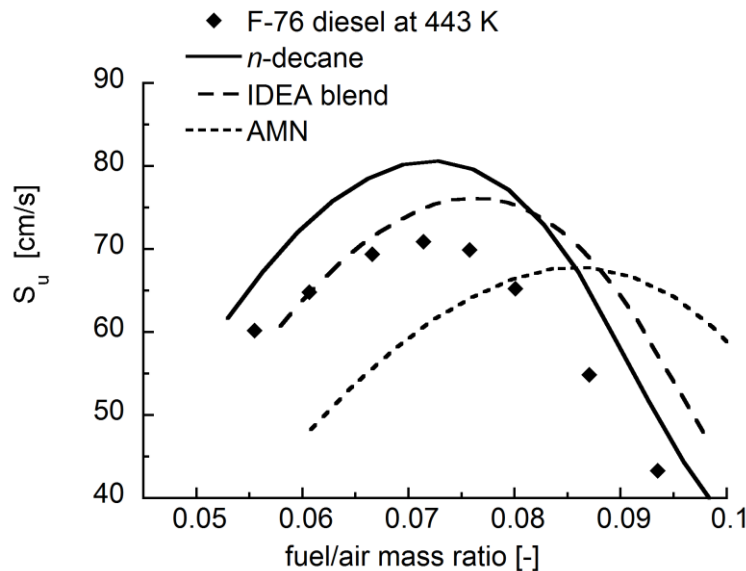


Figure 4.31: Simulated (lines) and experimental (symbols) flame speeds for diesels in air at 1 atm and 443 K

In this section, available diesel fuel experiments (five ignition delay times and three laminar flame speeds) are collected. The predictions of the current IDEA model show acceptable agreement regarding the experimental ignition delay times for different diesel fuels

and flame speeds measured at 443 and 470 K in fuel-lean and stoichiometric conditions. The predicted laminar flame speeds of diesel on the fuel-rich side at 470 K show obvious deviations; these deviations are related to the under-prediction of *n*-decane oxidation. Compared with diesel experiments at 623 K and 443 K, the current modeling behavior of the IDEA blend is unsatisfactory and more measurements of *n*-decane and diesel fuels are needed to determine the source of the deviation. The laminar flame speed experiments for AMN are of crucial importance for understanding the chemical mechanism modeling of AMN.

5 Kinetic mechanism of methyl-decanoate

5.1 Mechanism development for methyl-decanoate

MD [$\text{CH}_3(\text{CH}_2)_8\text{COOCH}_3$] is a typical fatty acid methyl-ester, which has a chain of ten carbon atoms and a methyl-ester group attached. MD is a common component in some bio-diesels. Table 5.1 summarizes the experimental and modeling studies using MD as fuel.

Table 5.1 Review of experiments and models for MD

Authors	Devices	Conditions		
		T [K]	p [atm]	Mixtures
Wang et al. [131]	ST	650-1400	15-16	$\phi = 0.5-1.5$ in air
Haylett et al. [53]	ST	1200-1350	8	0.2% <i>n</i> -decane, 3.1% O ₂ in Ar
Wang et al. [132]	ST	700-1300	20	$\phi = 1$ in air
Li et al. [133]	ST	900-1300	20;50	$\phi = 1$ in air
Campbell et al. [134]	ST	1050-1400	7	$\phi = 0.3; 1.4$ in Ar
Wang et al. [57]	Flame	403	1	$\phi = 0.6-1.4$ in air
Glaude et al. [135]	JSR	550-1150	1.06	$\phi = 1.0$ in air
Sarathy et al. [136]	diffusion flame	-	1	1.8% MD in N ₂ ; 42% O ₂ in N ₂
Detailed mechanism including high- and low-temperature oxidation pathways				
Herbinet et al. [46]	- JSR of rapeseed oil [137]; - Ignition delay of <i>n</i> -decane [47]; - Exhaust speciation in CFR engine			3036 species; 8555 reactions
Glaude et al. [135]	- JSR of MD (published with their model)			1251 species; 7171 reactions
Diévert et al. [138]	- JSR of MD [135]; - Ignition delay of MD [131]; - Laminar flame speed of MD [57]; - Diffusion flame extinction limits of MD [139]; - Speciation of MD in a diffusion flame [136]			530 species; 2396 reactions
Grana et al. [140]	- JSR of MD [135]; - Ignition delay of MD [131]; - Laminar flame speed for MD [57]; - Diffusion flame extinction limits for MD [139]; - Speciation in diffusion flame for MD [136]			~350 species; ~10,000 reactions
Reduced mechanism including high-temperature oxidation pathway alone				
Seshadri et al. [139]	- Reduced model from Herbinet et al. [46]; - Diffusion flame extinction limits for MD [139]			125 species; 713 reactions
Sarathy et al. [136]	- Reduced model from Herbinet et al. [46]; - Speciation in diffusion flame for MD [136]			648 species; 2998 reactions
Luo et al. [141]	- Reduction of model from Herbinet et al. [46]; - JSR for rapeseed oil [137]; - Ignition delay for MD [131]			115 species; 460 reactions

One practical application of a kinetic model is to provide chemical and physical information that will allow complicated engine simulations. For this purpose, a compact kinetic model is preferred. Based on previous kinetic modeling processes for MD, a more compact and comprehensive model of MD is developed in this chapter. The development of a detailed mechanism will be discussed in the first section, followed by the reduction procedures, the validations, and the discussion of MD as a surrogate biodiesel fuel.

5.1.1 Detailed mechanism

The generation rules for a detailed MD mechanism mainly follow the 25 reaction classes suggested by Curran et al. [74]. In the publication about the *n*-heptane mechanism [74], 25 reaction classes for high-temperature oxidation (class 1-9) and low-temperature oxidation (class 10-25) are discussed extensively. Due to the presence of a methyl-ester group, the reaction rates relevant to ester groups are applied using the values from Herbinet et al. [46]. For the linear carbon chain (without a methyl-ester group), the reaction rates are mainly based on the study by Ahmed et al. [31]. Thanks to recent experiments and modeling, several updated reaction rates are available, as explained in the following.

To facilitate discussion, the molecular structure of MD and the names for the different carbon positions in current thesis are shown in Figure 5.1. The letter “p” in brackets means primary radical position, “s” means secondary radical position, and “c” means radical position adjacent to a carbonyl radical. The numbers next to the brackets indicate the names for the carbon position, and “m” means the methyl group.

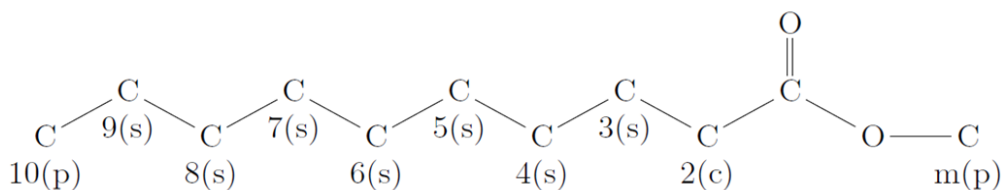


Figure 5.1: Molecular structure of MD

From the analyses of bond dissociation energies shown in Figure 5.2, it can be seen that the carbon in the linear chain (2), next to the carbonyl position, has the lowest C-H bond dissociation energy. Consequently, the reaction rate for the H atom abstraction at this carbon position (2) needs to be faster than that at the secondary carbon positions (3-9); hence the corresponding radical ($C_{11}H_{21}O_2-r2$) generation is faster than that of the secondary radicals. The H atom abstraction reaction rate by hydroxyl radical (OH) is applied from the recent kinetic

data of Sivaramakrishnan and Michael [75]. Using their data improves model predictions in the low temperature range compared to those reported in earlier studies [76, 77]. H atom abstraction reactions by highly oxygenated methane derivatives (O_2CHO) as suggested in the *n*-heptane mechanism [74] are not considered. The values of abstraction reaction rates by radical carriers (other than OH) remain the same as given by Ahmed et al.

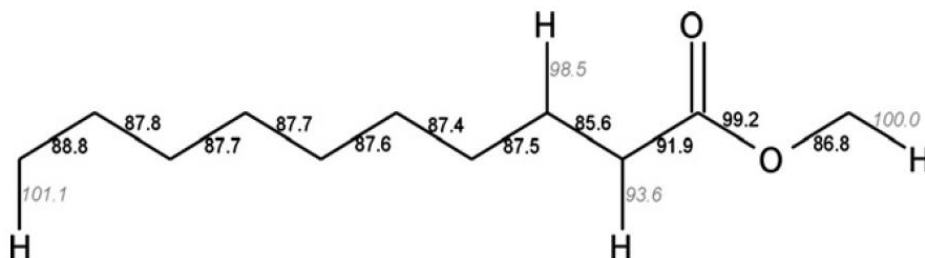


Figure 5.2: Bond dissociation energies (black: C-C bonds; gray, C-H bonds) calculated at 298.15 K for MD (unit: kcal mol⁻¹) [138]

Since the radical $C_{11}H_{21}O_2\text{-r}2$ is easily generated, it further decomposes into a 1-heptyl radical and a methyl propenoate through a β -scission reaction. In Figure 5.2, carbon position (3) and position (4) have the lowest C-C bond energy (85.6 kcal/mol). Therefore, the carbon at position (4) loses its H atom and forms the radical $C_{11}H_{21}O_2\text{-r}4$, which will produce corresponding radicals easier than other radicals due to its lower C-C bond energy. These two β -scission reactions are shown in Figure 5.3. The revised kinetic data for β -scission reactions follow the study of El Bakali et al. [78], but the author made some changes to improve the validation result.

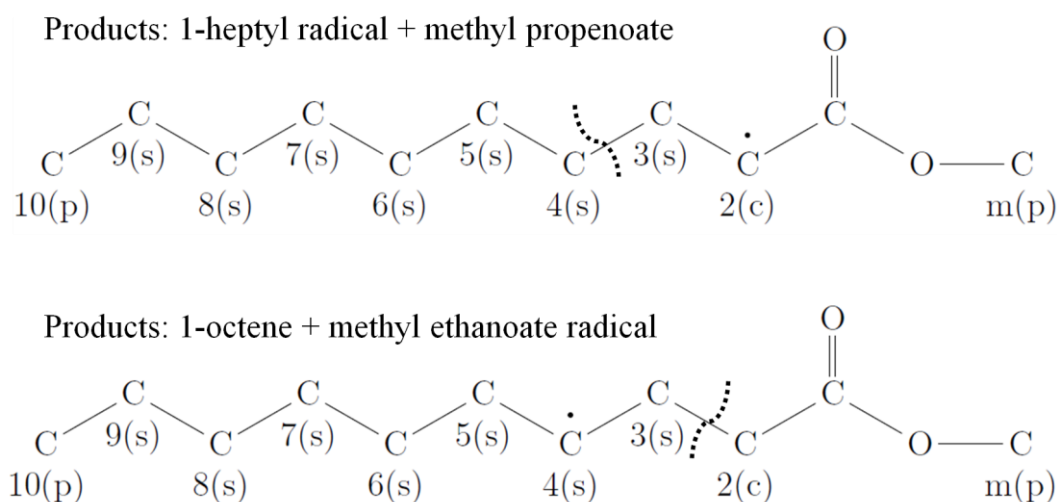


Figure 5.3: β -scission reactions for two MD radicals

The high-temperature oxidation pathway of olefins is applied with detailed rules suggested by Nawdiyal et al. [32] because olefins are one of the most intermediate products. The low-temperature oxidation pathway of olefins is not included here because the low-temperature oxidation pathway is applied only to the seed molecule as explained in this chapter later. The H atom abstraction from olefins (reaction class 6) follows the rules of H abstraction from the fuel molecule (reaction class 2). As the allylic C-H bond and C-C bond have the lowest bond energy, only the rate coefficient at the allylic position given by Mehl et al. [81] is applied as the fastest reaction pathway. Subsequently, the detailed decomposition rules of olefin at the allylic position (reaction class 9) and the decomposition rules of alkenyl radicals (reaction class 8) are used as in Mehl et al. [81].

In low-temperature oxidation, the reaction rate values for isomerization of peroxyalkylhydroperoxide (class 23) are taken from Ahmed et al. [31] but divided by 5, for better agreement with the MD experimental values. The reaction rate values for the rest of the classes remain the same as in Ahmed et al. [31]. The primary oxidation mechanism of MD is listed in Table 5.2.

Table 5.2 Primary oxidation mechanism of MD

Reaction	$A [\frac{cm^3}{mol \cdot s}]$	n	$E_a [\frac{cal}{mol}]$	Ref.
<i>Class 1 : Unimolecular alkane decomposition</i>				
$C_nH_{2n}O_2 = H + C_nH_{2n-1}O_2$	2.5E27	-3.8	9.708E4	[31]
$C_nH_{2n}O_2 = methyl + alkyl\ ester$	1.0E28	-3.8	9.106E4	[31]
$C_nH_{2n}O_2 = alkyl + alkyl\ ester$	1.0E28	-3.8	9.011E4	[31]
<i>Class 2 : H atom abstraction from fuel & class 6 : H atom abstraction from alkenes</i>				
$C_nH_{2n}O_2 + H = C_nH_{2n-1}O_2 + H_2$	Per H			
Primary	5.63E07	2.00	7.706E3	[31]
Secondary	2.45E07	2.00	5.002E3	[31]
Carbonyl	1.26E14	0.00	7.300E3	[74]
$C_nH_{2n}O_2 + OH = C_nH_{2n-1}O_2 + H_2O$				
Primary	4.55E06	1.81	8.683E2	[75] ^a
Secondary	2.86E06	1.81	-1.015E3	[75] ^a
Carbonyl	3.53E09	0.94	5.047E2	[75] ^a
$C_nH_{2n}O_2 + O = C_nH_{2n-1}O_2 + OH$				
Primary	3.66E05	2.40	5.504E3	[31]
Secondary	1.18E05	2.50	2.201E3	[31]
Carbonyl	1.10E13	0.00	3.280E3	[74]
$C_nH_{2n}O_2 + CH_3 = C_nH_{2n-1}O_2 + CH_4$				
Primary	2.17E11	0.00	1.166E4	[31]
Secondary	2.00E11	0.00	9.506E3	[31]
Carbonyl	1.00E11	0.00	7.906E3	[74]
$C_nH_{2n}O_2 + HO_2 = C_nH_{2n-1}O_2 + H_2O_2$				
Primary	2.68E12	0.00	1.965E4	[31]
Secondary	2.44E12	0.00	1.701E3	[31]
Carbonyl	2.16E12	0.00	1.440E4	[74]

(Table continues on next page)

Table 5.2 (continued)

Reaction	$A \left[\frac{\text{cm}^3}{\text{mol} \cdot \text{s}} \right]$	n	$E_a \left[\frac{\text{cal}}{\text{mol}} \right]$	Ref.
<i>Class 2 : H atom abstraction from fuel & class 6 : H atom abstraction from alkenes</i>	Per H			
$C_nH_{2n}O_2 + CH_3O = C_nH_{2n-1}O_2 + CH_3OH$				
Primary	5.27E10	0.00	7.005E3	[31]
Secondary	5.48E11	0.00	5.002E3	[31]
Carbonyl	1.90E10	0.00	2.800E3	[74]
$C_nH_{2n}O_2 + O_2 = C_nH_{2n-1}O_2 + HO_2$				
Primary	4.17E12	0.00	4.902E4	[31]
Secondary	1.00E13	0.00	4.761E4	[31]
Carbonyl	2.00E13	0.00	4.130E4	[74]
$C_nH_{2n}O_2 + C_2H_3 = C_nH_{2n-1}O_2 + C_2H_4$				
Primary	1.67E11	0.00	1.801E4	[31]
Secondary	2.00E11	0.00	1.681E4	[31]
Carbonyl	2.00E11	0.00	1.430E4	[74]
$C_nH_{2n}O_2 + C_2H_5 = C_nH_{2n-1}O_2 + C_2H_6$				
Primary	1.67E10	0.00	1.341E4	[31]
Secondary	2.50E10	0.00	1.041E4	[31]
Carbonyl	1.00E11	0.00	7.900E3	[74]
$C_nH_{2n}O_2 + CH_3O_2 = C_nH_{2n-1}O_2 + CH_3O_2H$				
Primary	2.02E12	0.00	2.044E4	[31]
Secondary	2.02E12	0.00	1.771E4	[31]
Carbonyl	2.00E12	0.00	1.430E4	[74]
$C_nH_{2n}O_2 + C_nH_{2n-1}O_4 = C_nH_{2n-1}O_2 + C_nH_{2n-1}O_2H$				
Primary	2.02E12	0.00	2.044E4	[31]
Secondary	2.02E12	0.00	1.771E4	[31]
Carbonyl	2.00E12	0.00	1.600E4	[74]
<i>Reaction class 3</i>				
$C_nH_{2n-2}O_2 + H = C_nH_{2n-1}O_2$				
H addition on terminal C	1.00E13	0.0	1.200E3	[31]
H addition on internal C	1.00E13	0.0	2.900E3	[31]
to form olefins and alkyl radicals	7.50E18	-2.0	2.880E4	[79] ^b
$C_nH_{2n+1}OCOCH_2-rm = C_nO_2H_{2n+1}CO + CH_2O$	6.30E18	-2.0	3.190E4	[46] ^b
$C_nH_{2n}OCOCH_3-r2 = C_{n-1}H_{2n-1}CHCO + CH_3O$	6.30E18	-2.0	3.220E4	[46] ^b
$C_nH_{2n}OCOCH_3-r3 = C_nH_{2n} + CH_3OCO$	6.00E18	-2.0	3.12E04	[46] ^b
$C_nH_{2n}OCOCH_3-r4 = C_{n-1}H_{2n-2} + CH_2OCOCH_3$	1.60E19	-2.0	2.78E04	[46] ^b
<i>Reaction class 5: $C_nH_{2n-1}O_2 = C_nH_{2n-1}O_2$</i>				
Primary to secondary 3 ring	5.48E08	1.62	3.876E4	[31]
Reverse	1.74E07	2.01	4.128E4	[31]
Primary to secondary 4 ring	1.39E09	0.98	3.376E4	[31]
Reverse	4.41E07	1.38	3.628E4	[31]
Primary to secondary 5 ring	2.54E09	0.35	1.976E4	[31] ^c
Reverse	1.61E08	0.74	2.228E4	[31] ^c
Primary to secondary 6 ring	4.28E11	-1.05	1.176E4	[31]
Reverse	1.36E10	-0.66	1.428E4	[31]
Secondary to secondary 3 ring (2-3)	9.59E08	1.39	3.970E4	[31]
Reverse	9.59E08	1.39	3.970E4	[31]
Secondary to secondary 3 ring (3-4)	6.04E08	1.39	3.970E4	[31]
Reverse	1.20E09	1.39	3.970E4	[31]
Secondary to secondary 4 ring	1.76E09	0.76	3.470E4	[31]
Reverse	3.50E09	0.76	3.470E4	[31]
Secondary to secondary 5 ring	3.22E09	0.13	2.070E4	[31]
Reverse	3.22E09	0.13	2.070E4	[31]
Secondary to secondary 6 ring	5.00E11	-1.25	1.276E4	[71]
Reverse	1.60E10	-0.86	1.528E4	[71]

(Table continues on next page)

Table 5.2 (continued)

Reaction	$A [\frac{cm^3}{mol \cdot s}]$	n	$E_a [\frac{cal}{mol}]$	Ref.
<i>Reaction class 7</i>				
$C_nH_{2n-1}O_2 + H \Rightarrow products$	2.50E12	0.00	1.00E3	[30] ^d
$C_nH_{2n-1}O_2 + OH \Rightarrow products$	5.00E12	0.00	1.00E3	[30] ^d
<i>Reaction class 8</i>				
<i>secondary radicals (to form primary radical)</i>	1.00E14	0.00	3.100E4	[81]
<i>primary radicals (to form primary radical)</i>	1.00E14	0.00	3.000E4	[81]
<i>allyl radicals (to form primary radical)</i>	1.00E13	0.00	3.500E4	[81]
<i>secondary radicals (to form allyl radical)</i>	3.16E13	0.00	2.600E4	[81]
<i>Reaction class 9</i>				
<i>to form methyl radical and alkenyl ester</i>	1.00E16	0.00	7.300E4	[81]
<i>to form alkyl radical and alkenyl ester</i>	1.00E16	0.00	7.100E4	[81]
<i>to form alkenyl radical and alkyl ester</i>	1.00E16	0.00	7.100E4	[81]
<i>Reaction class 10</i>				
$C_nH_{2n-1}O_2 + O_2 = C_nH_{2n-1}O_4$	2.00E12	0.00	0	[31]
<i>Reaction class 11</i>				
$C_nH_{2n-1}O_2 + C_nH_{2n-1}O_4 = C_nH_{2n-1}O_3 + C_nH_{2n-1}O_3$	7.00E12	0.00	-1.000E3	[31]
<i>Reaction class 12</i>				
$C_nH_{2n-1}O_4 = C_nH_{2n-2}O_4H$	Per H			
5 ring primary	2.98E12	0.00	2.970E4	[31]
5 ring secondary	2.98E12	0.00	2.790E4	[31]
5 ring tertiary	2.59E12	0.00	2.540E4	[35]
6 ring primary	2.47E11	0.00	2.390E4	[31]
6 ring secondary	2.48E11	0.00	2.215E4	[31]
6 ring tertiary	2.16E11	0.00	1.970E4	[35]
7 ring primary	2.06E10	0.00	2.110E4	[31]
7 ring secondary	2.06E10	0.00	1.935E4	[31]
7 ring tertiary	1.80E10	0.00	1.640E04	[35]
8 ring primary	1.72E09	0.00	2.390E04	[31]
8 ring secondary	1.72E09	0.00	2.215E04	[31]
8 ring tertiary	1.50E09	0.00	1.970E04	[35]
<i>Reaction class 13,14</i>				
$C_nH_{2n-1}O_4 + HO_2 = C_nH_{2n-1}O_4H + O_2$	1.75E10	0.00	-3.272E3	[31]
$C_nH_{2n-1}O_4 + H_2O_2 = C_nH_{2n-1}O_4H + HO_2$				
forward reaction	2.40E12	0.00	1.000E4	[74]
reverse reaction	2.40E12	0.00	1.000E4	[74]
<i>Reaction class 15, 16</i>				
$C_nH_{2n-1}O_4 + CH_3O_2 \Rightarrow C_nH_{2n-1}O_3 + CH_3O + O_2$	1.40E16	-1.61	1.857E3	[31]
$C_nH_{2n-1}O_4 + C_nH_{2n-1}O_4 \Rightarrow$				
$C_nH_{2n-1}O_3 + C_nH_{2n-1}O_3 + O_2$	1.40E16	-1.61	1.857E3	[31]
<i>Reaction class 17</i>				
$C_nH_{2n-1}O_4H = C_nH_{2n-1}O_3 + OH$	1.26E16	0.00	4.246E4	[31]
<i>Reaction class 18</i>				
$product1 + product2 + product3 = C_nH_{2n-1}O_3$	1.00E11	0.00	1.189E4	[31]
<i>Reaction class 19</i>				
<i>cyclic ether 3 ring</i>	3.00E11	0.00	2.198E4	[31]
<i>cyclic ether 4 ring</i>	2.50E10	0.00	1.524E4	[31]
<i>cyclic ether 5 ring</i>	2.08E09	0.00	6.500E3	[31]
<i>cyclic ether 6 ring</i>	1.50E08	0.00	1.800E3	[31]
<i>Reaction class 20</i>				
$C_nH_{2n-2}O_2 + HO_2 = C_nH_{2n-2}O_4H$				
addition on terminal position	1.00E11	0.00	1.101E4	[31]
addition on internal position	1.00E11	0.00	7.605E3	[31]

(Table continues on next page)

Table 5.2 (continued)

Reaction	$A [\frac{cm^3}{mol \cdot s}]$	n	$E_a [\frac{cal}{mol}]$	Ref.
Reaction class 21 $C_nH_{2n-2}O_4H \Rightarrow C_mH_{2m} + \text{carbonyl} + OH$	5.00E13	0.00	2.548E4	[31]
Reaction class 22 $C_nH_{2n-2}O_4H + O_2 = O_2C_nH_{2n-2}O_4H$	2.00E12	0.00	0	[31]
Reaction class 23 $O_2C_nH_{2n-2}O_4H = OC_nH_{2n-3}O_3H + OH$	Per H			
5 ring primary	5.96E11	0.00	2.668E4	[31] ^e
5 ring secondary	2.98E11	0.00	2.488E4	[31] ^e
6 ring primary	2.48E10	0.00	2.088E4	[31] ^e
6 ring secondary	1.12E10	0.00	1.913E4	[31] ^e
7 ring primary	4.12E9	0.00	1.808E4	[31] ^e
7 ring secondary	2.06E9	0.00	1.633E4	[31] ^e
8 ring primary	3.44E09	0.00	2.088E4	[31] ^e
8 ring secondary	1.72E08	0.00	1.913E4	[31] ^e
Reaction class 24 $OC_nH_{2n-3}O_3H = \text{products} + OH$	1.00E16	0.00	4.16E4	[31]
Reaction class 25 $C_nH_{2n-2}O_3 + OH = \text{products} + H_2O$				
H - C - O primary	9.50E07	1.61	-3.500E1	[31]
H - C - O secondary	8.84E09	1.00	-1.482E2	[31]
$C_nH_{2n-2}O_3 + HO_2 = \text{products} + H_2O_2$				
H - C - O primary	3.00E04	2.60	1.390E4	[31]
H - C - O secondary	1.08E04	2.55	1.053E4	[31] ^b

The rate constant, $k = A * T^n * \exp(-E_a/RT)$ are given in the units of $s^{-1}, cm^3, mol^{-1}, cal$.

^a The pre-exponential factor here is doubled for the value from Atkinson et al. [75].

^b The pre-exponential factor here is modified for the value from Allara et al. [79]

^c The rate constant here is taken from the corrected table from Ahmed et al. [31].

^d The pre-exponential factor here is divided with 2 for the value from Schenk et al. [30]

^e The pre-exponential factor here is divided with 5 for the value from Ahmed et al. [31]

In the low-temperature region, the author applied the low-temperature oxidation pathway (class 10-25) only to the seed molecule of the mechanism (MD here), unlike in the *n*-heptane mechanism of Curran et al. [74]. In this way, the detailed mechanism is already quite compact. Using C₀-C₆ chemistry (base chemistry), the author derived a comprehensive, detailed model with 619 species and 3600 reversible reactions of a size that is not only significantly smaller than the LLNL model [46] (with 2877 species), but also comparable to recently published skeletal mechanisms [136] (with 648 species).

5.1.2 Chemistry-guided reduction (CGR)

The precondition for reduction is a starting mechanism that is extensively validated for the whole range of combustion conditions while being of compact size at the same time. As

the starting mechanism was already introduced in the previous section, this section focuses on the application of chemical lumping combined with sensitivity analysis.

“Chemical lumping” means that a set of isomeric species are replaced by single lumped species based on chemical properties such as different functionalities. In the past, chemical lumping was applied for the reduction of *n*-heptane based on the two rules listed in Table 5.3. The first rule organizes the functional groups and radical sites. The low-temperature oxidation of MD, which is similar to that of the *n*-alkane mechanisms, is dominated by the isomerization reactions starting with ten different C₁₀H₂₁O₂ isomers. These isomers are distinguished depending on the carbon atom hosting the functional groups into primary, secondary, or carbonyl. Taking *n*-heptane as an example, all secondary heptyl isomers that have equal concentrations can be lumped as one lumped isomer. However, MD has an asymmetrical molecular structure. Secondary carbons have different bond energies and hence obtain different concentrations, so they cannot be lumped together. Therefore, the rules should consider the same bond energy as another criterion, and hence an updated version of the rules is listed in Table 5.4. According to the analysis of carbon bond energy, C₁₀H₂₁O₂-r2 and C₁₀H₂₁O₂-r4 are special isomers that should not be lumped. The other six secondary isomers are lumped as one lumped isomer. With the lumping approach, the structure of low-temperature oxidation is simplified as depicted in Figure 5.4.

Table 5.3 Original chemical lumping rules and assumptions

No.	Rules	Assumptions used for the lumping	Classes
1	Species with the same functional groups at the same sites are lumped separately.	Species with the same functional group at the same sites have equal concentrations.	1 to 11 & 13 to 18
2	Species with the same functional groups at the same sites and with the same number of C atoms between the functions are lumped separately.	Species with the same functional groups at the same sites and with the same number of C atoms between the functions have equal concentrations.	12 & 19 to 24

Table 5.4 Chemical lumping rules and assumptions (updated in current study)

No.	Rules	Assumptions used for the lumping	Classes
1	Species with the similar C-H and C-C bond energies are lumped separately.	Species with the similar C-H and C-C bond energies have equal concentrations.	1 to 11 & 13 to 18
2	Species with the similar C-H and C-C bond energies and with the same number of C atoms between	Species with the similar C-H and C-C bond energies and with the same number of C atoms between	12 & 19 to 24

	the functions are lumped separately.	the functions have equal concentrations.	
--	--------------------------------------	--	--

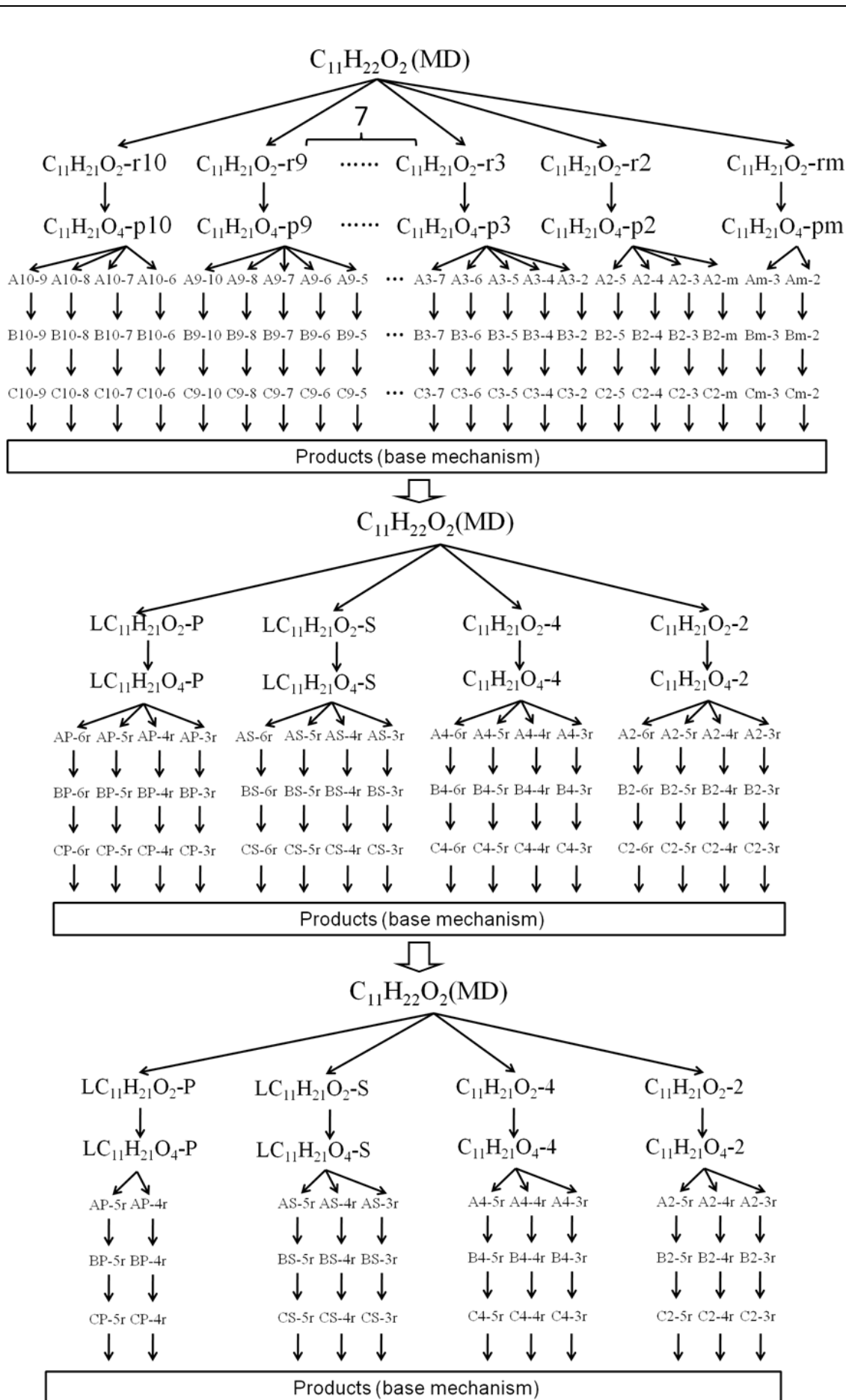


Figure 5.4: Simplified oxidation pathway of MD in the low-temperature region

The second rule organizes the distance between functional groups. 56 hydroperoxical radicals (in class 12) are lumped into 16 lumped radicals, which are correspondingly distinguished as primary, secondary, and two non-lumped hydroperoxical radicals in Table 5.5. With such a tremendously reduced number of species, the deviations are found to be negligible when comparing the aggregated concentration profiles of the lumped species and the corresponding isomers in the detailed mechanism. The detailed mathematical description of the lumping procedure is given by Zeuch et al. [43].

Table 5.5 Structure simplification of detailed, lumped, and skeletal mechanisms visualized by the isomer number used for each reaction step (Figure 5.5)

Reaction Step	Number of Isomeric Species		
	Detailed	Lumped	Skeletal
1	10	4	4
2	10	4	4
2a	10	4	0
3	56	16	11
3a	28	4	3
3b	8	3	3
4	56	16	11
5	56	16	11

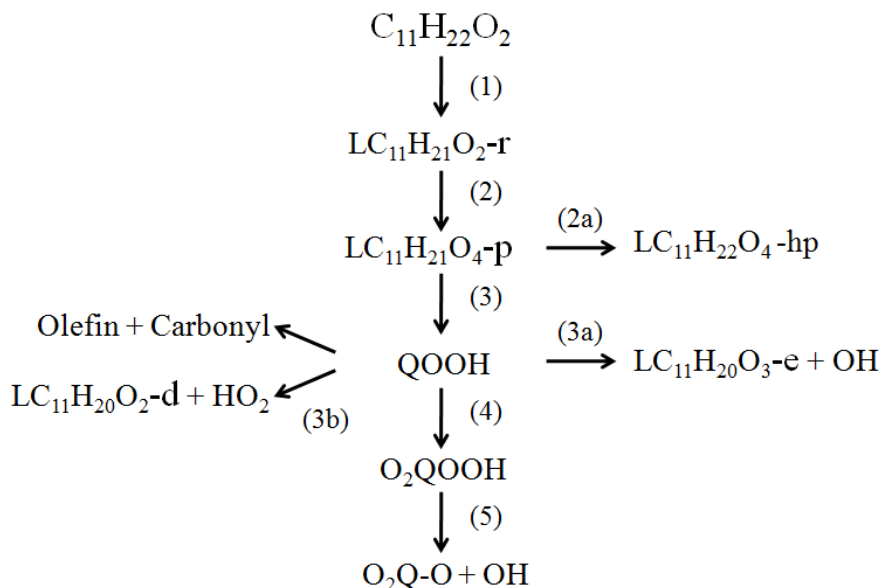


Figure 5.5: Schematic diagram of main oxidation pathways

The lumped mechanism generated according to this procedure consists of 419 species and 3500 reversible reactions, as compared to 619 species and 3600 reversible reactions for the detailed mechanism.

In the next step, the lumped mechanism can be further simplified into a skeletal mechanism by species removal using the necessity analysis tool developed by Soyhan et al. [40]. The automatic detection of species with low necessity is done by means of reaction flow analysis of the species involved as reactants in sensitive reactions, the fuel, the oxidizer, and the final products. Prior to the reduction, some parameters have to be set, which can be done in two steps as follows:

- First step: The necessary species are defined, such as fuels ($C_{11}H_{22}O_2$), oxidizer (O_2), final major products and important intermediate molecules (H_2 , CO , CO_2 , H_2O , CH_3 , and CH), inert gases (N_2 , Ar).
- Second step: The temperature is chosen as a target for the sensitivity analysis.

The necessity analysis was performed with a wide range of pressures from 1 to 100 bar, temperatures from 600 to 1800 K, and fuel equivalence ratios from 0.1 to 3.5 in a constant volume reactor. Except for the case of the constant volume reactor, the direct test calculations were performed under the experimental conditions used for the validation of the detailed model: fuel consumption in a stoichiometric diluted fuel-oxidizer mixture in a jet-stirred reactor at 1 bar.

For the reduction of the oxidation mechanism for MD, the redundant species with the lowest necessity values were identified, which are mainly from the low-temperature mechanism. If the unimportant seed species are removed, their corresponding products can also be removed safely. For example, if the 8-ring peroxy hydroperoxy radicals can be removed with low necessity values, a set of species produced from the 8-ring peroxy hydroperoxy radicals alone may also be removed safely despite their necessity rankings, such as the methyl-octanoate ketone radical ($C_9H_{15}O_3MO-A_5R_8$), the methyl-heptanoate ketone radical ($C_8H_{13}O_3MHP-A_4R_7$), the methyl-hexanoate ketone radical ($C_7H_{11}O_3MHX-A_3R_6$), and the methyl-pentanoate ketone radical ($C_6H_9O_3MPE-A_2R_5$). In this way, all possible redundant species will not be neglected. The characteristic properties of the detailed, lumped, and skeletal mechanisms in the low-temperature region are quantified by the numbers of isomers used in each reaction step as shown in Table 5.5.

In the high-temperature mechanism, olefins and the corresponding alkenyl radicals are the main intermediate species. The olefins with double bonds at their secondary positions generally have much lower necessities than those with double bonds at their primary positions. This finding is confirmed by the study of Glaude et al. [135], who demonstrated that the most abundant olefins obtained from linear alkanes are those with double bonds located at

their primary positions, exclusively obtained by β -scission of normal alkyl radicals. In addition, small olefins show higher importance than large olefins.

The C₀-C₆ chemistry reduction follows the reduction of the *n*-heptane/toluene mechanism [28], in which the C₀-C₆ chemistry developed from the model of Warnatz and colleagues has been preserved almost completely. The final skeletal mechanism, which was validated over the total parameter range discussed in current study, consists of 244 species and 3000 reversible reactions.

5.2 Mechanism validations for MD

Table 5.6 summarizes the validations and analyses of using MD as fuel; their detailed description will be discussed below.

Table 5.6 Validations and analyses of MD performed in current thesis

	Conditions			Authors
	T [K]	p [atm]	Mixtures	
Ignition delay	650-1400	15-16	$\phi = 0.5-1.5$ in air	Wang et al.
Ignition delay	1200-1350	8	$\phi = 0.09$ in Ar	Haylett et al.
Ignition delay	700-1300	20	$\phi = 1$ in air	Wang et al.
Ignition delay	900-1300	20;50	$\phi = 1$ in air	Li et al.
Ignition delay	1050-1400	7	$\phi = 0.3; 1.4$ in Ar	Campbell et al.
Flame speed	403	1	$\phi = 0.6-1.4$ in air	Wang et al.
Speciation in JSR	550-1150	1.06	$\phi = 1.0$ in air	Glaude et al.
Speciation in diffusion flame	420-1700	1	1.8% MD in N ₂ ; 42% O ₂ in N ₂	Sarathy et al.
Sensitivity analysis under const. volume reactor	650, 800, 1000	16	$\phi = 1$ in air	-
Sensitivity analysis under JSR reactor	650, 800, 1000	16	$\phi = 1$ in air	-
Flow analysis under const. volume reactor	800	10	$\phi = 1$ in air	-

5.2.1 Ignition delay times

The auto-ignition of MD has been studied at medium and high-temperatures in shock tube experiments. Wang et al. [131] measured the ignition delay times of MD/air mixtures for $\phi = 0.5, 1.0,$ and 1.5 at pressures around 16 atm. The experimental data are compared with the calculations in the detailed and skeletal mechanisms and are shown in Figure 5.6.

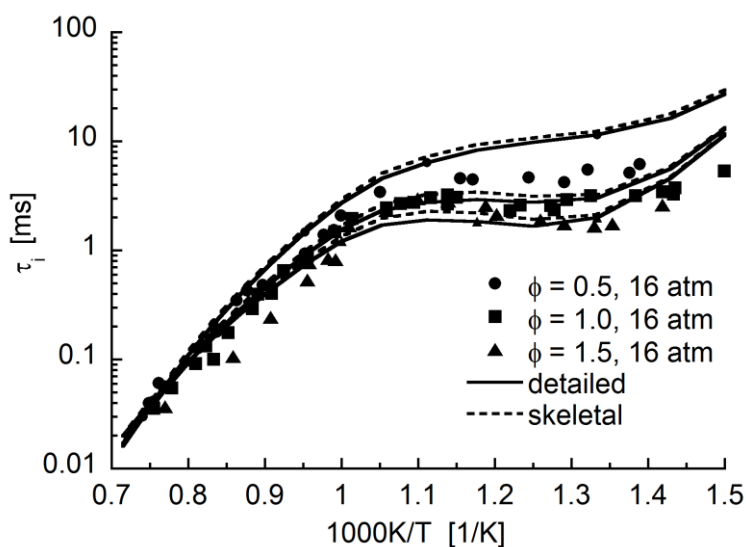


Figure 5.6: Simulated (solid lines: detailed mechanism, dashed lines: skeletal mechanism) and experimental (symbols) ignition delays of MD/air mixtures at 16 atm [131]

The predicted ignition delay times are determined by evaluating the OH emission peak in accordance with the procedure applied in the experiments. Agreement is good for stoichiometric and fuel-rich conditions. For fuel-lean conditions with $\phi = 0.5$, there is a deviation in the low-temperature region. This feature is also found in the model of Grana et al. [140]. The other models [46, 135] have better agreement for fuel-lean conditions, but have over-predictions in the low-temperature region for fuel-rich and stoichiometric conditions.

Reaction sensitivity coefficients that show the rate limiting reaction are especially valuable for demonstrating the accuracy of the reduction [12]. Reaction sensitivity analyses at 650, 800, and 1000 K were performed for both the detailed and the skeletal mechanism as shown in Figure 5.7. As the author's attention was focused on MD oxidation kinetics at low-temperatures, it was assumed that only those reactions belonging to reaction classes 1–25 are of major importance for the reactivity at low- and medium temperatures. The author multiplied the forward rate coefficients of these reactions by a factor of two and compared the relative change in the ignition delay times. A negative sensitivity coefficient thus means that the overall rate of fuel oxidation is enhanced by the examined reaction. The sensitivity coefficients were calculated at the same temperatures as done by Curran et al. [74]. The relative sensitivities here are unchanged when comparing the detailed mechanism with the skeletal one as displayed in Figure 5.7. The author related this finding to the almost completely preserved C_0 - C_6 chemistry, which effectively determines the reactivity when smaller species are formed in the fuel degradation and oxidation process. Removing the species with the lowest necessity values does not change the relative and absolute amounts of the reactive C_1/C_2 species formed, hence reaction class sensitivities are largely unaffected.

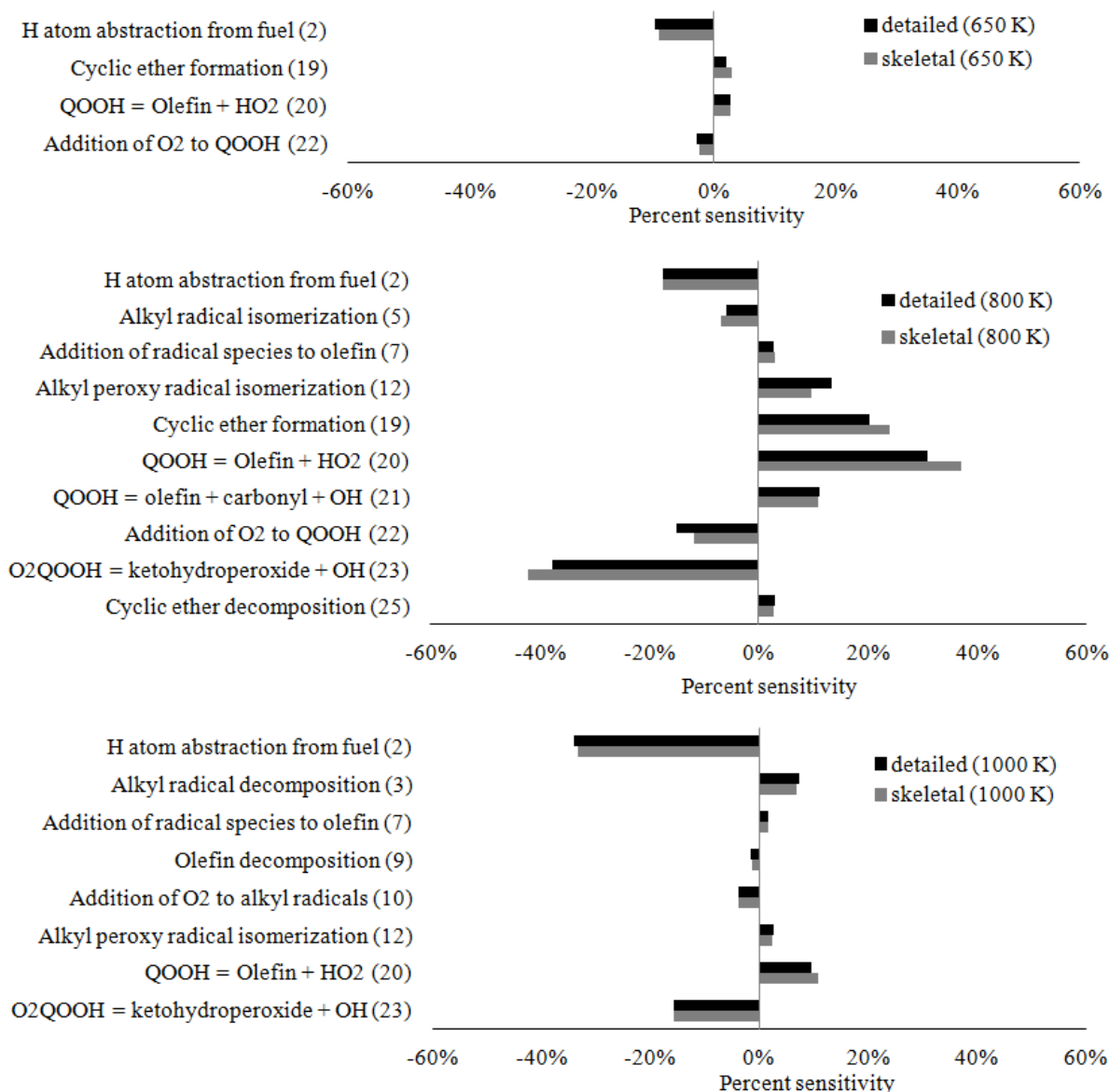


Figure 5.7: Sensitivity coefficients for ignition delays, stoichiometric MD/air mixtures at 16 atm with 650 K, 800 K, and 1000 K

In order to understand the decomposition process in the negative temperature coefficient (NTC) region, reaction flow analysis was applied here. The reaction flow analyses were performed with both the detailed and the skeletal mechanism and were used to test whether the main decomposition pathway was changed during CGR reduction.

Since MD has ten $C_{11}H_{21}O_2$ isomers, its decomposition flow is of huge size, which cannot be shown in one normal size picture. Therefore, the consumption flow of one MD radical ($C_{11}H_{21}O_2-r3$) was selected to show the general decomposition process. The reason for the selection of $C_{11}H_{21}O_2-r3$ is that $C_{11}H_{21}O_2-r3$ is a normal secondary fuel radical that was lumped with other normal secondary radicals during CGR reduction. In this way, the comparison of the flow analyses of the detailed and the skeletal mechanism clearly shows the influ-

ence of CGR reduction. Additionally, $C_{11}H_{21}O_2-r3$ is located between two special secondary radicals ($C_{11}H_{21}O_2-r2$ and $C_{11}H_{21}O_2-r4$), and these two species are not lumped as explained in the last section. The investigation of the flow analysis of $C_{11}H_{21}O_2-r3$ may also include detailed information about the interaction between lumped species and un-lumped species.

The integrated carbon flow analysis was performed with stoichiometric MD/air mixtures at 10 bar and 800 K in the shock tube with ignition delay times as shown in Figure 4.8. The numbers represent the integrated carbon flow [mole/cm³] and the percentages in brackets are the percentages of these flows divided by the total consumption flows of the reactant species. The flow and percentage numbers of the detailed mechanism are depicted in black and those of the skeletal mechanism in dark gray.

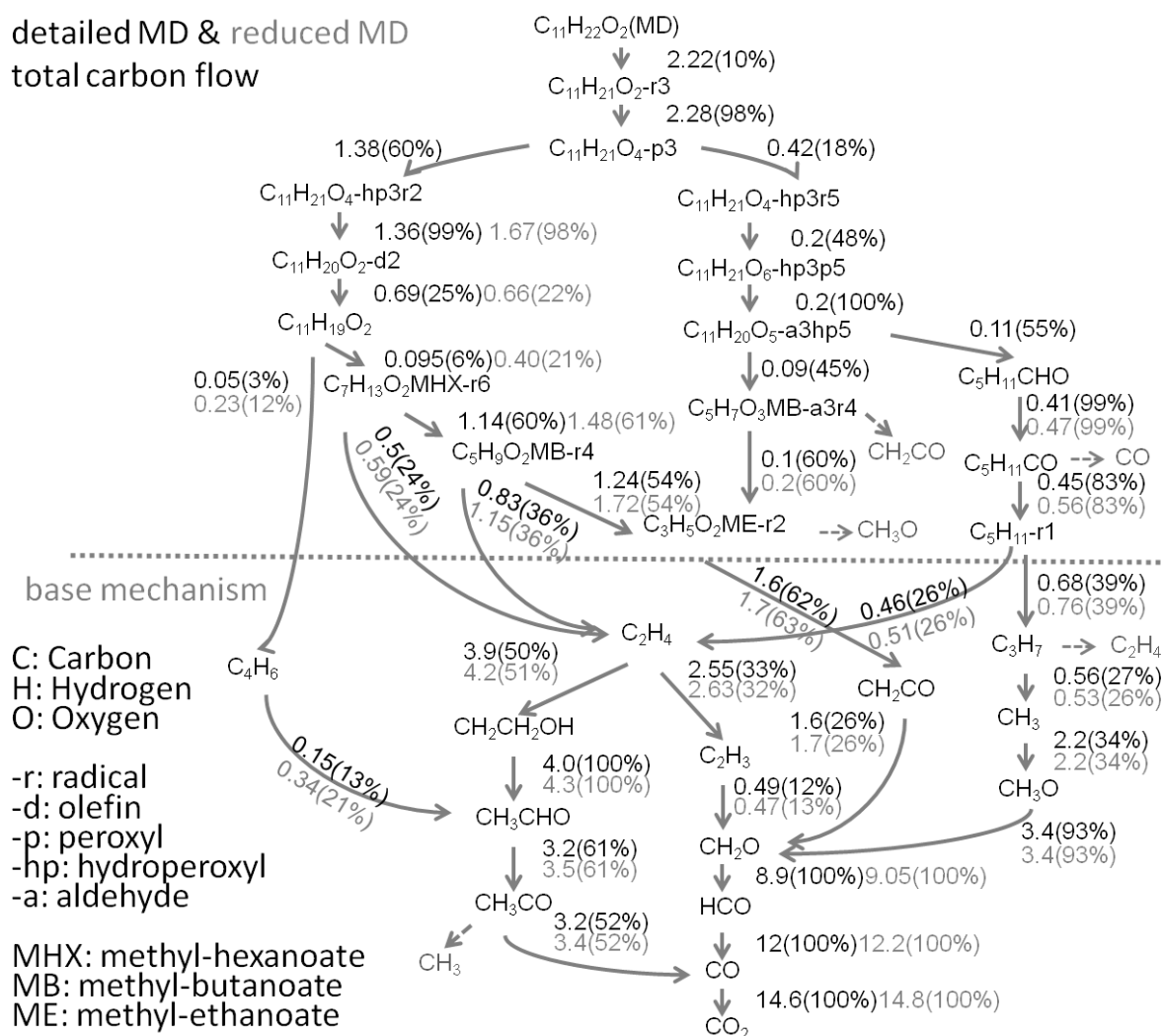


Figure 5.8: Carbon flow analysis for the radical ($C_{11}H_{21}O_2-r3$) for ignition delays, stoichiometric MD/air mixtures at 10 atm and 800 K

Figure 5.8 shows the complete carbon reaction pathway from the fuel (MD) to the final product (CO_2) through varied intermediate species. Since $C_{11}H_{21}O_2-r3$ and other relevant

products are lumped in the skeletal mechanism, they cannot be compared with the detailed species in the detailed mechanism. Along the decomposition pathways from intermediate species to final product (CO_2), there is good agreement between the detailed and the skeletal mechanism except in the decomposition pathway for alkenyl radicals ($\text{C}_{11}\text{H}_{19}\text{O}_2$). In the detailed mechanism, the alkenyl radical ($\text{C}_{11}\text{H}_{19}\text{O}_2$) has different products due to the breakage of the C-C bond at different positions. During the CGR reduction, most products of the alkenyl radicals ($\text{C}_{11}\text{H}_{19}\text{O}_2$) are removed and C_4H_6 and $\text{C}_7\text{H}_{13}\text{O}_2$ MHX-r6 alone are kept. Consequently, the consumption path of $\text{C}_{11}\text{H}_{19}\text{O}_2$ has different flow values and percentage numbers in the detailed and in the skeletal mechanism. For both mechanisms, ethene is the central intermediate species since ethene is the main product derived from all β -scission reactions. Additionally, formaldehyde (CH_2O), aldehyde (HCO), and carbon monoxide (CO) are important intermediate species that produce final products (CO_2) in the oxidation stage.

Recently, the experimental ignition delay times of stoichiometric MD/air mixtures in the shock tube were investigated at higher pressures: at 20 atm by Wang et al. [132] and at 20 and 50 atm by Li et al. [133]. The simulated ignition delay times are compared with the experimental data in Figure 5.9 and Figure 5.10. There is good agreement between the experimental values and the simulated values for both detailed and skeletal mechanism.

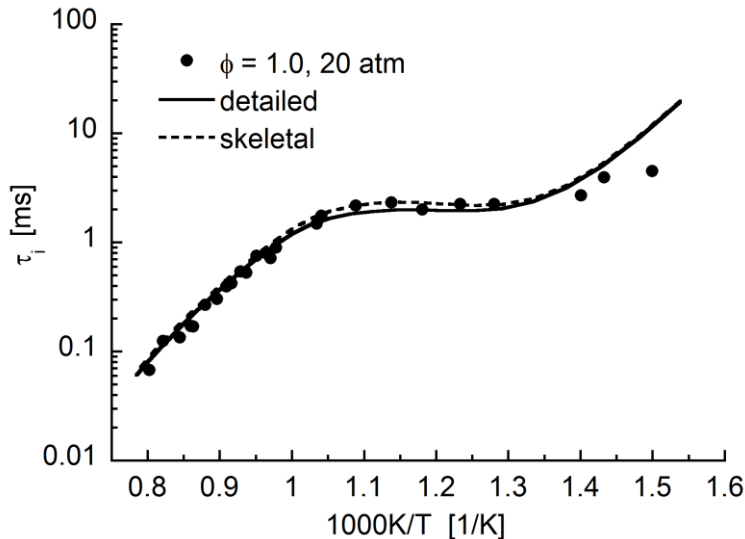


Figure 5.9: Simulated (solid lines: detailed mechanism, dashed lines: skeletal mechanism) and experimental (symbols) ignition delays of MD/air mixtures at 20 atm [132]

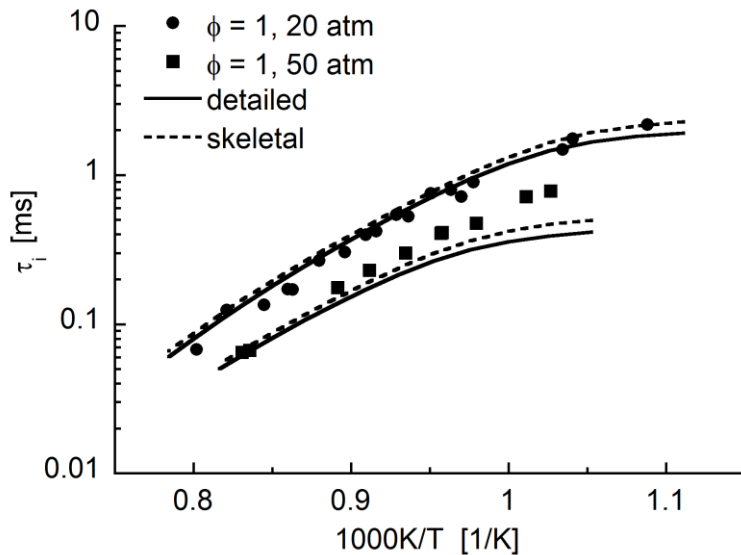


Figure 5.10: Simulated (solid lines: detailed mechanism, dashed lines: skeletal mechanism) and experimental (symbols) ignition delays of MD/air mixtures at 20 and 50 atm [133]

Campbell et al. [134] performed an experiment with ignition delay times for MD at low pressure (7 atm). Acceptable agreement can be seen in the comparison of the simulated values as plotted in Figure 5.11.

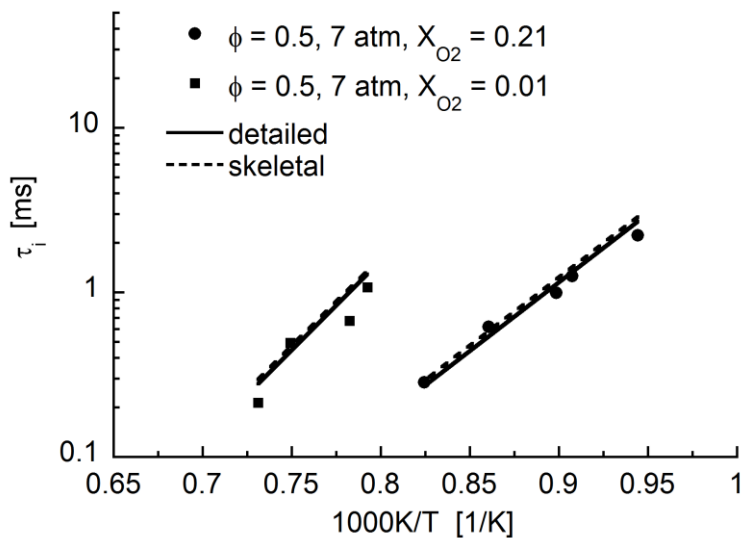


Figure 5.11: Simulated (solid lines: detailed mechanism, dashed lines: skeletal mechanism) and experimental (symbols) ignition delays of MD/O₂/Ar mixtures at 7 atm [134]

Recently, Haylett et al. [53] demonstrated the potential of aerosol shock tubes while investigating ignition delay times for different low-vapor-pressure fuels. MD has low vapor pressure (37 mtorr), and hence it is a good candidate for measurements in the aerosol shock tube. Figure 5.12 shows the comparisons of the measured and the predicted ignition delay times of MD/O₂ mixtures in Ar at a low equivalence ratio ($\phi = 0.17$), 8 atm. The model now under-predicts the ignition delay times by a factor of two in the measured conditions. In order

to balance the ignition delay times reported by Wang et al. [131], the model maintains a reasonable compromise between the two sets of experiments.

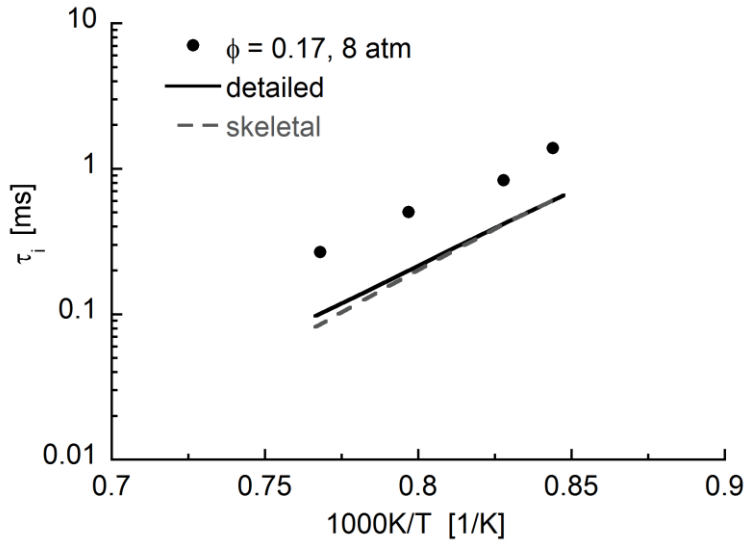


Figure 5.12: Simulated (solid lines: detailed mechanism, dashed lines: skeletal mechanism) and experimental (symbols) ignition delays of MD/O₂/Ar mixtures at 7 atm [53]

5.2.2 Laminar flame speeds

Wang et al. [57] examined the laminar burning velocity of MD/air mixtures at atmospheric pressure and an initial temperature of 403 K in a counter-flow burner. The simulations using the detailed and the skeletal mechanism agree with the experimental data with different fuel/air equivalence ratios and are shown in Figure 5.13.

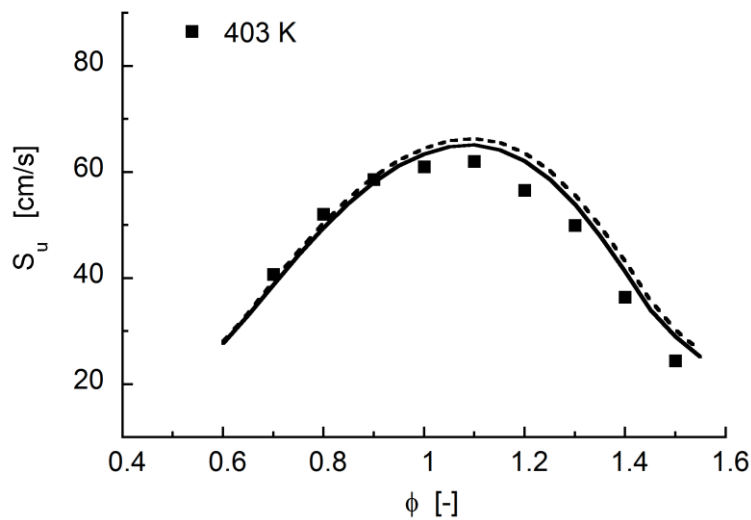


Figure 5.13: Simulated (solid lines: detailed mechanism, dashed lines: skeletal mechanism) and experimental (symbols) laminar flame velocity of MD/air mixtures at 403 K, 1 atm [57]

5.2.3 Jet stirred reactor

Glaude et al. [135] studied the oxidation of MD/O₂/He (helium) mixtures in a JSR at atmospheric pressure and temperatures from 500 to 1100 K. The simulated and experimental species profiles are summarized in Figure 5.14. For the simulations, the inert gas helium was replaced by argon since helium is not included in the reaction mechanism. The mole profile of the fuel is under-predicted, which is consistent with the over-prediction of O₂. The mole fractions of the major species CO, CO₂ are well predicted. The prediction of the mole fractions of C₂H₂, C₂H₆, 1,3-C₄H₆, C₃H₆, and C₃H₈ are acceptable. The predicted mole fractions of large 1-olefins (1-hexene and 1-nonene) and unsaturated esters with double bonds at the end of the chain (methyl 2-propenoate, methyl 3-butenate, methyl 5-hexenoate, methyl 6-heptanoate, methyl 7-octenoate, and methyl 8-nonenoate) are in agreement with the experimental data.

Compared with the simulations using the detailed and the skeletal mechanism, the mole fractions of most species are preserved. The skeletal mechanism shows only negligible deviations from the detailed one. The olefin concentrations predicted by the skeletal mechanism deviate significantly from those of the detailed one. The main reason for this is due to the removal of a large amount of olefin during the reduction. Therefore, the pathways of the remaining olefins are rearranged and their mole fractions are increased to maintain the total amount.

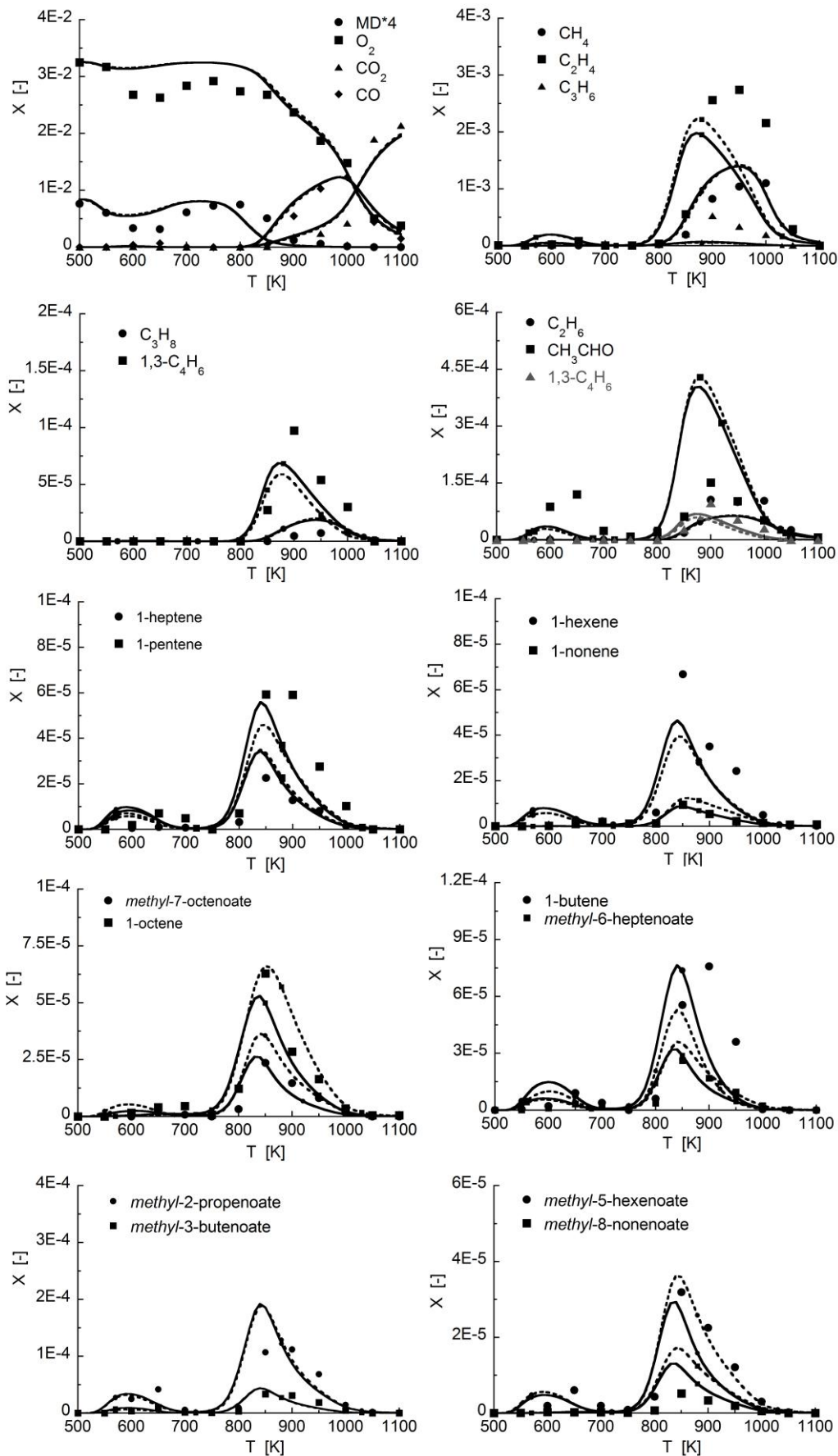


Figure 5.14: Simulated (solid lines: detailed mechanism, dashed lines: skeletal mechanism) and experimental (symbols) species mole fraction in JSR ($C_{11}H_{22}O_2 = 0.21\%$; $O_2 = 3.255\%$; $Ar = 96.535\%$ with $\tau = 1.5$ s at 1.06 bar) [135]

A sensitivity analysis was performed for the stoichiometric MD/air mixtures at temperatures of 600, 730, and 900 K with respect to the 25 reaction classes of the MD model. For the specific conditions of the jet stirred reactor, the sensitivity coefficients were derived in the following way: The steady state concentrations of the fuel in the out stream were calculated using both the original and the modified mechanism, with the rate of a reaction class being enhanced by a factor of two. The ratio of the two concentrations in percentage was defined as the sensitivity coefficient. The results of the sensitivity analysis are displayed in Figure 5.15. It can be observed that the removal of species of low necessity values and their corresponding reactions does not change the relative and absolute class sensitivities.

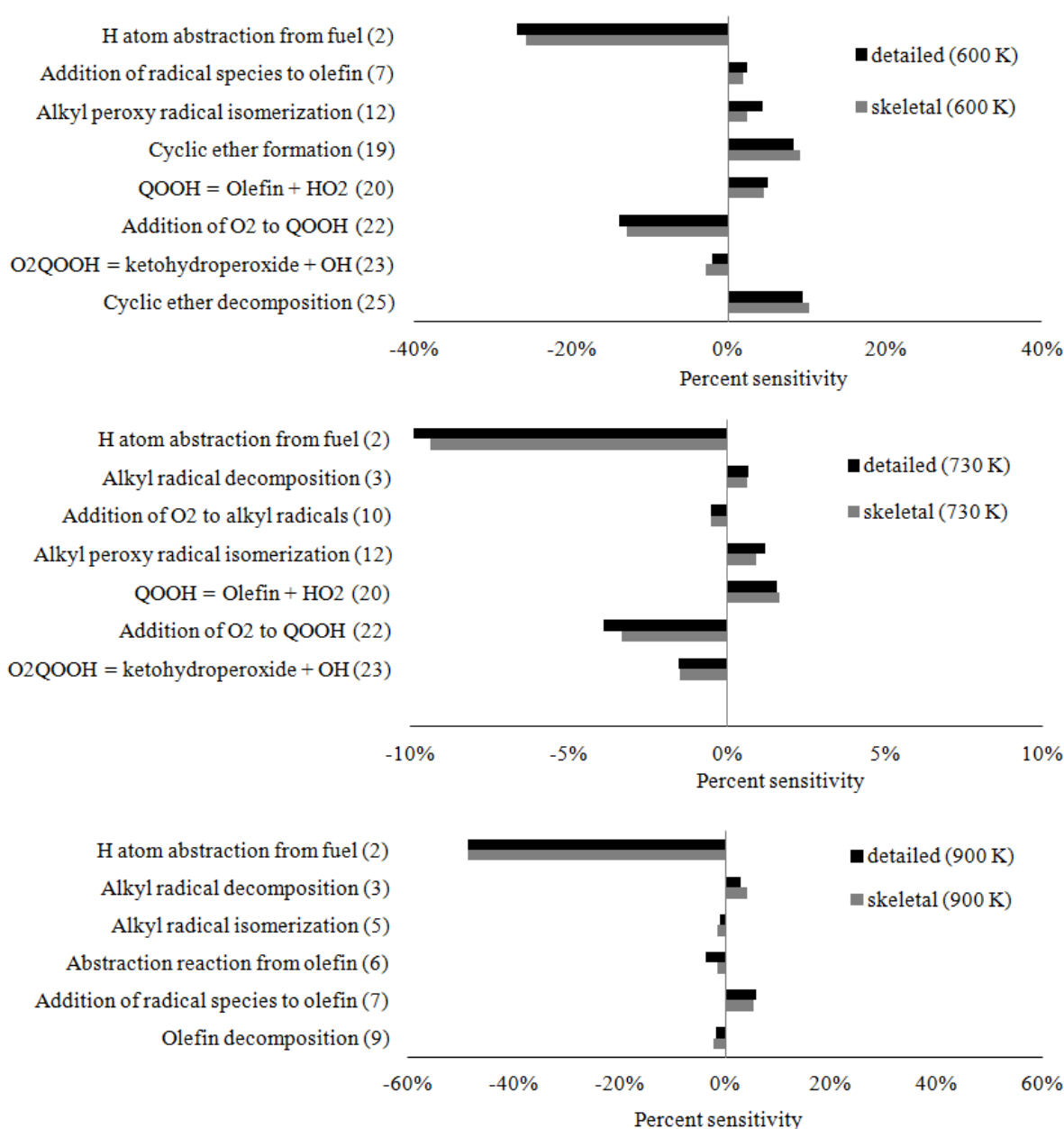


Figure 5.15: Sensitivity coefficients for JSR with stoichiometric MD/air mixtures at 1.06 bar with 600, 730, and 900 K

5.2.4 Diffusion flame speciation

Sarathy et al. [136] studied the specification data of a 1.8% MD, 42% O₂ and 56.2% N₂ diffusion flame at atmospheric pressure. The simulated results are shown in Figure 5.16.

The model performs well in predicting the maximum concentrations of MD, O₂, CO, CO₂, CH₄, C₂H₆, and C₂H₂ which are within a factor of 1.5 of the measured maximal mole fractions. The detected olefins (C₂H₄, C₃H₆, and C₄H₈₋₁) are moderately under-predicted, which is consistent with the simulations performed by Sarathy et al. [35]. The similarity of the simulations also includes the over-prediction of CH₂O, which may result from both experiment deviation and imprecise rate coefficients, as explained by Sarathy et al. [35]. In this mechanism, C₃H₄, C₄H₆₋₁₃, and CH₂CO are over-predicted as well. The model predicts similar mole fractions for C₆H₁₂₋₁ and C₇H₁₄₋₁, while the experimental data show obvious differences.

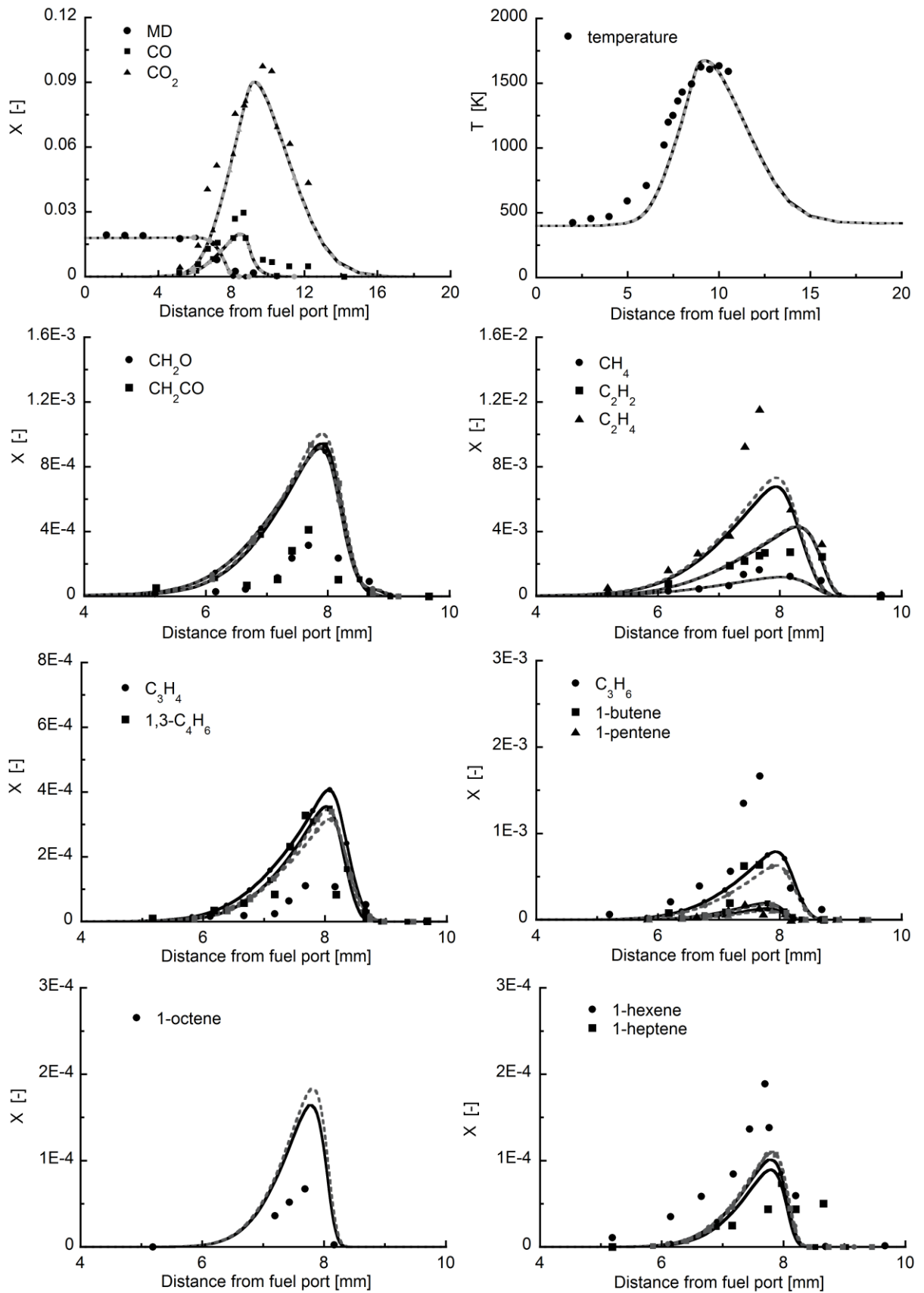


Figure 5.16: Simulated (solid lines: detailed mechanism, dashed lines: skeletal mechanism) and experimental (symbols) species mole fraction in a diffusion flame at atmospheric pressure [136]

5.2.5 Base mechanism

As explained in chapter 3, one feature of current kinetic models is compiled using a well-validated base mechanism. A variety of small-species target fuels are validated using the detailed and the skeletal mechanisms. The experimental ignition delay times for methane [142], ethylene [143], methane/ethane [144], ethane [145], *n*-propane [146], and *n*-butane [146] are well reproduced by the calculations as shown in Figure 5.17. It is noticeable that the simulations predicted by the detailed mechanism (dark straight lines) coincide with the values predicted by the skeletal mechanism (dashed gray lines).

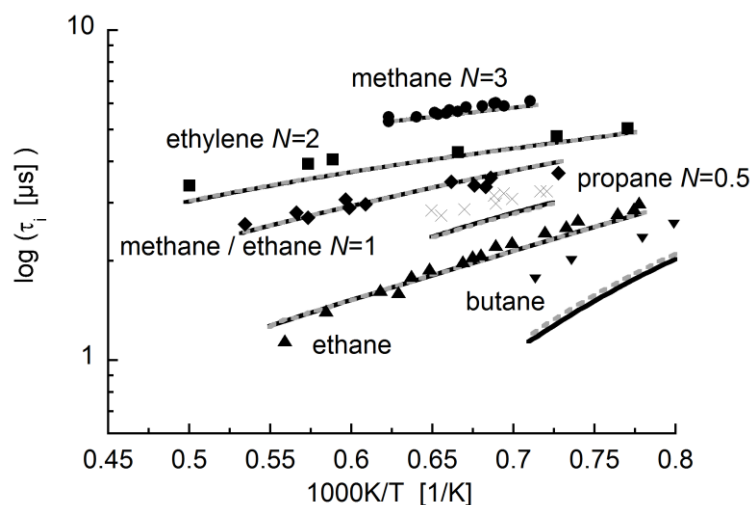


Figure 5.17: Simulated ignition delays, offset by N log units. Mixture compositions and pressure experiments: 9.5% CH_4 , 19% O_2 in Ar, 2.5 bar [142]; 1% C_2H_4 , 1.5% O_2 in Ar, 3 bar [143]; 3.5% CH_4 , 0.164% C_2H_6 , 7% O_2 in Ar, 8 bar [144]; 1% C_2H_6 , 3.5% O_2 in Ar, 2 bar [145]; 0.84% C_3H_8 , 2.1% O_2 in Ar, 7.5 bar [146]; 2.5% C_4H_{10} , 16.25% O_2 in Ar, 10 bar [146]

The experimental laminar flame speeds of methane [147, 148], ethane [149], ethylene [150], *n*-propane [151, 152], propene [153], and *n*-butane [149, 150] are compared with the simulations using the detailed and the skeletal mechanisms in Figure 5.18. There is agreement between the predicted and the experimental flame speeds. The simulations using the detailed mechanism fit with those using the skeletal mechanism for methane, ethane, butane, and ethylene. In the case of the flame speeds of propane and propene, the simulated values obtained when using the skeletal mechanism are slightly higher than the results obtained when using the detailed mechanism.

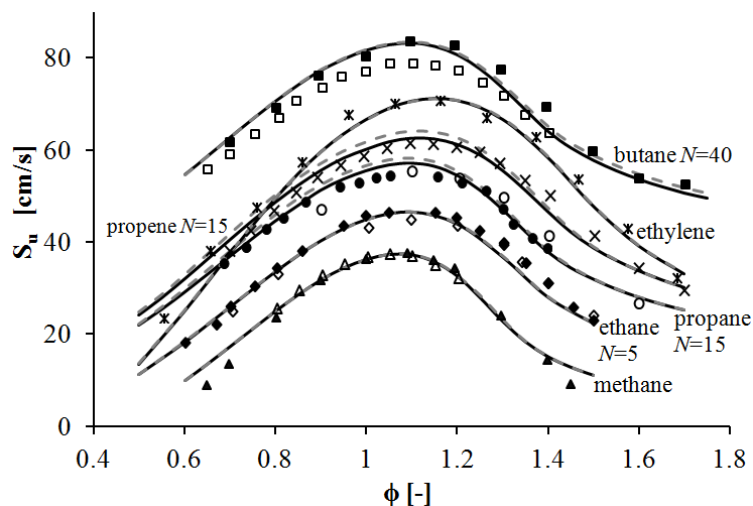


Figure 5.18: Simulated and experimental laminar flame speeds at 298 K and 1 atm, offset by N cm/s.

The good agreement between the simulated and the experimental values confirms again that removing the species with the lowest necessity values does not change the key reactions of the reactive C_0 - C_6 species formed. Therefore, the validations of the C_0 - C_6 species are largely unaffected.

5.2.6 Three-stage flow analysis

At temperatures as low as 393 K, some fuel-air mixtures react chemically and produce very weak flames called cool flames, which generate very little heat. The reaction is not burned; rather, the molecules break down and recombine to produce a variety of stable chemical compounds including alcohols, acids, peroxides, aldehydes, and carbon monoxide [154]. Cool flame reactions appear, as a self-quenching pressure and temperature pulse, during the two-stage hydrocarbon fuel ignition and are associated with “knocking” in spark-ignited internal combustion engines [155].

In this section, a multi-stage flow analysis is performed to distinguish the reaction pathways during the cool-flame stage and the auto-ignition stage. Figure 5.19 shows the temperature and fuel consumption profile (in mole fractions) in a constant volume reactor at 800 K and 10 atm with stoichiometric MD/air mixtures. It can be seen that the temperature rises a little around 0.7ms due to the effect of the cool flame. Corresponding to this small increase in temperature, the majority of the MD has been consumed at the cool-flame stage. In the transition stage, the consumption of MD continues but is much slower than during the cool-flame stage. The temperature slowly rises during the transition stage. The MD has been completely

consumed before auto-ignition starts. Thereafter, the temperature rises dramatically due to the auto-ignition. In the temperature and fuel consumption profiles, the character of the fuel and the temperature at different stages is clearly visible. To fully understand the reaction pathways during the different stages in detail, a three-stage simulation was performed as follows:

- 1st stage (cool-flame stage) with reacting time (0-1 ms)
- 2nd stage (transition stage) with reacting time (1-6.2 ms)
- 3rd stage (auto-ignition stage) with reacting time (6.2-7.5 ms)

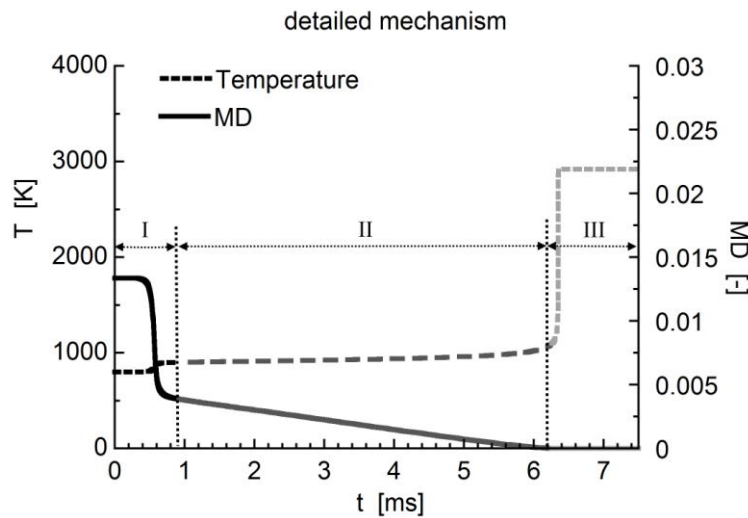


Figure 5.19: 3-stage T and MD profile for ignition delays, stoichiometric MD/air mixtures at 10 atm and 800 K (with detailed mechanism)

The carbon flow for the decomposition of $C_{11}H_{21}O_2-r3$ instead of the fuel molecule (MD) was applied again in Figure 5.20 due to the size limitations, as explained before.

detailed MD

C flow for 3 time zones:

0-0.9 ms/0.9-6.2 ms/6.2-7.5 ms

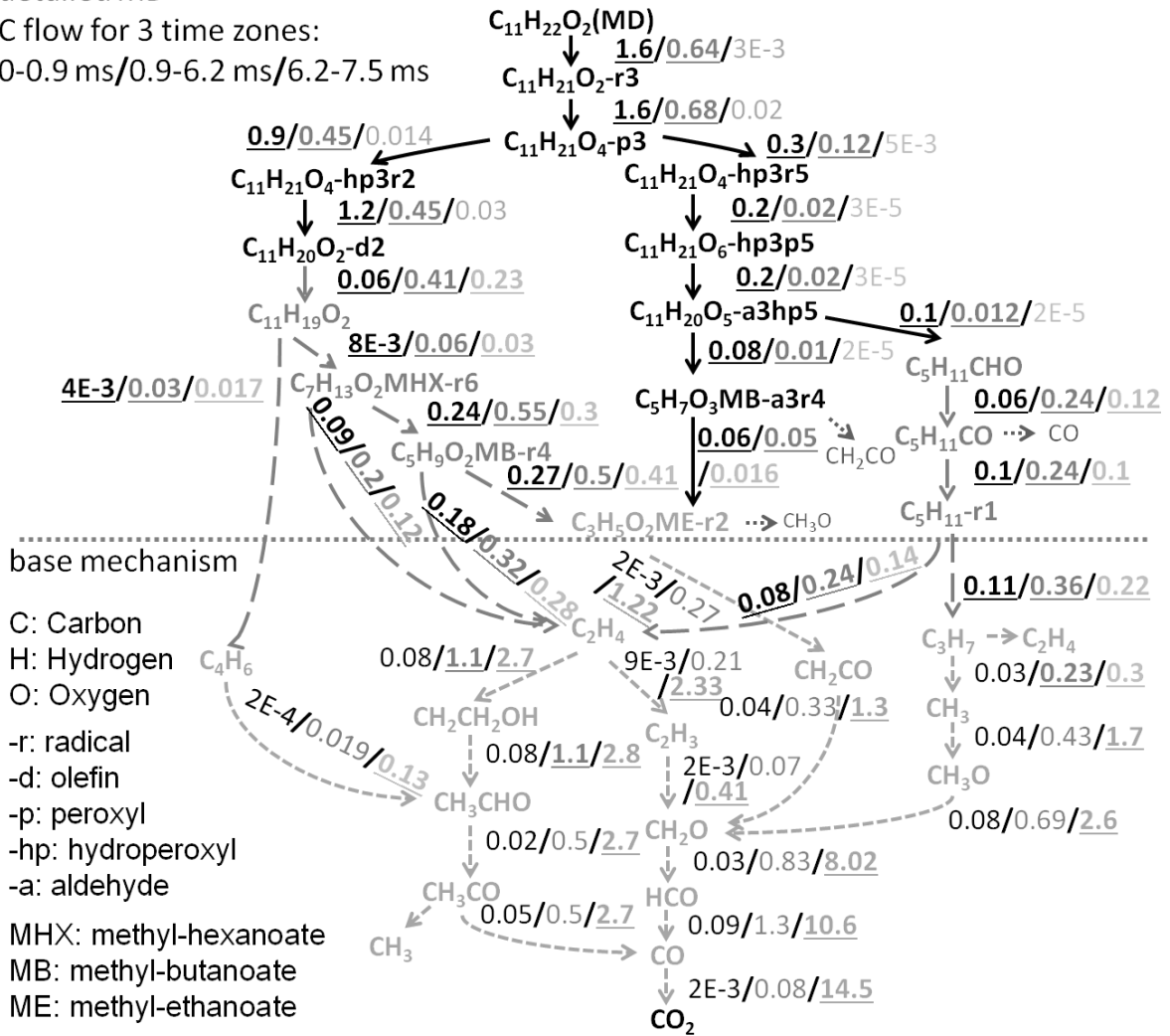


Figure 5.20: 3-stage flow analysis for ignition delays, stoichiometric MD/air mixtures at 10 atm and 800 K (with detailed mechanism)

In the 1st stage (cool flame), MD decomposes into MD radicals through H atom abstraction, which further react with oxygen and form peroxide radicals. The peroxide radicals produce hydroperoxide radicals ($C_{11}H_{21}O_4$ -hp3r2 and $C_{11}H_{21}O_4$ -hp3r5) through isomerization. Later, the hydroperoxide radical ($C_{11}H_{21}O_4$ -hp3r5) reacts with oxygen and forms a peroxide hydroperoxide radical ($C_{11}H_{21}O_6$ -hp3p5), while the hydroperoxide radical ($C_{11}H_{21}O_4$ -hp3r2) yields olefin ($C_{11}H_{20}O_2$ -d2). These products generate further intermediate species such as olefins, aldehydes, or ketones.

In the 2nd stage (after cool flame and before auto-ignition), the main pathways are similar to the pathways in the 1st stage with a lower flow amount since the majority of the fuel has been consumed. The most prominently featured pathway in this stage is the decomposition of stable species such as olefins (L - $C_{11}H_{20}O_2$, C_2H_4), ketones ($C_5H_{11}CHO$), and other large radicals such as $C_{11}H_{19}O_2$, $C_7H_{13}O_2$ MHX-r6, and $C_5H_{11}CO$. The decomposition process of these

intermediate species, which are indirectly derived from fuel molecules, increases the temperature and the pressure, and therefore accumulates the energy for auto-ignition.

In the 3rd stage (auto-ignition stage), the MD has been exhausted and the main flows are the reactions responsible for auto-ignition. Only these auto-ignition-relevant reactions are responsible for the small species (such as C₂H₄, CH₂O, HCO, and CO). In this way, the base mechanism, which is irrelevant for the fuel decomposition, is of importance at this stage.

The 3-stage flow analysis was also performed for the skeletal mechanism. Since C₁₁H₂₁O₂-r3 and other relevant species were lumped into the corresponding “lumped species”, the “lumped species” instead of the detailed species are depicted in the flow analysis. The comparison of Figure 5.20 and Figure 5.22 shows that the general features found in the detailed mechanism are also observed in the skeletal mechanism.

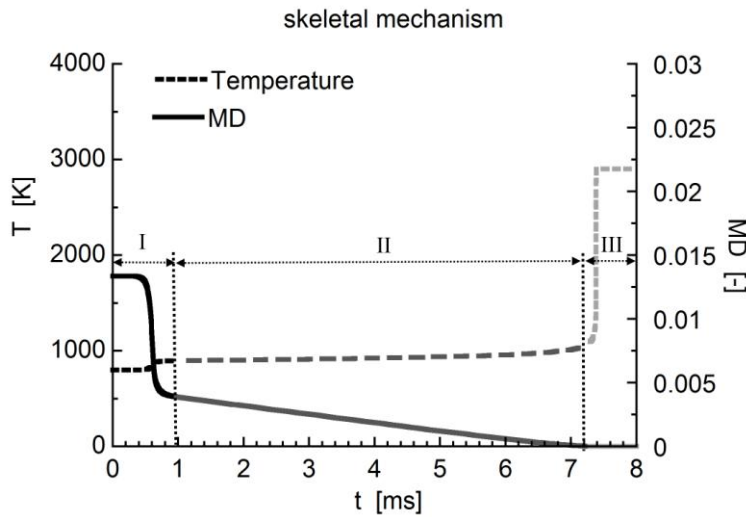


Figure 5.21: 3-stage T and MD profile for ignition delays, stoichiometric MD/air mixtures at 10 atm and 800 K (with skeletal mechanism)

reduced MD

C flow for 3 time zones:

0-1 ms/1-7.2 ms/7.2-8 ms

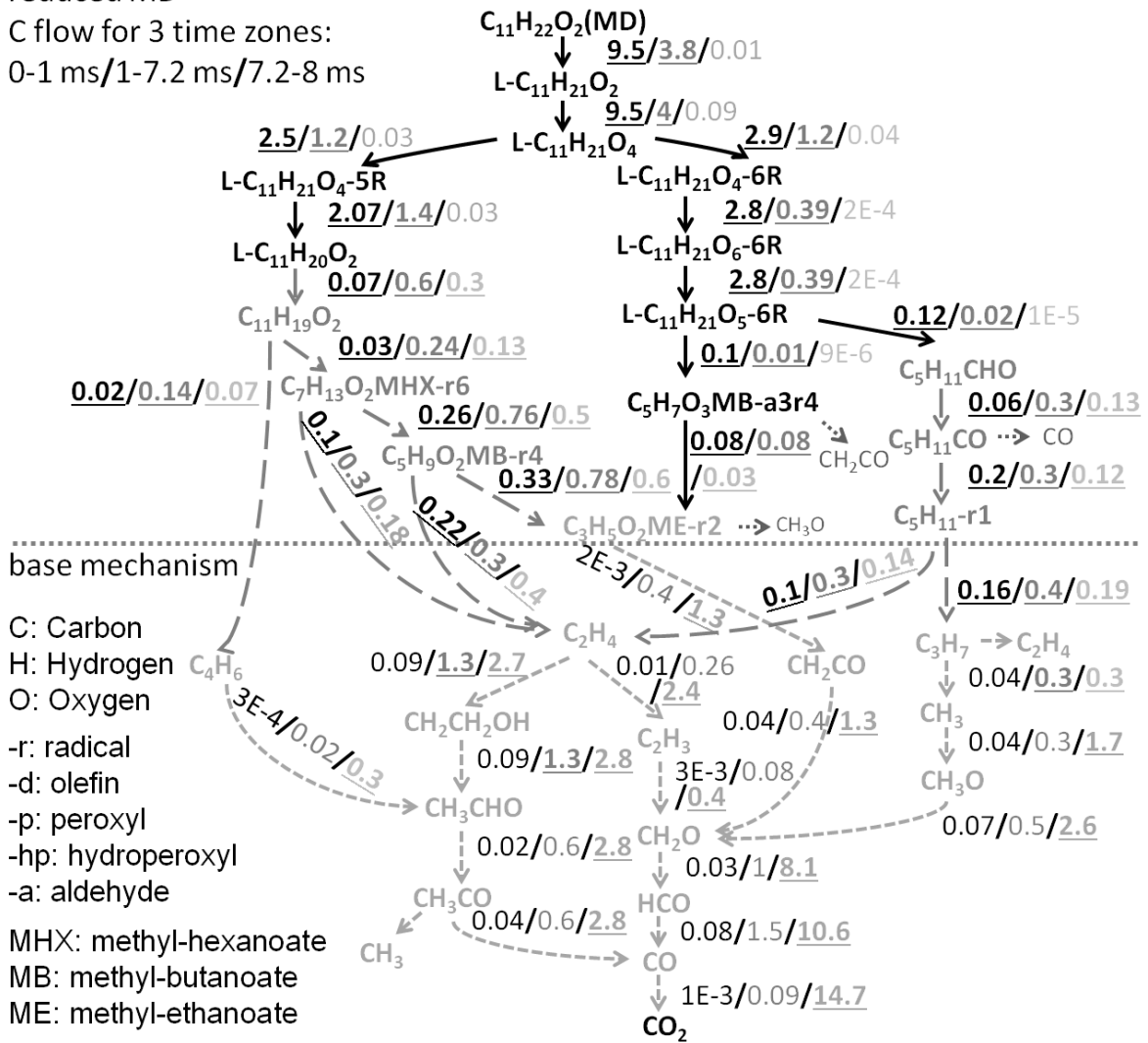


Figure 5.22: 3-stage flow analysis for ignition delays, stoichiometric MD/air mixtures at 10 atm and 800 K (with skeletal mechanism)

5.3 Surrogate component for biodiesel

Vegetable oils such as palm, jatropha, corn, cottonseed, linseed, safflower, sunflower, olive, soy, and rapeseed oil, as well as animal fats (such as beef tallow) can all produce biodiesel with the same five methyl-ester components, as shown in Table 5.7 by Westbrook et al. [156]. Their approximate CN values are referred from Graboski and McCormick [157] and Murphy et al. [158].

Table 5.7 Composition of different biodiesel fuels and their approximate CN values [156]

	Sun	Saff	Linseed	Jatropha	Cotton	Corn	Olive	Tallow	Palm	Peanut	Soy	Rapeseed
Palmitate $C_{17}H_{34}O_2$	7	7	7	4	23	10	13	28	46	11	8	4
Stearate $C_{19}H_{38}O_2$	5	2	1	8	3	4	4	22	4	8	4	1
Oleate $C_{19}H_{36}O_2$	19	13	19	49	20	38	72	46	40	49	25	60
Linoleate $C_{19}H_{34}O_2$	68	78	19	38	53	48	10	3	10	32	55	21
Linolenate $C_{19}H_{32}O_2$	1	0	54	1	1	0	1	1	0	0	8	14
CN	49	50	39	58	51	49	55	58	62	54	47	54

Since biodiesels have five main components and other minor components, it is difficult to develop the surrogate fuel for biodiesel in one step. A helpful approach for developing a kinetic model for complex fuels is to apply surrogate mixtures of pure hydrocarbons to replicate the physical and chemical characteristics of a practical fuel surrogate. A proper surrogate blend simplifies the complicated practical fuels but maintains the fundamental characteristics of the targeted fuel. To date, there have been some progresses in the field of surrogate fuel for biodiesel fuels.

Methyl-butanoate (MB) was initially investigated by Fisher et al. [159] and further investigated by many researchers [160-166]. MB has important features of the methyl-ester group. However, MB does not exhibit NTC behavior, which has been observed for larger methyl-esters such as methyl-palmitate (MP) [167]. Therefore, MB alone is unsuitable for use as a biodiesel surrogate.

The kinetic model of *n*-hexadecane has been used to simulate the combustion of biodiesel [137]. Due to the lack of a methyl-ester group, this model cannot form carbon dioxide early in the corresponding JSR experiment.

Recently, a kinetic model of MP, methyl-stearate, methyl-oleate, methyl-linoleate, and methyl-linolenate has been reported by Westbrook et al. [168] and a lumped biodiesel model including MP, methyl-stearate, methyl-oleate, methyl-linoleate, and methyl-linolenate has been proposed by Saggese et al. [169]. Other surrogate fuels include methyl-octanoate [170], methyl-stearate, and methyl-oleate [171].

MD is considered as a suitable biodiesel surrogate [46, 53, 57, 131-141] (and in current study). MD has a structure that is similar to actual biodiesel and its kinetic model is much more compact than other larger methyl-esters such as MP. Table 5.8 shows the general physi-

cal and thermal properties of MD, biodiesel, and petroleum-based diesel from the literature [4, 10, 172-176]. Each property of MD is very similar to the properties of biodiesel. But the properties of biodiesel are a little different than those of other petroleum-based diesel fuels.

Table 5.8 Summary of general physical and thermal properties [4, 10, 172-176]

Specifications	Petrodiesel		Biodiesel		MD
	ASTM D975	EN 590	ASTM D6751	EN 14214	-
Density (15 °C) [kg/m ³]	850	820-845	880	860-900	873
Kinematic viscosity (40 °C) [mm ² /s = cSt]	2.6	2.0-4.5	1.9-6.0	3.5-5.0	6.0
Flash point [°C]	60-80	>55	Min. 100-170	>120	110
Cetane number[-]	40-55	Min. 51	Min. 47	Min. 51	47.5
Low heating value [MJ/kg]	~ 42-46	~ 43	~ 37	~ 35	34.4*

* calculated

Prior to current study, only one fundamental experimental study had been performed regarding real biodiesel fuels. Wang et al. [177] measured ignition delay experiments by using real biodiesels and biodiesel components as fuel. The comparisons of MD with these experimental data are discussed here. Figure 5.23 compares the experimental results of MP at 10 and 20 atm with the corresponding simulated results obtained from using the skeletal mechanism of MD in the same conditions.

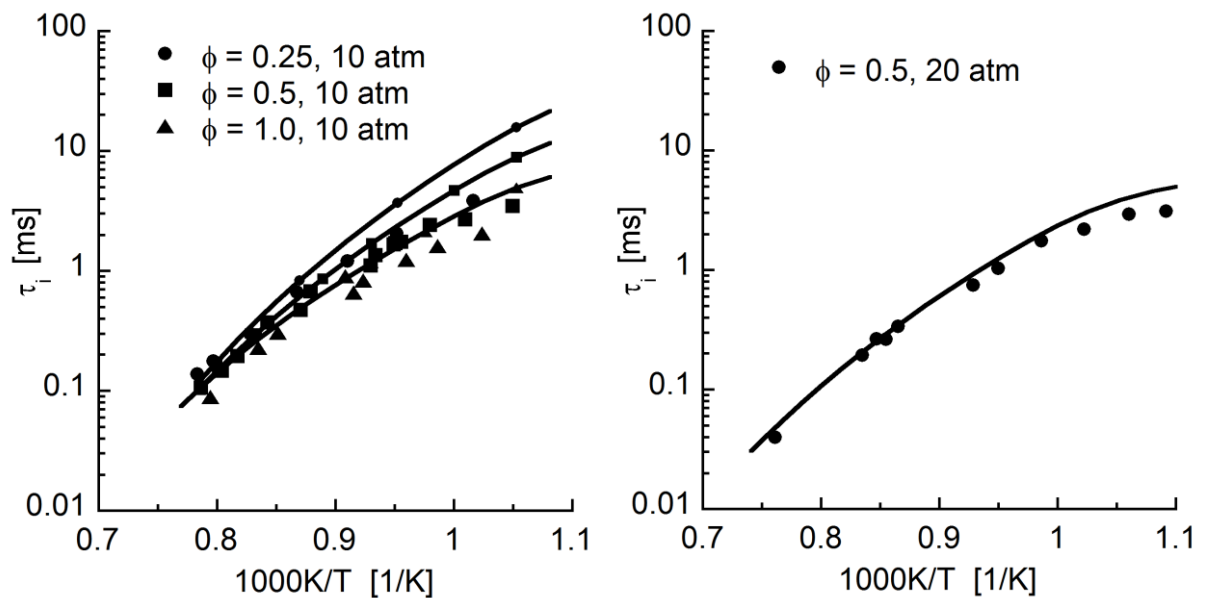


Figure 5.23: Simulated ignition delay times of MD/air mixtures (line); experimental ignition delay times of MP/air mixtures (symbols)

At 10 atm (left figure), the simulated values fit with the experimental data in the temperature region of 1100-1300 K, while in the region of 950-1100 K, the simulated ignition delay times are a bit slower than in the experimental data, especially in fuel-lean conditions.

At 20 atm (right figure), the simulated values fit well with the simulated values in the measured temperature region.

Since the simulated ignition delay times of MD fit with the experimental data of MP, the experimental data of MD [131] were compared with the experimental data of MP [177] at 16 atm. The experimental data of MP were scaled to 16 atm by using $\tau \sim P^{-1}$. Figure 5.24 (fuel-lean conditions) and Figure 5.25 (stoichiometric conditions) clearly demonstrate that MP and MD have almost the same behavior in high-temperature regions. At 900-1100 K, the ignition delay times of MP are slightly faster than those of MD. Due to the lack of data, the behavior of MP in the low-temperature region remains unknown. The model predicts the ignition delay times in stoichiometric conditions well, while under-predicting the ignition delay times in fuel-lean conditions.

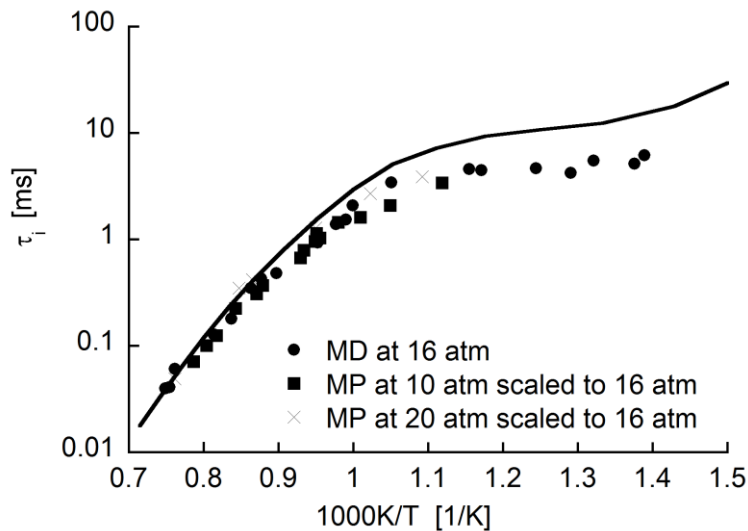


Figure 5.24: Simulated ignition delay times of MD/air mixtures (line); experimental ignition delays of MD/air mixtures and MP/air mixtures (symbols) at $\phi = 0.5$

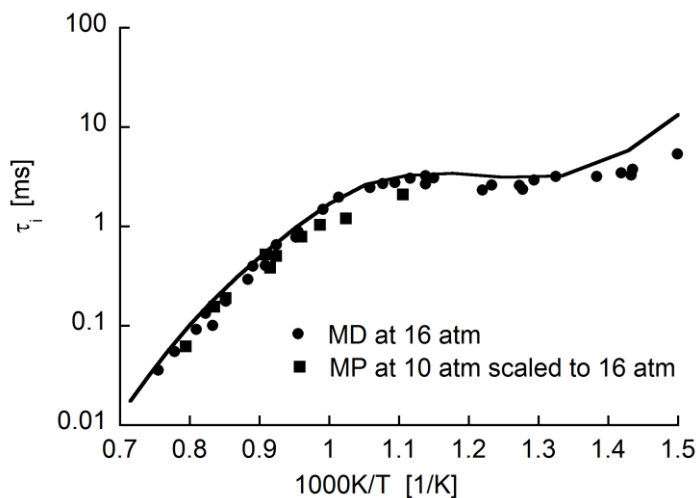


Figure 5.25: Simulated ignition delay times of MD/air mixtures (line); experimental ignition delays of MD/air mixtures and MP/air mixtures (symbols) at $\phi = 1$

According to Table 5.7, the major components of biodiesel are unsaturated methyl-esters. Figure 5.26 shows the ignition delay times of three unsaturated biodiesel components at 10 atm and $\phi = 0.25$.

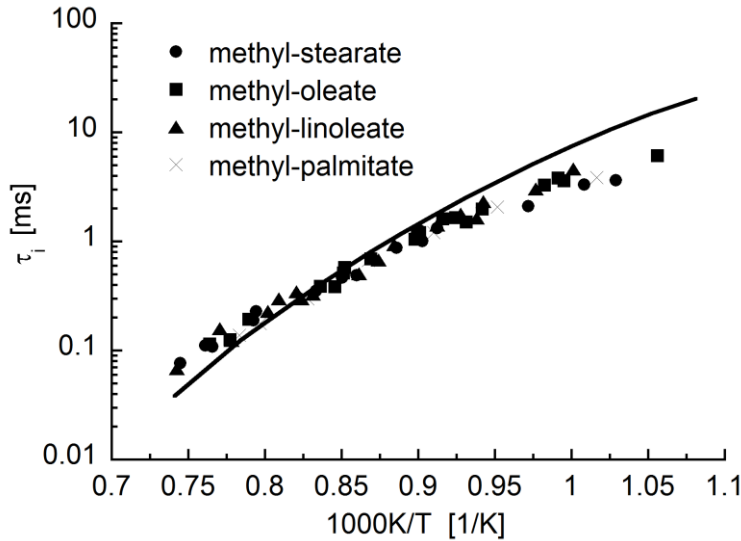


Figure 5.26: Simulated ignition delay times of MD/air mixtures (line); experimental ignition delay times of methyl-esters/air mixtures (symbols) at 10 atm, $\phi = 0.25$

The experimental ignition delay times of three unsaturated methyl-esters fit with each other and their data agree well with those of MP in the same conditions. The simulated results in the skeletal mechanism of MD in the same conditions show some deviation. Such deviation is also found in the validation of MD in fuel-lean conditions. Since there is no experimental data in the lower temperature region, with different fuel/air ratios and pressure conditions, the behavior of unsaturated methyl-ester still requires more measurements to be performed.

The comparison of real biodiesels is plotted in Figure 5.27. The symbols show the experimental ignition delay times of two biodiesel fuels at 10 atm and $\phi = 0.25$. The straight line denotes the simulation of MD using the skeletal mechanism of MD in the same conditions. Agreement for both biodiesels is acceptable and is similar to MP, methyl-stearate, methyl-oleate, and methyl-linoleate.

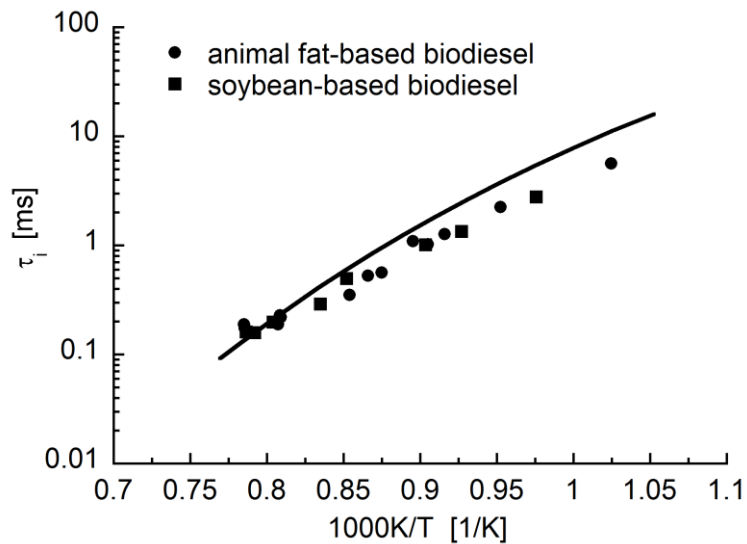


Figure 5.27: Simulated ignition delay times of MD/air mixtures; experimental ignition delay times of two types of biodiesels at 10 atm, $\phi = 0.25$

Both the experimental and the simulated investigation of ignition delay times have proved that MD is a suitable surrogate component, representing a real biodiesel component MP or a simple one-component surrogate for biodiesel fuel. However, more experimental data for biodiesel components and biodiesels are of great importance for further validation of the biodiesel surrogate model.

Unsaturated methyl-esters are important biodiesel components. According to Westbrook et al. [156], Mehl et al. [81], Bounaceur et al. [117], and Herbinet et al. [178], the C=C double bonds within the straight-chain portion inhibit intramolecular H atom abstraction reactions, which are important processes for low-temperature oxidation and for the ignition of saturated hydrocarbons. In future work on biodiesel surrogate fuels, the blend of MD with unsaturated methyl-esters is suggested as a promising direction.

6 Conclusions

6.1 Conclusions

In recent years, biodiesel is an alternative fuel to petroleum diesel that is renewable and creates less harmful emissions than conventional diesel. Biodiesel blends – usually B5 or B20 – are available at more and more service stations in all states [5]. An increasing number of commercial organizations (mining companies and transport companies) are trialing B20 to B100 blends due to the significant greenhouse reduction benefits [5]. The main objective of current study is to develop the kinetic mechanism of *n*-decane/AMN/MD blend as the surrogates for biodiesel/diesel blends. By using the CGR reduction approach, the skeletal oxidation of *n*-decane/AMN/MD blend with skeletal base mechanism includes 295 species and 3500 reversible reactions.

Development of AMN/*n*-decane model (chapter 4)

A compact and comprehensive kinetic mechanism for *n*-decane and AMN, respectively, has been developed and compiled. The oxidation of *n*-decane follows the rules for 25 reaction classes suggested by Curran et al. [32]. The reaction rates mainly follow a previous *n*-heptane study by Ahmed et al. [31], updated with recent studies [75, 78, 81]. The oxidation of AMN follows the AMN combustion [85] and toluene combustion [88, 89]. Some reaction rates were applied from the recent literature [19, 91, 98, 102, 106, 179].

The skeletal *n*-decane oxidation consists of 65 species and 480 reversible reactions. The AMN oxidation consists of 20 species and 92 reversible reactions. Using the compiled, detailed base mechanism [30], the AMN/*n*-decane mechanism has a size of 273 species and 3100 reversible reactions.

One fuel-fuel interaction for IDEA blend is discussed. According to the simulations in constant volume reactor, the chain propagation pathway of $A_2CH_2 + HO_2$ is proved to be the most important OH formation source for AMN oxidation and dominates ignition delay times of AMN. With addition of 10% *n*-decane (even 1% *n*-decane), the AMN/*n*-decane blend becomes much more reactive than pure AMN. With addition of 10% AMN, the reactivity of AMN/*n*-decane blend is slower than that of pure *n*-decane since A_2CH_2 formation is the limiting reaction that inhibits the chain propagation pathway of $A_2CH_2 + HO_2$. The proper reaction rate for chain propagation pathway of $A_2CH_2 + HO_2$ suggested by current study is $1.0E+13 \text{ cm}^3/\text{mol}$. This value is referred from total rate constant by Hippler et al. [89] and is multiplied

with two times. The reaction coefficient for $A_2CH_3 + O_2 = A_2CH_2 + HO_2$ is applied with the recent values measured by Oehlschlaeger et al. [90]. However, the interaction between aromatic and paraffin is still not fully understood and further investigations are of necessary.

Application of AMN/*n*-decane model (chapter 4)

The AMN/*n*-decane blend was examined by means of comprehensive target experiments for *n*-decane, AMN, and the AMN/*n*-decane blend. Ignition delay times, flame speeds, and species composition in JSRs and counter flow flames were successfully simulated for a broad range of temperatures (500-2000 K) and pressures (1-50 bar).

The current AMN/*n*-decane mechanism was applied as the IDEA blend using 30% AMN/70% *n*-decane as fuel. The simulations of the IDEA blend with the current model show acceptable agreement when compared with different experiments of ignition delay times for diesel fuels as well as with flame speed experiments.

Based on the above investigations, the IDEA blend is considered as one two-component diesel surrogate fuel that is suitable for improving kinetic understanding and for application in engine simulations.

Development of MD model (chapter 5)

A compact and comprehensive kinetic mechanism for MD has been developed in current study. The generation rules for the detailed MD mechanism mainly follow the 25 reaction classes suggested by Curran et al. [74]. The reaction rates associated with methyl-ester groups were adopted from Herbinet et al. [46]. For the linear carbon chain (without a methyl-ester group), the reaction rates are mainly based on the study by Ahmed et al. [31].

MD has an asymmetrical molecular structure with one methyl-ester group attached to a long carbon chain. The analysis of bond dissociation energies showed that the bond energies are varied at different secondary carbon positions, yielding different reaction rates [75, 79] for β -scission reactions. MD is the first ester species applying the CGR reduction approach. The observation of different bond energies at the secondary carbon position refines the previous chemical lumping rule. The current study indicates that the criterion for forming lumping species should be the bond energy instead of the functional group (primary carbon, secondary carbon, etc.) Also, using the CGR reduction approach, the detailed mechanism with 619 species and 3600 reversible reactions has been reduced to a skeletal level with 244 species and

3000 reversible reactions. Good maintenance of the chemical information during the reduction has been confirmed by the simulation results, as well as by sensitivity analyses and flow analyses performed using the detailed and the skeletal mechanism.

Another feature of mechanism development has been the development of three-stage flow analyses for visualizing different flow pathways.

Application of MD model (chapter 5)

The detailed and compact models were validated with experimental data for MD over a wide range of temperature (500 to 1500 K) and pressure (1 to 20 bar) and for different fuel/oxidizer ratios. The validations included ignition delay times, flame speeds, as well as speciation in reactor experiments and counter-flow flames. The good agreement between the model and the experiments proves that this MD model is a reliable kinetic model for simulations, either used by itself or in combination with IDEA blend.

The MD model was compared with available experimental ignition delay times of real biodiesel fuels. The acceptable agreement shows the possibility of using this MD model as a simple one-component biodiesel surrogate.

Due to limitation of time, the validation and analysis of *n*-decane/AMN/MD blend has not yet been investigated and further research work would be necessary.

6.2 Suggestions for future research

Several areas have been identified where further research would be valuable and provide new insights:

- More measurements regarding the laminar flame speeds of AMN are important for understanding the oxidation of AMN.
- More measurements regarding the ignition delay times and laminar flame speeds of diesel are needed for further developing the surrogate diesel model.
- In future work on *n*-decane/AMN/MD blend, validation and comparison with respective experiments are necessary for comprehensively understanding the model behavior.
- In future work on biodiesel surrogate fuels, blending MD with unsaturated methyl-esters is suggested as an interesting direction.

Bibliography

1. Hentschel, W., K.-P. Schindler, and O. Haahtela, *European Diesel research IDEA - Experimental results from DI Diesel engine investigations*. 1994. p. SAE Technical Paper 941954.
2. Barths, H., H. Pitsch, and N. Peters, *3D simulation of DI Diesel combustion and pollutant formation using a two-component reference fuel*. OIL GAS SCI TECHNOL, 1999. **54**(2): p. 233-244.
3. Barths, H., C. Hasse, and N. Peters, *Computational fluid dynamics modelling of non-premixed combustion in direct injection Diesel engines*. INT J ENGINE RES, 2000. **1**(3): p. 249-267.
4. Atadashi, I.M., M.K. Aroua, and A.A. Aziz, *High quality biodiesel and its diesel engine application: A review*. RENEW SUST ENERG REV, 2010. **14**(7): p. 1999-2008.
5. [cited 2017 15 August]; Available from: <https://de.wikipedia.org/wiki/Biodiesel>.
6. board, N.b. [cited 2017 15 August]; Available from: www.biodiesel.org.
7. *Biodiesel Handling and Use Guide*. [cited 2017 15 August]; Available from: <https://www.nrel.gov/docs/fy09osti/43672.pdf>.
8. Demirbas, A., *Progress and recent trends in biofuels*. PROG ENERG COMBUST, 2007. **33**(1): p. 1-18.
9. Demirbas, A., *Biodiesel production from vegetable oils via catalytic and non-catalytic supercritical methanol transesterification methods*. PROG ENERG COMBUST, 2005. **31**(5-6): p. 466-487.
10. Agarwal, A.K., *Biofuels (alcohols and biodiesel) applications as fuels for internal combustion engines*. PROG ENERG COMBUST, 2007. **33**(3): p. 233-271.
11. Kohse-Höinghaus, K., et al., *Biofuel Combustion Chemistry: From Ethanol to Biodiesel*. ANGEW CHEM INT EDIT, 2010. **49**(21): p. 3572-3597.
12. Warnatz, J., U. Maas, and R.W. Dibble, *Combustion*. 1997, Heidelberg: Springer Verlag.
13. J A Miller, a. R J Kee, and C.K. Westbrook, *Chemical Kinetics and Combustion Modeling*. Annual Review of Physical Chemistry, 1990. **41**(1): p. 345-387.
14. Metiu, H., *Physical Chemistry: Kinetics* 2006, New York: Taylor & Francis Press.
15. Pollard, R.T., *Hydrocarbons*, in *Comprehensive Chemical Kinetics*, C.H. Bamford and C.F.H. Tipper, Editors. 1977, Elsevier. p. 249-367.
16. Nilsson, D., *Automatic Analysis and Reduction of Reaction Mechanisms for Complex Fuel Composition*. 2001, Lund University.

-
17. Bhaskaran, K.A. and P. Roth, *The shock tube as wave reactor for kinetic studies and material systems*. PROG ENERG COMBUST, 2002. **28**(2): p. 151-192.
 18. Kee, R.J., M.E. Coltrin, and P. Glarborg, *Chemically Reacting Flow: Theory and Practice*. 2005: Wiley Press.
 19. Mauß, F., *Entwicklung eines kinetischen Modells der Russbildung mit schneller Polymerisation*. 1998, RWTH Aachen.
 20. Warnatz, J., *Hydrocarbon oxidation high-temperature chemistry*. PURE APPL CHEM, 2000. **72**(11): p. 2101-2110.
 21. Miller, J.A., *Theory and modeling in combustion chemistry*. SYMP (INT) COMBUST, 1996. **26**(1): p. 461-480.
 22. C., C., *Entwicklung eines detaillierten Reaktionsmechanismus zur Modellierung der Verbrennungsprozesse von Kohlenwasserstoffen bei Hoch- und Niedertemperaturbedingungen*. 1993, Universität Heidelberg.
 23. V., K. 1997, Universität Heidelberg.
 24. Frenklach, M. and J. Warnatz, *Detailed Modeling of PAH Profiles in a Sooting Low-Pressure Acetylene Flame*. COMBUST SCI TECHNOL, 1987. **51**(4-6): p. 265-283.
 25. Wang, H. and M. Frenklach, *A detailed kinetic modeling study of aromatics formation in laminar premixed acetylene and ethylene flames*. COMBUST FLAME, 1997. **110**(1-2): p. 173-221.
 26. Hoyermann, K., F. Mauss, and T. Zeuch, *A detailed chemical reaction mechanism for the oxidation of hydrocarbons and its application to the analysis of benzene formation in fuel-rich premixed laminar acetylene and propene flames*. PHYS CHEM CHEM PHYS, 2004. **6**(14): p. 3824-3835.
 27. Qin, Z., et al., *Combustion chemistry of propane: A case study of detailed reaction mechanism optimization*. P COMBUST INST, 2000. **28**(2): p. 1663-1669.
 28. Ahmed, S.S., F. Mauss, and T. Zeuch, *The Generation of a Compact n-Heptane / Toluene Reaction Mechanism Using the Chemistry Guided Reduction (CGR) Technique*. Z PHYS CHEM, 2009. **223**(4-5): p. 551-563.
 29. Oßwald, P., et al., *Combustion Chemistry of the Butane Isomers in Premixed Low-Pressure Flames*. Z PHYS CHEM, 2011. **225**(9-10): p. 1029-1054.
 30. Schenk, M., et al., *Detailed mass spectrometric and modeling study of isomeric butene flames*. COMBUST FLAME, 2013. **160**(3): p. 487-503.
 31. Ahmed, S.S., et al., *A comprehensive and compact n-heptane oxidation model derived using chemical lumping*. PHYS CHEM CHEM PHYS, 2007. **9**(9): p. 1107-1126.
 32. Nawdiyal, A., et al., *Experimental and modelling study of speciation and benzene formation pathways in premixed 1-hexene flames*. P COMBUST INST, 2015. **35**(1): p. 325-332.

-
33. Seidel, L., et al., *Comprehensive kinetic modeling and experimental study of a fuel-rich, premixed n-heptane flame*. COMBUST FLAME, 2015. **162**(5): p. 2045-2058.
 34. Wang, X., *Mechanism Generation for Hydrocarbon Fuels*. 2011, Brandenburgische Technische Universität Cottbus - Senftenberg.
 35. Seidel, L., *Optimisation of a detailed iso-octane / n-heptane mechanism and reduction to skeletal size*. 2009, Brandenburgische Technische Universität Cottbus - Senftenberg.
 36. Nawdiyal, A., L. Leon, and F. Mauss, *Development of a high temperature mechanism for methylcyclohexane oxidation*, in *Poster session presented at the 36th International Symposium on Combustion*. 2016: Seoul, South Korea.
 37. Burcat, A. and B. Ruscic, *Third Millennium Ideal Gas and Condensed Phase Thermochemical Database for Combustion with Updates from Active Thermochemical Tables*. 2005.
 38. Stagni, A., et al., *Lumping and Reduction of Detailed Kinetic Schemes: an Effective Coupling*. IND ENG CHEM RES, 2014. **53**(22): p. 9004-9016.
 39. Lu, T. and C.K. Law, *A directed relation graph method for mechanism reduction*. P COMBUST INST, 2005. **30**(1): p. 1333-1341.
 40. Soyhan, H.S., F. Mauss, and C. Sorousbay, *Chemical kinetic modeling of combustion in internal combustion engines using reduced chemistry*. COMBUST SCI TECHNOL, 2002. **174**(11-12): p. 73-91.
 41. Løvås, T., D. Nilsson, and F. Mauss, *Automatic reduction procedure for chemical mechanisms applied to premixed methane/air flames*. P COMBUST INST, 2000. **28**(2): p. 1809-1815.
 42. Løvås, T., et al., *Comparison of automatic reduction procedures for ignition chemistry*. P COMBUST INST, 2002. **29**(1): p. 1387-1393.
 43. Zeuch, T., et al., *A comprehensive skeletal mechanism for the oxidation of n-heptane generated by chemistry-guided reduction*. COMBUST FLAME, 2008. **155**(4): p. 651-674.
 44. Farrell, J.T., et al., *Development of an experimental database and kinetic models for surrogate Diesel fuels*. 2007. p. SAE Technical Paper 2007-01-0201.
 45. Dagaut, P., M. Reuillon, and M. Cathonnet, *short communication. High pressure oxidation of liquid fuels from low to high temperature.3. n-decane*. COMBUST SCI TECHNOL, 1994. **103**(1-6): p. 349-359.
 46. Herbinet, O., W.J. Pitz, and C.K. Westbrook, *Detailed chemical kinetic oxidation mechanism for a biodiesel surrogate*. COMBUST FLAME, 2008. **154**(3): p. 507-528.
 47. Pfahl, U., K. Fieweger, and G. Adomeit, *Self-ignition of Diesel-relevant hydrocarbon-air mixtures under engine conditions*. SYMP (INT) COMBUST, 1996. **26**(1): p. 781-789.
 48. Dean, A.J., et al., *Autoignition of surrogate fuels at elevated temperatures and*

-
- pressures. P COMBUST INST, 2007. **31**(2): p. 2481-2488.
49. Zhukov, V.P., V.A. Sechenov, and A.Y. Starikovskii, *Autoignition of n-decane at high pressure*. COMBUST FLAME, 2008. **153**(1-2): p. 130-136.
 50. Shen, H.-P.S., et al., *A shock tube study of the ignition of n-heptane, n-decane, n-dodecane, and n-tetradecane at elevated pressures*. ENERG FUEL, 2009. **23**(5): p. 2482-2489.
 51. Olchanski, E. and A. Burcat, *Decane oxidation in a shock tube*. INT J CHEM KINET, 2006. **38**(12): p. 703-713.
 52. Horning, D.C., *A study of the high temperature autoignition and thermal decomposition of hydrocarbons*. 2001, Stanford University.
 53. Haylett, D.R., D.F. Davidson, and R.K. Hanson, *Ignition delay times of low-vapor-pressure fuels measured using an aerosol shock tube*. COMBUST FLAME, 2012. **159**(2): p. 552-561.
 54. Wagner, P. and G.L. Dugger, *Flame propagation. V. Structural influences on burning velocity*. J AM CHEM SOC, 1955. **77**(1): p. 227-231.
 55. Zhao, Z., et al., *Burning velocities and a high-temperature skeletal kinetic model for n-decane*. COMBUST SCI TECHNOL, 2004. **177**(1): p. 89-106.
 56. Kumar, K. and C. Sung, *Laminar flame speeds and extinction limits of preheated n-decane/O₂/N₂ and n-dodecane/O₂/N₂ mixtures*. COMBUST FLAME, 2007. **151**(1-2): p. 209-224.
 57. Wang, Y.L., et al., *Studies of C4 and C10 methyl ester flames*. COMBUST FLAME, 2011. **158**(8): p. 1507-1519.
 58. Ji, C., et al., *Propagation and extinction of premixed C5–C12 n-alkane flames*. COMBUST FLAME, 2010. **157**(2): p. 277-287.
 59. Bales-Gueret, C., et al., *Experimental study and kinetic modeling of higher hydrocarbon oxidation in a jet-stirred flow reactor*. ENERG FUEL, 1992. **6**(2): p. 189-194.
 60. Dagaut, P., A. El Bakali, and A. Ristori, *The combustion of kerosene: Experimental results and kinetic modelling using 1- to 3-component surrogate model fuels*. FUEL, 2006. **85**(7-8): p. 944-956.
 61. Biet, J., et al., *Experimental and modeling study of the low-temperature oxidation of large alkanes*. ENERG FUEL, 2008. **22**(4): p. 2258-2269.
 62. Zeppieri, S.P., S.D. Klotz, and F.L. Dryer, *Modeling concepts for larger carbon number alkanes: A partially reduced skeletal mechanism for n-decane oxidation and pyrolysis*. P COMBUST INST, 2000. **28**(2): p. 1587-1595.
 63. Jahangirian, S., et al., *A detailed experimental and kinetic modeling study of n-decane oxidation at elevated pressures*. COMBUST FLAME, 2012. **159**(1): p. 30-43.

-
64. Delfau, J.-L., et al., *Experimental and computational investigation of the structure of a sooting decane-O₂-Ar flame*. SYMP (INT) COMBUST, 1991. **23**(1): p. 1567-1572.
65. Doute, C., J.-L. Delfau, and C. Vovelle, *Modeling of the structure of a premixed n-decane flame*. COMBUST SCI TECHNOL, 1997. **130**(1-6): p. 269-313.
66. Glaude, P.A., et al., *Modeling of the oxidation of n-octane and n-decane using an automatic generation of mechanisms*. INT J CHEM KINET, 1998. **30**(12): p. 949-959.
67. Ranzi, E., et al., *A wide range kinetic modeling study of pyrolysis, oxidation and combustion of heavy n-alkanes*. IND ENG CHEM RES, 2005. **44**(14): p. 5170-5183.
68. Battin-Leclerc, F., et al., *Modeling of the gas-phase oxidation of n-decane from 550 to 1600 K*. P COMBUST INST, 2000. **28**(2): p. 1597-1605.
69. Bikas, G. and N. Peters, *Kinetic modelling of n-decane combustion and autoignition: Modeling combustion of n-decane*. COMBUST FLAME, 2001. **126**(1-2): p. 1456-1475.
70. Moréac, G., E.S. Blurock, and F. Mauß, *Automatic generation of a detailed mechanism for the oxidation of n-decane*. COMBUST SCI TECHNOL, 2006. **178**(10-11): p. 2025-2038.
71. Westbrook, C.K., et al., *A comprehensive detailed chemical kinetic reaction mechanism for combustion of n-alkane hydrocarbons from n-octane to n-hexadecane*. COMBUST FLAME, 2009. **156**(1): p. 181-199.
72. Kumar, K., G. Mittal, and C.-J. Sung, *Autoignition of n-decane under elevated pressure and low-to-intermediate temperature conditions*. COMBUST FLAME, 2009. **156**(6): p. 1278-1288.
73. Dryer, F.L. and K. Brezinsky, *A Flow Reactor Study of the Oxidation of n-Octane and Iso-Octane*. COMBUST SCI TECHNOL, 1986. **45**(3-4): p. 199-212.
74. Curran, H.J., et al., *A comprehensive modeling study of n-heptane oxidation*. COMBUST FLAME, 1998. **114**(1-2): p. 149-177.
75. Sivaramakrishnan, R. and J.V. Michael, *Rate Constants for OH with Selected Large Alkanes: Shock-Tube Measurements and an Improved Group Scheme*. J PHYS CHEM A, 2009. **113**(17): p. 5047-5060.
76. Atkinson, R., *Kinetics of the gas-phase reactions of OH radicals with alkanes and cycloalkanes*. Atmos. Chem. Phys., 2003. **3**(6): p. 2233-2307.
77. Cohen, N., *Are reaction rate coefficients additive? Revised transition state theory calculations for OH + alkane reactions*. International Journal of Chemical Kinetics, 1991. **23**(5): p. 397-417.
78. El Bakali, A., J.-L. Delfau, and C. Vovelle, *Kinetic modeling of a rich, atmospheric pressure, premixed n-heptane/O₂/N₂ flame*. COMBUST FLAME, 1999. **118**(3): p. 381-398.
79. Allara, D.L. and R. Shaw, *A compilation of kinetic parameters for the thermal*

-
- degradation of n - alkane molecules.* J PHYS CHEM REF DATA, 1980. **9**(3): p. 523-560.
80. Olzmann, M. and K. Scherzer, *Zur unimolekularen β -Spaltung großer n-Alkylradikale.* BERICH BUNSEN GESELL, 1988. **92**(8): p. 908-916.
81. Mehl, M., et al., *Oxidation and combustion of the n-hexene isomers: A wide range kinetic modeling study.* COMBUST FLAME, 2008. **155**(4): p. 756-772.
82. Pitsch, H., *Detailed kinetic reaction mechanism for ignition and oxidation of alpha-methylnaphthalene.* SYMP (INT) COMBUST, 1996. **26**(1): p. 721-728.
83. Shaddix, C.R., K. Brezinsky, and I. Glassman, *Oxidation of 1-methylnaphthalene.* SYMP (INT) COMBUST, 1992. **24**(1): p. 683-690.
84. Shaddix, C.R., K. Brezinsky, and I. Glassman, *Analysis of fuel decay routes in the high-temperature oxidation of 1-methylnaphthalene.* COMBUST FLAME, 1997. **108**(1-2): p. 139-157.
85. Mati, K., et al., *Oxidation of 1-methylnaphthalene at 1-13 atm: experimental study in a JSR and detailed chemical kinetic modeling.* COMBUST SCI TECHNOL, 2007. **179**(7): p. 1261-1285.
86. Wang, H., et al., *An experimental and kinetic modeling study of the autoignition of alpha-methylnaphthalene/air and alpha-methylnaphthalene/n-decane/air mixtures at elevated pressures.* COMBUST FLAME, 2010. **157**(10): p. 1976-1988.
87. Marchal, A., *Etude de la contribution des familles chimiques constitutives des gazoles à la formation de polluants non réglementés.* 1997, Université d'Orléans.
88. Emdee, J.L., K. Brezinsky, and I. Glassman, *A kinetic model for the oxidation of toluene near 1200 K.* J PHYS CHEM-US, 1992. **96**(5): p. 2151-2161.
89. Bounaceur, R., et al., *Experimental and modeling study of the oxidation of toluene.* INT J CHEM KINET, 2005. **37**(1): p. 25-49.
90. Oehlschlaeger, M.A., D.F. Davidson, and R.K. Hanson, *Investigation of the reaction of toluene with molecular oxygen in shock-heated gases.* COMBUST FLAME, 2006. **147**(3): p. 195-208.
91. Klippenstein, S.J., L.B. Harding, and Y. Georgievskii, *On the formation and decomposition of C₇H₈.* P COMBUST INST, 2007. **31**(1): p. 221-229.
92. Marinov, N.M., et al., *Modeling of aromatic and polycyclic aromatic hydrocarbon formation in premixed methane and ethane flames.* COMBUST SCI TECHNOL, 1996. **116**(1-6): p. 211-287.
93. Colket, M.B. and D.J. Seery, *Reaction mechanisms for toluene pyrolysis.* SYMP (INT) COMBUST, 1994. **25**(1): p. 883-891.
94. Baulch, D.L., et al., *Evaluated kinetic data for combustion modeling. supplement I.* J PHYS CHEM REF DATA, 1994. **23**(6): p. 847-848.

-
95. Fahr, A. and S.E. Stein, *Gas-phase reactions of phenyl radicals with aromatic molecules*. J PHYS CHEM-US, 1988. **92**(17): p. 4951-4955.
 96. Robaugh, D. and W. Tsang, *Mechanism and rate of hydrogen atom attack on toluene at high temperatures*. J PHYS CHEM-US, 1986. **90**(17): p. 4159-4163.
 97. Nicovich, J.M., C.A. Gump, and A.R. Ravishankara, *Rates of reactions of atomic oxygen(3P) with benzene and toluene*. J PHYS CHEM-US, 1982. **86**(9): p. 1684-1690.
 98. Hippler, H., C. Reihls, and J. Troe, *Shock tube UV absorption study of the oxidation of benzyl radicals*. SYMP (INT) COMBUST, 1991. **23**(1): p. 37-43.
 99. Miller, J.A. and C.F. Melius, *Kinetic and thermodynamic issues in the formation of aromatic compounds in flames of aliphatic fuels*. COMBUST FLAME, 1992. **91**(1): p. 21-39.
 100. Frank, P., et al., *High-temperature reactions of phenyl oxidation*. SYMP (INT) COMBUST, 1994. **25**(1): p. 833-840.
 101. Bittker, D.A., *Detailed mechanism for oxidation of benzene*. COMBUST SCI TECHNOL, 1991. **79**(1-3): p. 49-72.
 102. Battin-Leclerc, F., et al., *Experimental and modeling study of the oxidation of xylenes*. INT J CHEM KINET, 2006. **38**(4): p. 284-302.
 103. Grela, M.A. and A.J. Colussi, *Kinetics and mechanism of the thermal decomposition of unsaturated aldehydes: benzaldehyde, 2-butenal, and 2-furaldehyde*. J PHYS CHEM-US, 1986. **90**(3): p. 434-437.
 104. Asaba, T. and N. Fujii, *Shock-tube study of high-temperature pyrolysis of benzene*. SYMP (INT) COMBUST, 1971. **13**(1): p. 155-164.
 105. Eng, R.A., et al., *Kinetic investigations of the reactions of toluene and of p-xylene with molecular oxygen between 1050 and 1400 K*. SYMP (INT) COMBUST, 1998. **27**(1): p. 211-218.
 106. Ingham, T., R.W. Walker, and R.E. Woolford, *Kinetic parameters for the initiation reaction $RH+O_2=>R+HO_2$* . SYMP (INT) COMBUST, 1994. **25**(1): p. 767-774.
 107. Baulch, D.L., et al., *Evaluated kinetic data for combustion modeling: supplement II*. J PHYS CHEM REF DATA 2005. **34**(3): p. 757-1397.
 108. Burcat, A. and B. Ruscic, *Third millennium ideal gas and condensed phase thermochemical database for combustion with updates from active thermochemical tables*. 2005: <http://garfield.chem.elte.hu/Burcat/burcat.html>.
 109. Zellner, R., S.W. Benson: *Thermochemical Kinetics*. 1977, John Wiley & Sons: New York-London-Sydney-Toronto. p. 877-878.
 110. Ramirez L, H.P., et al., *Kinetics of oxidation of commercial and surrogate diesel fuels in a jet-stirred reactor: Experimental and modeling studies*. ENERG FUEL, 2010. **24**(3): p. 1668-1676.

-
111. Moriue, O., et al., *Effects of dilution by aromatic hydrocarbons on staged ignition behavior of n-decane droplets*. P COMBUST INST, 2000. **28**(1): p. 969-975.
 112. Bounaceur, R., et al., *Kinetic modelling of a surrogate diesel fuel applied to 3D auto-ignition in HCCI engines*. INT J VEHICLE DES, 2007. **44**(1-2): p. 124-142.
 113. Bartels, M., J. Edelbüttel-Einhaus, and K. Hoyeremann, *The reactions of benzyl radicals with hydrogen atoms, oxygen atoms, and molecular oxygen using EI/REMPI mass spectrometry*. SYMP (INT) COMBUST, 1989. **22**(1): p. 1041-1051.
 114. Colket III, M.B., D.W. Naegeli, and I. Glassman, *High temperature oxidation of acetaldehyde*. SYMP (INT) COMBUST, 1977. **16**(1): p. 1023-1039.
 115. Tsang, W. and R.F. Hampson, *Chemical kinetic data base for combustion chemistry. Part I. Methane and related compounds*. J PHYS CHEM REF DATA, 1986. **15**(3): p. 1087-1279.
 116. Brezinsky, K., T.A. Litzinger, and I. Glassman, *The high temperature oxidation of the methyl side chain of toluene*. INT J CHEM KINET, 1984. **16**(9): p. 1053-1074.
 117. Bounaceur, R., et al., *Influence of the position of the double bond on the autoignition of linear alkenes at low temperature*. P COMBUST INST, 2009. **32**(1): p. 387-394.
 118. Bromly, J.H., et al., *An experimental investigation of the mutually sensitised oxidation of nitric oxide and n-butane*. SYMP (INT) COMBUST, 1992. **24**(1): p. 899-907.
 119. Prabhu, S.K., et al., *The Effect of Nitric Oxide on Autoignition of a Primary Reference Fuel Blend in a Motored Engine*. 1993, SAE International.
 120. Prabhu, S.K., et al., *1-Pentene oxidation and its interaction with nitric oxide in the low and negative temperature coefficient regions*. COMBUST FLAME, 1996. **104**(4): p. 377-390.
 121. Stenlaas, O., et al., *2002-01-2699 The Influence of Nitric Oxide on the Occurrence of Autoignition in the End Gas of Spark Ignition Engines*. SAE SP 2002-01-2699 2002: p. 43-52.
 122. Gogan, A., et al., *2003-01-3122 Knock Modeling: an Integrated Tool for Detailed Chemistry and Engine Cycle Simulation*. SAE SP, 2003: p. 1-10.
 123. Pitz, W.J. and C.J. Mueller, *Recent progress in the development of diesel surrogate fuels*. PROG ENERG COMBUST, 2011. **37**(3): p. 330-350.
 124. Penzyakov, O.G., et al., *High-pressure ethylene oxidation behind reflected shock waves*. P COMBUST INST, 2009. **32**(2): p. 2421-2428.
 125. Haylett, D.R., et al., *Application of an aerosol shock tube to the measurement of Diesel ignition delay times*. P COMBUST INST, 2009. **32**(1): p. 477-484.
 126. Spadaccini, L.J. and J.A. Tevelde, *Autoignition characteristics of aircraft-type fuels*. COMBUST FLAME, 1982. **46**: p. 283-300.
 127. Alptekin, E. and M. Canakci, *Determination of the density and the viscosities of*

-
- biodiesel–diesel fuel blends*. RENEW ENERG, 2008. **33**(12): p. 2623-2630.
128. Chong, C.T. and S. Hochgreb, *Measurements of laminar flame speeds of liquid fuels: Jet-A1, Diesel, palm methyl esters and blends using particle imaging velocimetry (PIV)*. P COMBUST INST, 2011. **33**(1): p. 979-986.
 129. Gomez-Meyer, J.-S., et al., *Laminar flame speed of soy and canola biofuels*. CT&F - Ciencia, Tecnología y Futuro, 2012. **4**: p. 75-83.
 130. Li, B., et al., *Flame propagation of mixtures of air with high molecular weight neat hydrocarbons and practical jet and Diesel fuels*. P COMBUST INST, 2013. **34**(1): p. 727-733.
 131. Wang, W. and M.A. Oehlschlaeger, *A shock tube study of methyl decanoate autoignition at elevated pressures*. COMBUST FLAME, 2012. **159**(2): p. 476-481.
 132. Wang, W., S. Gowdagiri, and M.A. Oehlschlaeger, *Comparative Study of the Autoignition of Methyl Decanoates, Unsaturated Biodiesel Fuel Surrogates*. ENERG FUEL, 2013. **27**(9): p. 5527-5532.
 133. Li, Z., et al., *Autoignition of Methyl Decanoate, a Biodiesel Surrogate, under High-Pressure Exhaust Gas Recirculation Conditions*. ENERG FUEL, 2012. **26**(8): p. 4887-4895.
 134. Campbell, M.F., D.F. Davidson, and R.K. Hanson, *Ignition delay times of very-low-vapor-pressure biodiesel surrogates behind reflected shock waves*. FUEL, 2014. **126**: p. 271-281.
 135. Glaude, P.A., et al., *Modeling of the oxidation of methyl esters-Validation for methyl hexanoate, methyl heptanoate, and methyl decanoate in a jet-stirred reactor*. COMBUST FLAME, 2010. **157**(11): p. 2035-2050.
 136. Sarathy, S.M., et al., *An experimental and kinetic modeling study of methyl decanoate combustion*. P COMBUST INST, 2011. **33**(1): p. 399-405.
 137. Dagaut, P., S. Gail, and M. Sahasrabudhe, *Rapeseed oil methyl ester oxidation over extended ranges of pressure, temperature, and equivalence ratio: Experimental and modeling kinetic study*. P COMBUST INST, 2007. **31**(2): p. 2955-2961.
 138. Diévar, P., et al., *A kinetic model for methyl decanoate combustion*. COMBUST FLAME, 2012. **159**(5): p. 1793-1805.
 139. Seshadri, K., et al., *Experimental and kinetic modeling study of extinction and ignition of methyl decanoate in laminar non-premixed flows*. P COMBUST INST, 2009. **32**(1): p. 1067-1074.
 140. Grana, R., et al., *A wide range kinetic modeling study of pyrolysis and oxidation of methyl butanoate and methyl decanoate – Note II: Lumped kinetic model of decomposition and combustion of methyl esters up to methyl decanoate*. COMBUST FLAME, 2012. **159**(7): p. 2280-2294.
 141. Luo, Z., et al., *A Reduced Mechanism for High-Temperature Oxidation of Biodiesel Surrogates*. ENERG FUEL, 2010. **24**(12): p. 6283-6293.

-
142. Frenklach, M. and D.E. Bornside, *Shock-initiated ignition in methane-propane mixtures*. COMBUST FLAME, 1984. **56**(1): p. 1-27.
 143. Baker, J.A. and G.B. Skinner, *Shock-tube studies on the ignition of ethylene-oxygen-argon mixtures*. COMBUST FLAME, 1972. **19**(3): p. 347-350.
 144. Crossley, R.W., et al., *The effect of higher alkanes on the ignition of methane-oxygen-argon mixtures in shock waves*. COMBUST FLAME, 1972. **19**(3): p. 373-378.
 145. Takahashi, K., et al., *The Addition Effects of Methyl Halides on Ethane Ignition Behind Reflected Shock Waves*. B CHEM SOC JPN, 1989. **62**(7): p. 2138-2145.
 146. Burcat, A., K. Scheller, and A. Lifshitz, *Shock-tube investigation of comparative ignition delay times for C1-C5 alkanes*. COMBUST FLAME, 1971. **16**(1): p. 29-33.
 147. Selle, L., T. Poinso, and B. Ferret, *Experimental and numerical study of the accuracy of flame-speed measurements for methane/air combustion in a slot burner*. COMBUST FLAME, 2011. **158**(1): p. 146-154.
 148. Van Maaren, A., D.S. Thung, and L.R.H. De Goey, *Measurement of Flame Temperature and Adiabatic Burning Velocity of Methane/Air Mixtures*. COMBUST SCI TECHNOL, 1994. **96**(4-6): p. 327-344.
 149. Bosschaart, K.J. and L.P.H. De Goey, *The laminar burning velocity of flames propagating in mixtures of hydrocarbons and air measured with the heat flux method*. COMBUST FLAME, 2004. **136**(3): p. 261-269.
 150. Hirasawa, T., et al., *Determination of Laminar Flame Speeds of Ethylene/n-Butane/Air Flames Using Digital Particle Image Velocimetry*, in *2nd Joint Meeting of the U.S. Section of the Combustion Institute*. 2001: Oakland, California.
 151. Hassan, M.I., et al., *Properties of Laminar Premixed Hydrocarbon/Air Flames at Various Pressures*. J PROPUL POWER, 1998. **14**(4): p. 479-488.
 152. Vagelopoulos, C.M. and F.N. Egolfopoulos, *Direct experimental determination of laminar flame speeds*. SYMP (INT) COMBUST, 1998. **27**(1): p. 513-519.
 153. Davis, S.G., C.K. Law, and H. Wang, *Propene pyrolysis and oxidation kinetics in a flow reactor and laminar flames*. COMBUST FLAME, 1999. **119**(4): p. 375-399.
 154. Pearlman, H. and R.M. Chapek. *Cool Flames and Autoignition: Thermal-Ignition Theory of Combustion Experimentally Validated in Microgravity*. 2000.
 155. Lignola, P.G. and E. Reverchon, *Cool flames*. PROG ENERG COMBUST, 1987. **13**(1): p. 75-96.
 156. Westbrook, C.K., et al., *Detailed chemical kinetic modeling of the effects of CC double bonds on the ignition of biodiesel fuels*. P COMBUST INST, 2013. **34**(2): p. 3049-3056.
 157. Graboski, M.S. and R.L. McCormick, *Combustion of fat and vegetable oil derived fuels in diesel engines*. PROG ENERG COMBUST, 1998. **24**(2): p. 125-164.

-
158. Murphy, M.J., J.D. Taylor, and R.L. McCormick, *Compendium of Experimental Cetane Number Data*. 2004.
 159. Fisher, E.M., et al., *Detailed chemical kinetic mechanisms for combustion of oxygenated fuels*. P COMBUST INST, 2000. **28**(2): p. 1579-1586.
 160. Metcalfe, W.K., et al., *Experimental and Modeling Study of C₅H₁₀O₂ Ethyl and Methyl Esters*. J PHYS CHEM A, 2007. **111**(19): p. 4001-4014.
 161. Dooley, S., H.J. Curran, and J.M. Simmie, *Autoignition measurements and a validated kinetic model for the biodiesel surrogate, methyl butanoate*. COMBUST FLAME, 2008. **153**(1-2): p. 2-32.
 162. Gaïl, S., et al., *A wide-ranging kinetic modeling study of methyl butanoate combustion*. P COMBUST INST, 2007. **31**(1): p. 305-311.
 163. Huynh, L.K. and A. Violi, *Thermal Decomposition of Methyl Butanoate: Ab Initio Study of a Biodiesel Fuel Surrogate*. J ORG CHEM, 2008. **73**(1): p. 94-101.
 164. Huynh, L.K., K.C. Lin, and A. Violi, *Kinetic Modeling of Methyl Butanoate in Shock Tube*. J PHYS CHEM A, 2008. **112**(51): p. 13470-13480.
 165. Farooq, A., et al., *An experimental and computational study of methyl ester decomposition pathways using shock tubes*. P COMBUST INST, 2009. **32**(1): p. 247-253.
 166. Lin, K.C., J.Y.W. Lai, and A. Violi, *The role of the methyl ester moiety in biodiesel combustion: A kinetic modeling comparison of methyl butanoate and n-butane*. FUEL, 2012. **92**(1): p. 16-26.
 167. Hakka, M.H., et al., *Experimental study of the oxidation of large surrogates for diesel and biodiesel fuels*. COMBUST FLAME, 2009. **156**(11): p. 2129-2144.
 168. Westbrook, C.K., et al., *Detailed chemical kinetic reaction mechanisms for soy and rapeseed biodiesel fuels*. COMBUST FLAME, 2011. **158**(4): p. 742-755.
 169. Saggese, C., et al., *A lumped approach to the kinetic modeling of pyrolysis and combustion of biodiesel fuels*. P COMBUST INST, 2013. **34**(1): p. 427-434.
 170. Togbé, C., et al., *Chemical Kinetic Study of the Oxidation of a Biodiesel–Bioethanol Surrogate Fuel: Methyl Octanoate–Ethanol Mixtures*. J PHYS CHEM A, 2010. **114**(11): p. 3896-3908.
 171. Naik, C.V., et al., *Detailed chemical kinetic reaction mechanism for biodiesel components methyl stearate and methyl oleate*. P COMBUST INST, 2011. **33**(1): p. 383-389.
 172. Murugesan, A., et al., *Bio-diesel as an alternative fuel for diesel engines—A review*. RENEW SUST ENERG REV, 2009. **13**(3): p. 653-662.
 173. McIlroy, A., et al., *Basic research needs for clean and efficient combustion of 21st century transportation fuels*. 2006.

-
174. Monteiro, M.R., et al., *Critical review on analytical methods for biodiesel characterization*. TALANTA, 2008. **77**(2): p. 593-605.
 175. Wang, X., et al., *An experimental investigation on spray, ignition and combustion characteristics of biodiesels*. P COMBUST INST, 2011. **33**(2): p. 2071-2077.
 176. Wadumesthrige, K., et al., *Investigation of Lubricity Characteristics of Biodiesel in Petroleum and Synthetic Fuel*. ENERG FUEL, 2009. **23**(4): p. 2229-2234.
 177. Wang, W., S. Gowdagiri, and M.A. Oehlschlaeger, *The high-temperature autoignition of biodiesels and biodiesel components*. COMBUST FLAME, 2014. **161**(12): p. 3014-3021.
 178. Herbinet, O., W.J. Pitz, and C.K. Westbrook, *Detailed chemical kinetic mechanism for the oxidation of biodiesel fuels blend surrogate*. COMBUST FLAME, 2010. **157**(5): p. 893-908.
 179. Lefort, B. and W. Tsang, *High temperature stability of larger aromatic compounds*. COMBUST FLAME, 2011. **158**(4): p. 657-665.

Nomenclature

Symbols		unit
A	Pre-exponential factor in Arrhenius law	$[\frac{cm^3}{mol \cdot s}]$
c_p	Specific heat capacity at constant pressure	$[\frac{J}{kg \cdot K}]$
c_v	Specific heat capacity at constant volume	$[\frac{J}{kg \cdot K}]$
C	Molar concentration	$[\frac{mol}{m^3}]$
D_{nm}	The multi-component diffusion coefficients	$[\frac{m^2}{s}]$
D_i^T	Thermal diffusion coefficient	$[\frac{kg}{m \cdot s}]$
D_i^M	Diffusion coefficient of compound i into mixture of the other compounds M	$[\frac{m^2}{s}]$
E_a	Activation energy	$[\frac{kJ}{mol}]$
E_i	Sensitivity	[-]
e_n	Internal energy	$[\frac{J}{kg \cdot K}]$
F	Function	[-]
j_q	Heat flux	$[\frac{J}{m^2 \cdot s}]$
j_n	Diffusion mass flux	$[\frac{kg}{m^2 \cdot s}]$
h_n	Specific enthalpy	$[\frac{J}{kg}]$
K_{eq}	Equilibrium constant	[-]
k	Rate coefficient	Unit depend on the global order of reaction
n	Exponential factor of temperature in Arrhenius law	[-]
p	Pressure	[Pa]
R	The universal gas constant ($R = 8.314$)	$[\frac{J}{mol \cdot K}]$
S	Specific entropy	$[\frac{J}{kg \cdot K}]$
T	Temperature	[K]
t	Time	[s]
u	Velocity	$[\frac{m}{s}]$
V	Volume	$[m^3]$
V_n	Diffusion velocity	$[\frac{m}{s}]$
W_n	Molecular weight	$[\frac{kg}{mol}]$
X_i	Molar fraction	[-]
Y_i	Mass fraction	[-]

Greek symbols

Φ	Fuel/air ratio	[-]
ν	Stoichiometric coefficient	[-]
τ_i	Induction time, i.e. ignition delay time	[ms]
τ	Mean residence time of the fluid in the reactor	[s]
ρ	Mass density	$[\frac{kg}{m^3}]$
$\dot{\omega}_n$	Mass rate of production of the n th species by chemical reaction	$[\frac{kg}{m^3 \cdot s}]$
λ	Heat conductivity	$[\frac{J}{K \cdot m \cdot s}]$
μ	Dynamic viscosity	$[\frac{kg}{m \cdot s}]$

Superscripts

f	Forward
<i>ab.</i>	Absolute
<i>rel.</i>	Relative
u	unburnt gas
r	Reverse
0	Standard state

Abbreviations

AMN	α -methylnaphthalene
FS	Laminar flame speed
JSR	Jet stirred reactor
MB	Methyl-butanoate
MD	Methyl-decanoate
MP	Methyl-palmitate
NTC	Negative temperature coefficient
PFR	Plug flow reactor
RCM	Rapid compression machine
ST	Shock tube

Acknowledgement

“Praise be to the LORD, the God of Israel, from everlasting to everlasting.”(Psalm 106:48)

Firstly, I express my gratitude to my supervisor Professor Fabian Mauss, who offered this thesis, leading me to research field of combustion modeling with his interest in science, wisdom and kindness. I would like to thank to PD Dr. Thomas Zeuch, who is willing to be the referee of this thesis and other publications, and always readily gives help.

I would like to thank all colleagues in kinetic group and chair, especially Amruta and Larisa for creating a friendly, tight-cooperative and creative atmosphere of work.

Special thanks to my husband, Yanjie Zhu, my parents and brother.